**Waves and eddies on a $\beta$ plane: experiments with altimetry**

by

Yang Zhang

Dissertation submitted to the School of Graduate Studies
in partial fulfillment of the
requirements for the degree of
Doctor of Philosophy

Department of Physics and Physical Oceanography

Memorial University of Newfoundland

2016

## Abstract

This study investigated problems related to beta-plane turbulence and wave radiation by a vortex drifting on a beta plane using laboratory experiments supplemented by numerical simulations and analytic methods. An optical system Altimetric Imaging Velocimetry was employed in the study. It directly measures geostrophic currents and then calculates the total current using the quasi-geostrophic approximation under a small Rossby number assumption.

The first part of the dissertation investigated the barotropic $\beta$-plane turbulence. In the first experiment, an electromagnetic method was employed to generate barotropic turbulent flows consisting of cyclones and prevalent anti-cyclones. Zonal jets were formed in both the forced-dissipative regime and the free-decaying regime. In the former case, jets are latent, are obscured by the strong vortices and are only visible after time averaging of the observed fields. In the second experiment, Thermal convection played the role of forcing with scales confined by the baroclinic deformation radius, which was much smaller than the scale of the electromagnetic forcing. The jets were more distinctive in this experiment. In both cases, an anisotropic energy spectrum was observed, where less energy was located inside a dumbbell-shaped area near the origin, whose boundary corresponds to the Rhines scale. Rather than arresting the inverse cascading energy, the dumbbell redirected energy to the zonal modes of approximately the forcing scale. The theoretical spectrum evolution showed that the zonal modes can be fed by an isotropic forcing through only linear dynamics. The west-propagating Rossby waves caused the asymmetry in the frequency-wavenumber spectrum with an energetic plume directing towards the west with a slope $V_{rms}k$, where $V_{rms}$ is the

root mean square velocity of the turbulent flow and $k$ is the isotropic wavenumber.

The second part of the dissertation presented the results from a series of experiments on baroclinic $\beta$-plane turbulence where a shear between two layers generated meanders, waves, eddies and filaments interacting with each other. The small eddies and thin filaments in these experiments are ageostrophic and can be related to the submesocale dynamics in the ocean, where energy slowly released from baroclinic instability cascades to smaller scales. Dynamics in spectral spaces were emphasized, and a normal Fourier transform in a local Cartesian coordinate system together with a Fourier-Bessel transform in a global polar coordinate system were employed. Rhines arguments hold on both spectra, which showed anisotrophy during a quasi-stationary regime. High energy concentration on the zonal modes larger than the Rhines scale, as well as low energy concentration below a threshold scale, represented by the dumbbell-shaped curve in the Fourier spectrum, were observed as well. In frequency-wavenumber space, prominent signatures due to the westward-propagating Rossby waves and the eastward-propagating baroclinic instability waves were revealed by dispersion relations.

Encouraged by the significance of the linear dynamics in $\beta$-plane turbulence, the third part of the dissertation extended the $\beta$-plume theory to an idealized scenario, i.e. wave radiation by a drifting vortex on a $\beta$-plane. In a series of experiments, a cyclonic vortex was generated by siphoning water out of the tank. A northwestward-propagating cyclone radiating Rossby waves (long waves to the west and short waves to the east) was observed in the experiments as well as in the pseudo-spectral simulation. Distinct inertial waves were obvious in the altimetric images. Decomposing the vortex into a primary monopole

and a secondary dipole showed that the vortex translation speed was indeed determined by its dipole component ($\beta$-gyres). In the far field the linear dynamics played a dominant role. Laboratory experiments, numerical simulation and a linear theory showed a similar wave pattern where the long wave crests aligned in a quasi-zonal direction to the west of the cyclone. A linear analogue of the Rhines wavenumber is proposed as $k_{Rhines} = \sqrt{\beta/U_t}$, which qualitatively described the energy distribution of large-scale dynamics in the spectrum, where $U_t$ is the vortex translation speed. This result might be applied to the ocean, where sparsely distributed eddies interact with each other through Rossby waves.

# Contents

**Contents** **i**

**List of Figures** **iii**

**List of Tables** **viii**

**1 Introduction** **1**
1.1 Background . . . . . 1
1.2 Main concepts . . . . . 2
1.3 Phenomena due to the $\beta$ effect . . . . . 8
1.4 Overview of the thesis structure . . . . . 19

**2 $\beta$-plane Turbulence** **20**
2.1 Introduction . . . . . 20
2.2 Laboratory apparatus and techniques . . . . . 25
2.3 Experimental results and analyses . . . . . 29
2.4 Discussions and conclusions . . . . . 53

**3 Baroclinic Turbulence on the Polar $\beta$-plane in the Rotating tank: Down to Submesoscale** **56**
3.1 Introduction . . . . . 56
3.2 Laboratory techniques . . . . . 58
3.3 Methods of spectral analyses . . . . . 60
3.4 Results . . . . . 65
3.5 Conclusions . . . . . 82

**Appendices** **85**
3.A Parseval's identity . . . . . 85
3.B Dispersion relation for two-layer baroclinic flow . . . . . 86

**4 Rossby Wave Radiation by an Eddy on a *beta*-plane** **88**
4.1 Introduction . . . . . 88
4.2 Laboratory setup and techniques . . . . . 92

4.3 The numerical model . . . . . 96
4.4 Theory . . . . . 97
4.5 Results . . . . . 102
4.6 Discussion . . . . . 121

**5 Conclusions** **124**

**Bibliography** **130**

# List of Figures

1.1 A sketch of the $\beta$-plume dynamics. . . . . 11
1.2 A sketch of the Rhine theory in the $k_x - k_y$ wavenumber space, where $k_x$ and $k_y$ denote the wavenumber in zonal and meridional directions respectively. Pink color denotes areas of high energy outside the solution where the presumed dispersion relation of turbulence controls the dynamics; meanwhile, the white color denotes the low-energy areas at large scales where Rossby waves dominate. $\epsilon$ is the energy injection/dissipating rate in a equilibrium state. The red rod along $k_y$ axis represents the zonal modes where the inversely cascaded energy accumulates. 12

2.1 Sketch of the experimental setup: rotating tank and the inner container (gray dashed lines) with the paraboloid false bottom (1) filled with water, video camera (2), high brightness TFT panel displaying the color mask (3), electrodes (4), and permanent magnets (5). A bird's view of the paraboloid false bottom where an array of magnets was placed is shown as the insert (6) between the camera and the tank. . . . . 26
2.2 Evolution of the barotropic turbulent flow with the $\beta$-effect visualized by AIV in the Bt experiment (Multimedia view): initial period shortly after the forcing starts, $t = 2\ s$ (a-c), stationary forced turbulence, $t = 380\ s$ (d-f) and decaying turbulence, $t = 2\ s$ (g-i) and $t = 30\ s$ after the forcing was stopped (j-l). The first column of panels shows velocity vectors superposed on color altimetry images. The velocity scale is given in the lower left corner of each panel. The second column shows the x-component of velocity, $v_\theta$, while the third column shows the dimensionless vorticity $\zeta/f_0$ varying from negative values (black, anticyclonic) to positive values (white, cyclonic). . . . . 30
2.3 Baroclinic flow generated by thermal forcing in the Bc: forced turbulence, $t = 360$ s (a, b) and decaying turbulence, $t = 40$ s after the forcing was stopped (c, d). Panels (a) and (c) show the x-component of velocity, $v_\theta$; panels (b) and (d) show the dimensionless vorticity $\zeta/f_0$. . . . . 32
2.4 Kinetic energy $\bar{E}$ and enstrophy $\bar{\zeta}^2$ averaged over the tank versus time in the Bt (a, c) and Bc (b, d) experiments. . . . . 34

2.5 Evolution of the two-dimensional energy spectrum in the Bt experiment. The scale on the right shows the logarithm of relative energy (normalized by spatial averaged energy in the tank), in $k_x - k_y$ wavenumber space at (a) $t = 4$ s, (b) $t = 382$ s from the start of the experiment and at (c) $t = 12$ s after the forcing was switched off. The white line in panel (b) shows $k_R$ given by Equation (2.10) while the black line shows $k_\beta$ given by Equation (2.11). . . . . 36
2.6 Two-dimensional energy spectrum in the Bc experiment in the beginning of the experiment at (a) $t = 35$ s and at (b) $t = 37$ s after the forcing was switched off. The white and black lines show $k_R$ and $k_\beta$, respectively. . . . . 38
2.7 The evolution of the energy spectrum given by the theoretical solution Equation (2.14). The scale on the right shows the logarithm of energy in $k_x - k_y$ wavenumber space at (a) $t = 10$ s, (b) $t = 100$ s, and at (c) $t = 500$ s. The dimensional parameters are $k_f = 1$ cm$^{-1}$ , $f_0 = 4.64$ s$^{-1}$, $\beta = 0.2$ cm$^{-1}$s$^{-1}$ , and $R_d = 18$ cm. . . . . 42
2.8 The one-dimensional spectra of relative energy (normalized by spatial average energy in the tank) in forced (a) and in decaying turbulence (b) with the barotropic electromagnetic forcing: energy $E(k)$ (upper curve) and zonal energy $E_Z(k_y)$ (lower curve). Arrows indicate the forcing wavenumber $k_f$. Panel (c) and (d) shows the Kolmogrov constants of $E(k)$ and $E_Z(k_y)$ in (a). . . . . 43
2.9 The same as before but for the flows with the baroclinic thermal forcing. . . . . 44
2.10 Evolution of the one-dimensional energy spectra (a, b) and the energy-weighted mean wavenumber $k_E$ (c, d) in decaying turbulence in the Bt (left column) and Bc (right column) experiments. Arrows indicate time when the forcing was switched off in each experiment. . . . . 47
2.11 Velocity $v_\theta$ measured along a circle of radius $r_0$ equal to two thirds of the radius of the domain at different times in the Bt (a) and Bc (b) experiments. The gray scale shows $v_\theta$ in cm/s. . . . . 49
2.12 The relative energy (normalized by the spatial-averaged energy) spectrum in the frequency-wavenumber space. The scale shows the logarithm of energy. The frequency is normalized by the Coriolis parameter $f_0$ . White curves show the Rossby wave dispersion relation Equation (2.7) with $k_y = 0.07$ cm$^{-1}$ and $R_d = 20$ cm (a), and $k_y = 0.06$ cm$^{-1}$ and $R_d = 19$ cm (b) (upper curves); and with $k_y = 0.7$ cm$^{-1}$ and $R_d = 20$ cm (a), $k_y = 0.7$ cm$^{-1}$ and $R_d = 19$ cm (b) (lower curves). The solid straight lines shows turbulent frequency given by Equation (2.8) with $V_{rms} = 1.34$ cm/s (a) and $V_{rms} = 0.4$ cm/s (b). . . . . 50
2.13 Rossby wave with spiral wavecrests propagating towards the center of the domain and represented by a solution in the form of the Hankel function. . . . . 51

3.1 Baroclinic flow in the rotating tank at $t = 120$ s after switching off the fresh water source: (a) velocity (arrows) superposed on the altimetric color image; (b) magnified view of the vortex indicated by the green arrow; (c) dimensionless relative vorticity, $\zeta/f_0$ varying between -1 (blue) and +1 (red) and (d) dimensionless strain rate, $s/f_0$ varying between 0 (blue) and +1 (red). Lower layer salinity is $S = 20$ ppt. . . . . 66
3.2 Time series of the mean azimuthal velocity, $V_{\theta,\ mean}$, rms azimuthal velocity, $V_{\theta\ rms}$, and rms radial velocity, $V_{r,\ rms}$. Time starts when the fresh water injection is stopped. Lower layer salinity is $S = 30$ ppt. . . . . 67
3.3 Energy spectra in the wavenumber domain: (top row) the Fourier spectra in the Cartesian coordinates and (bottom row) the Fourier-Bessel spectra in the polar coordinates at (a, d) $t = 1$ s, (b, e) $t = 300$ s, and (c, f) $t = 700$ s after switching off the fresh water source. Color scales show energy in logarithmic scale. Red lines in (c) and (f) display Equation (3.17) and Equation (3.19) respectively. Black crosses in (c) mark the Rhines wavenumber while the white lines in (f) are lines of $\alpha_{mn} = 30$, 50, 70, and 90. Lower layer salinity is $S = 30$ ppt. . . . . 69
3.4 1D energy spectra in the wavenumber domain in the experiments with salinity (left) $S = 12$ ppt and (right) $S = 30$ ppt. Blue and black lines show the Fourier and Fourier-Bessel spectra respectively. . . . . 72
3.5 Energy spectra in the frequency-wavenumber space measured along the circles of radii (a) $r = 0.5R$ and (b) $r = 0.7R$. White line shows the Rossby wave dispersion relation Equation (3.20) with $k_y = 2\pi/R$ while black and red lines show the damped and growing waves obtained by solving Equation (3.29) with $k_y = (1,\ 2,\ 5) \times 2\pi/R$. Color scales show relative energy (normalized by its spatial average) in logarithmic scale. Lower layer salinity is $S = 10$ ppt. . . . . 74
3.6 1D spectra of relative energy, normalized by the spatial averaged energy, in the frequency domain in the experiments with salinity (black line) $S = 20$ ppt and (blue line) $S = 10$ ppt. . . . . 77
3.7 Energy flux as a function of the wavenumber in two experiments with salinity (a) $S = 15$ ppt and (b) $S = 30$ ppt. Blue line displays the flux measured in the beginning of the experiments, soon after the injection of the fresh water was stopped, at $t = 10$ s, while the thin and thick black lines show the flux during quasi-steady period of the flow at $t = 270$ s and $t = 430$ s respectively. . . . . 79
3.8 Relative vorticity in the experiment with salinity $S = 30$ ppt at $t = 270$ s: (a) original field, (b) filtered at $k_l = 1.5$ rad/cm and (c) filtered at $k_l = 3.5$ rad/cm. Vorticity is normalized by the Coriolis parameter and varies in the range between -0.5 (blue) and +0.5 (red). . . . . 81
3.9 Energy flux, $\Pi^l$, in the experiment with salinity $S = 30$ ppt at $t = 270$ s: (a) $k_l$ = 1.5 rad/cm and (b) $k_l = 3.5$ rad/cm. Energy flux varies in the range between -0.8 $\mathrm{cm^2 s^{-3}}$ (blue) and +0.8 $\mathrm{cm^2 s^{-3}}$ (red). . . . . 82

4.1 (a) Sketch of the experimental setup (left): digital camera (1), high brightness display showing the color mask (2), the fluid in the tank is pumped out through a thin tube (3) to generate a cyclonic vortex (4). (b) Top view of the flow with a superposed velocity field (vectors) measured by the AIV at 19 s in experiment 1. 93
4.1 Flow evolution in experiment 1 visualized by AIV: (a) the beginning of forcing, $t = 4$ s, (b) the end of the forcing period when the vortex achieved its maximum strength, $t = 9$ s, (c) and (d) unforced vortex, $t = 16$ s and $t = 28$ s. The arrows (blue) indicate the velocity field. . . . . 103
4.2 Surface elevation field in experiment 1 at $t = 10$ s (a) and $t = 12$ s (b). Gray scale shows $\eta$ in cm. . . . . 104
4.3 Characteristics of vortices measured in experiments 1-5: the azimuthal velocity in cm/s (the first column), the surface elevation in cm (the second column), total kinetic energy as a function of time (the third column), and the vortex trajectory (the fourth column). The total time of travel after the forcing stops is indicated in the last column. . . . . 105
4.4 Monopolar and dipolar components of the flow in experiments 1 – 5: (the first column) the monopolar component $M$ (contours show $\eta$ in the range from $-0.25$ cm to $-0.03$ cm with 0.03 cm interval and arrows show the geostrophic velocity); (the second column) the dipolar component (contours show $\eta$ in the range from $-0.2$ cm to 0.2 cm with 0.004 cm interval, lighter gray lines (red) indicate positive values, the darker gray lines (blue) indicate negative values, the black shows zero $\eta$, and arrows show the geostrophic velocity); (the third column) radial profiles $M(r)$ (solid line), $a(r)$ (dashed line), and $b(r)$ (dashed-dotted line); and (the fourth column) zonal and meridional components of the translation velocity of the vortex measured in the experiments (solid darker gray/blue and lighter gray/red lines, respectively) and the velocity derived from the dipolar component (dotted lines). . . . . 108
4.5 Evolution of the monopolar (the first column) and the dipolar (the second column) components of the flow in experiment 1 at $t = 11$ s, 16 s, 21 s, 26 s, and 31 s. The third column gives $M(r)$ (solid line), $a(r)$ (dashed line), and $b(r)$ (dashed-dotted line). The contour lines show $\eta$ with 0.01 cm interval for the monopole and with 0.005 cm interval for the dipole. . . . . 110
4.6 Comparison of the surface elevation fields $\eta$ in experiment 1 (the first column), numerical shallow-water simulation (the second column), and linear theory (the third column). Values of $\eta$ is in the range between $-0.03$ cm (darker gray/blue) and 0.03 cm (lighter gray/red). . . . . 112
4.7 Same as in Fig. 7 but for the relative vorticity fields. Vorticity is normalized by the Coriolis parameter and varies in the range between $-0.5$ (darker gray/blue) and 0.5 (lighter gray/red). Arrows indicate the crests of inertial waves emitted by the evolving vortex. . . . . 113
4.8 Sequence of the altimetric images of the vortex at $t = 10$ s (a), 12 s (b), and 14 s (c). Thin bands spiraling around the vortex are inertial waves. . . . . 115

4.9 Hovmoeller (space-time) diagram of the geostrophic velocity measured along the straight line parallel to the vortex trajectory. Gray scale shows velocity in cm/s. 115
4.10 Two-dimensional energy spectra, $E(k_x, k_y)$ in experiment 1 (upper row, a-c), numerical simulations (middle row, d-f), and theory (bottom row, g-i) at $t = 10$ s, 16 s, and 22 s, respectively. Color scale shows $ln(E)$. Solid black lines show the solution of Equation (4.27) with $\omega_0 = 0$. The white curves show the solution of Equation (4.27) with $\omega_0 = 2\pi/\Delta t$, where $\Delta t = 12$ s. . . . . 119

# List of Tables

4.1 Experiment parameters. . . . . 96

I would like first to express my deep appreciation and thanks to my advisor Professor Dr. Yakov Afanasyev, for his continuous support of my Ph.D study and related research. His guidance helped me in all the time of research and writing of the papers. Obviously I am blessed for having an supervisor with a good instinct in physics, educated eyes during the GFD lab experiments, and a nice personal character.

I would like to thank Dr. Entcho Demirov and Dr. James Munroe for having served my supervisory committee in the past few years. I appreciate the encouragements and suggestions on my interest in numerical simulation from them.

I would also like to express my appreciation to Professor Dr. Len Zedel and Professor Dr. Brad DeYoung for their services in my exam committee during the comprehensive exam and defense. I am gratitude to the corrections and useful comments from the examiners including an external examiner Dr. Bruce Southerland, from whose comments I benefit a lot for the future growth.

Many thanks to my colleagues in the Physical Oceanography Department: Alexandr Konstantinov, Dr. Anna Matuka and Cris Stevenson for their technical support, Fan Lin and Yi Sui for the accommodations.

The final thank you is for my family, especially my wife Xiaolei Li, for their long-term support and encouragement.

# Chapter 1

# Introduction

## 1.1 Background

Geostrophic fluid dynamics is distinguished from general fluid mechanics due to rotation and density stratification, which are characterized by two frequencies: the Coriolis frequency and the buoyancy frequency, respectively. The rotation introduces a Coriolis force, which acts on a moving object to its right in the northern hemisphere. The Coriolis force does not do work; it does, however, generate eddies. Due to the small aspect ratio of the oceans (Shell approximation), large-scale ocean circulations can be described by the Shallow Water Equations.

The ocean circulations are turbulent and consist of coherent structures such as eddies, waves and jets interacting with each other. In three-dimensional turbulence, Kolmogorov's dimensional analysis showed that kinetic energy (and enstrophy as well) continuously cas-

cades to smaller scales until it reaches a dissipating scale. Given the two-dimensional character of large-scale circulations, the requirement of both energy and enstrophy conservation results in an inverse energy cascade, i.e. energy transfers from the forcing scale to larger scales; meanwhile, enstrophy still cascades to smaller scales. [44, 69].

## 1.2 Main concepts

In this section, some relevant textbook concepts are reviewed for the reader's reference.

### The $\beta$-plane approximation

Due to the Earth surface curvature, the Coriolis frequency $f = 2\Omega \sin\theta$ increases with latitude $\theta$, where $\Omega$ is the Earth rotating rate. The increasing trend is almost linear in a region of limited meridional span centered at a reference latitude $\theta_0$. Then the Coriolis frequency can be expanded into a Taylor series on the small meridional displacement $\delta y = r_E \delta\theta$:

$$f = f_0 + \frac{\partial f}{\partial y}\delta y. \tag{1.1}$$

This first-order approximation constitutes a local $\beta$-plane where $f_0 = 2\Omega \sin\theta_0$ and $\beta = 2\Omega \cos\theta_0 / r_E$ are two constants over the zonal band, $r_E$ is the Earth radius.

## Topographic $\beta$ effect

The linear-varying topography and the $\beta$-plane approximation have dynamic similarity in terms of potential vorticity (PV afterwards) conservation, i.e.

$$\frac{dq}{dt} = 0, \tag{1.2}$$

where

$$q = \frac{\zeta + f}{H - h_b} \tag{1.3}$$

is defined as the barotropic PV, $\zeta$ is the relative vorticity, $h_b = sy$ is a bottom topography increasing northward with the meridional displacement $y$ and a slope $s$, and $H$ is the mean water depth without surface elevation or bottom topography. Here we assume that $h_b/H << 1$, then PV could be approximated by

$$q \approx \frac{f + (fs/H)y}{H}. \tag{1.4}$$

One can see that the second term in the numerator plays a similar role as the second term on RHS of Equation (1.1), the $\beta$-plane approximation. It is called the topographic $\beta$-effect with $\beta_T = fs/H$.

In the rotating tank experiment $\beta_T$ needs to be clarified. The free surface of the rotating fluid is a paraboloid when in solid-body rotation, the water depth varies quadratically with the distance $r$ from the rotating axis

$$h_R(r) = Ar^2 + B, \tag{1.5}$$

where

$$A = \frac{\Omega^2}{2g}, \quad B = H - h_b - \frac{(\Omega R_t)^2}{4g}.$$

Here $H$ is the mean water depth without rotation or topography, $g$ is the acceleration due to gravity, and $R_t$ is the radius of the tank. The tank rotates anti-clockwise at a rate of $\Omega = 2.38$ rad/s. In order to derive the local $\beta_T$ at certain radius $r_0$ away from the center of the tank, a local Cartesian coordinate system is introduced at $r_0$, such that the local $x$ and $y$ axes are directed to the East and to the North correspondingly. Then PV can be written as

$$q = \frac{\zeta + f_0}{A(r_0 - y)^2 + B} \approx \frac{\zeta + f_0}{h_R(r_0) - 2Ar_0 y} \approx \frac{\zeta + f_0}{h_R(r_0)}(1 + \frac{2Ar_0 y}{h_R(r_0)}).$$

By analogy with (1.4) the topographic $\beta_T$ is

$$\beta_T = \frac{2Ar_0 f_0}{Ar_0^2 + B}. \tag{1.6}$$

In a small area surrounding the rotating axis, the dependence on $r$ is quadratic, rather than linear, such that

$$q = \frac{\zeta + f_0}{Ar^2 + B} \approx \frac{\zeta + f_0}{B}(1 - \frac{A}{B}r^2).$$

The above approximation constitutes the so-called polar $\beta$-plane or $\gamma$-plane in the center of the tank.

## Rossby waves

The $\beta$-effect plays as a restoring force in Rossby waves. The dynamics of Rossby waves are governed by the equation of conservation of relative vorticity:

$$\frac{\partial}{\partial t}(\nabla^2 - R_d^{-2})\eta + \beta\eta_x = 0, \tag{1.7}$$

where $R_d$ is the deformation radius, $\eta$ is the surface elevation, and the subscript $x$ in $\eta_x$ means its spatial derivative with respect to $x$. Here the nonlinear term is neglected. The dispersion relation can be obtained by the Fourier transform of Equation (1.7). Substituting the Fourier decomposition of $\eta$, i.e.

$$\eta(x, y) = \sum_{k_x, k_y} \tilde{\eta}(k_x, k_y) \exp\Big(i \cdot (k_x x + k_y y - \omega t)\Big),$$

where $\mathbf{k} = (k_x, k_y)$ is the wavenumber vector, $\omega$ is the wave frequency, and $\tilde{\eta}(k_x, k_y)$ represents the amplitude of mode $\mathbf{k}$, into Equation (1.7) gives the dispersion relation for Rossby waves in the form:

$$\omega = \frac{-\beta \cdot k_x}{k^2 + R_d^{-2}}, \tag{1.8}$$

here $k = \sqrt{k_x^2 + k_y^2}$ is the isotropic wavenumber.

## Dynamics in the polar coordinate system

Since the tank is cylindrical, it is necessary to derive the relative vorticity equation and also the disperison relation for Rossby waves in polar coordinate system $(r, \theta)$. The PV conservation shows

$$\frac{dq}{dt} = \frac{d}{dt}(\frac{\zeta + f}{h_R + \eta}) = 0. \tag{1.9}$$

Substituting Equation (1.5) into the above equation gives

$$\frac{dq}{dt} = \frac{d\zeta}{dt} - \frac{\zeta + f}{h_R + \eta}(2Ar\frac{dr}{dt} + \frac{d\eta}{dt}) = 0. \tag{1.10}$$

One can introduce the geostrophic approximation in the polar coordinate system such that the velocity is defined as

$$(v_\theta, v_r) = \mathbf{k} \times \frac{g}{f}\nabla\eta = \frac{g}{f}(\frac{\partial\eta}{\partial r}, -\frac{\partial\eta}{r\partial\theta}). \tag{1.11}$$

The geostrophic approximation also implies

$$\zeta = \frac{g}{f}\nabla^2\eta, \tag{1.12a}$$

$$\frac{d\eta}{dt} = \frac{\partial\eta}{\partial t}. \tag{1.12b}$$

Substituting the above 3 equations into Equation (1.10) gives

$$\begin{aligned}\frac{dq}{dt} &= \frac{g}{f}\frac{d}{dt}(\nabla^2\eta) - \frac{\zeta + f}{h_R + \eta}(2rv_rA + \frac{\partial\eta}{\partial t}) \\ &= \frac{\partial}{\partial t}(\frac{g}{f}\nabla^2 - \frac{\zeta + f}{h_R + \eta})\eta + \frac{g^2}{f^2}J(\eta, \nabla^2\eta) - \frac{\zeta + f}{h_R + \eta}2rv_rA \\ &= 0.\end{aligned}$$

Here $g^2J(\eta, \nabla\eta)/f^2$ is the nonlinear term and $J(a, b) = a_xb_y - a_yb_x$ represents the Jacobian operator. Neglecting the nonlinear term and using the following approximation

$$\frac{\zeta + f}{h_R + \eta} \approx \frac{f}{h_R}$$

show

$$\frac{\partial}{\partial t}(\frac{g}{f}\nabla^2 - \frac{f}{h_R})\eta + \frac{f}{h_R}2rv_rA = 0.$$

Multiplying it by $f/g$ and using the geostrophic approximation for $v_r$ one obtains

$$\frac{\partial}{\partial t}(\nabla^2 - R_d^{-2})\eta + \frac{2Af\eta_\theta}{h_R} = 0, \tag{1.13}$$

where $R_d = \sqrt{gh_R}/f_0$ is deformation radius. In a polar-coordinate system, a natural basis is the Fourier-Bessel series:

$$\eta(r, \theta, t) = \sum_{m=0}^{\infty} B_m J_m(r') \exp(im\theta - i\omega t), \tag{1.14}$$

where $r' = kr$, $B_m$ is the amplitude for mode $m$, and $J_m(r')$ is $1^{st}$ kind Bessel function of order $m$. It could be shown that Fourier-Bessel series satisfies

$$\nabla^2 \eta = -k^2 \eta, \tag{1.15}$$

which actually is the Bessel equation:

$$r'^2 \frac{\partial^2 J}{\partial r'^2} + r' \frac{\partial J}{\partial r'} + (r'^2 - m^2)J = 0. \tag{1.16}$$

Substituting the Fourier-Bessel decomposition into Equation (1.13) gives a dispersion relation of Rossby waves in polar coordinate system in the form:

$$\omega_R = \frac{-\beta_T k_x}{k^2 + R_d^{-2}}, \tag{1.17}$$

which is an analogue of (1.8). Here the dimensional azimuthal wavenumber is $k_x = Am$. Note that $\beta_T = 2f_0/h_R$ here is different from that in (1.6), where $\beta_T$ is derived in a local Cartesian coordinate system (the $\beta$-plane approximation); however, $\beta_T$ in Equation (1.17) is a global function of $r$ in the polar coordinate system. In practice when the radial profile

$\eta(r)$ is complicated, one can always use the following decomposition:

$$\eta(r) = \sum_{n=1}^{\infty} C_n \cdot J_m(\frac{r}{R}\alpha_{m,n}), \tag{1.18a}$$

$$C_n = \frac{\int_0^R r\eta(r)J_m(r/R\alpha_{m,n})dr}{0.5[RJ_{m\pm1}(\alpha_{m,n})]^2}, \tag{1.18b}$$

where $J_m(r)$ is the $1^{st}$ kind Bessel function of order $m \geq -1$, $R$ is radius of the domain, and $\alpha_{m,n}$ is the $n^{th}$ positive root of $J_m(r)$. As a result, the formal Fourier-Bessel decomposition is given as

$$\eta(r,\theta,t) = \sum_{m=0}^{\infty}\sum_{n=0}^{\infty} B_{mn}J_m(\frac{r}{R}\alpha_{m,n})\exp(im\theta - i\omega t), \tag{1.19}$$

where $B_{mn}$ is the amplitude for mode $\alpha_{m,n}/R$ and $m$ is azimuthal wavenumber. As a result, the dispersion relation becomes

$$\omega_R = \frac{-\beta_T(r)k_x}{(\alpha_{mn}/R)^2 + R_d(r)^{-2}}. \tag{1.20}$$

## 1.3 Phenomena due to the $\beta$ effect

### Rossby waves

On a $\beta$-plane, different types of coherent structures emerge in a background of geostrophic turbulence. The primary one is the generation of Rossby waves, which were first discovered by Carl Gustave Rossby in the 1930s as the big meanders of the jet stream in the atmosphere. Nowadays, these large-scale waves can be observed in the oceans by satellite altimeters. The signal of the Rossby wave propagation is usually visible in the Hovmoller diagram of sea surface height(SSH, [30, 90]) and sea surface temperature (SST, [56]). The oceanic Rossby

waves have amplitudes of $\mathcal{O}(10)$ cm, periods of months to years, and wavelengths of $\mathcal{O}(100)$ km to $\mathcal{O}(1000)$ km, respectively. The wave speed increases equatorward of course with $\beta$, specifically the zonal-averaged speed varies from 1 km/day to 27 km/day from 50 $^0N$ to 5 $^oN$.

Rossby waves have great significance in oceans and the atmosphere. In the zonal direction, long Rossby waves carry energy to the west [87], contributing to the westward intensification of circulation gyres [9]. Their westward propagation provides a mechanism for the response of the western boundary area to the atmospheric perturbation in the interior basin [85, 67, 105, 59]. In the equatorial region, the reflected Rossby waves and equatorial Kelvin waves play a key role in the dynamics of El Nino and Southern Oscillation (ENSO) events in the Pacific Ocean[74]. Rossby wave radiation is important as well to the dipole mode in the Indian Ocean[22]. In the meridional direction, Rossby waves explain planetary-scale atmospheric teleconnections [124, 57, 62, 61, 125, 71]. In terms of marine biology, the upwelling due to the wave radiation affects chlorophyll in the upper mixing layer [65, 35, 103].

## Zonal jets

Another ubiquitous phenomenon on a $\beta$-plane is zonal jets. Satellite observations show an abundance of zonal/quasi-zonal jets of alternating direction in areas with strong baroclinic instability, such as the Antarctic Circumpolar Current, Gulf Stream and Kuroshio extensions [80, 81, 109, 120]. Midlatitude jets have a width of 150 km $\sim$ 300 km and a velocity magnitude of about 7 cm/s. Zonal jets are latent in the ocean, i.e. they are obscured by energetic eddies

and are only visible after time averaging of the observed fields. Their latency is determined by the large-scale friction [73, 17] or energy injection rate [106] if in an equilibrium state. More prominent jets are observed in atmospheres in giant gas planets like Jupiter and Saturn [53], where they manifest as alternating stripes of different colors. Zonal jets, especially eastward ones, act as barriers to meridional transportation of mass, although some particles are still able to penetrate them after a long time [112]. The spontaneous emergence of zonal jets in a background of geophysical turbulence on a $\beta$-plane as well as their barrier role in meridional transportation are still under investigation[12].

Conceptual models based on either linear wave dynamics or quasi-linear wave-eddy interactions have been proposed as the mechanism for jet formation. One of the linear mechanisms of jet formation is the so-called $\beta$-plume mechanism [70, 116, 38]. A $\beta$-plume is a zonal-elongated gyre of circulation west of a localized source of perturbation. The plume is carried by nearly non-dispersive long Rossby waves. Two zonal jets with opposite directions develop at the southern and northern flanks of the plume, and are reconnected around the source of perturbation as well as in the front of the westward-propagating plume (see Figure 1.1). Recent experiments by [4, 108, 117] showed how a $\beta$-plume works in generating zonal jets.

In the case of a homogeneous eddy forcing, the Rhines wavenumber $k_R = \sqrt{\beta/V_{rms}}$ [98] can be introduced, where $V_{rms}$ is the root-mean-square velocity of turbulent motions. The Rhines scale denotes a spatial scale where the inversely cascading energy from small-scale nonlinear interactions starts feeling large-scale wave dynamics, and being transferred to Rossby waves and subsequently towards zonal jets. The Rhines theory is essentially

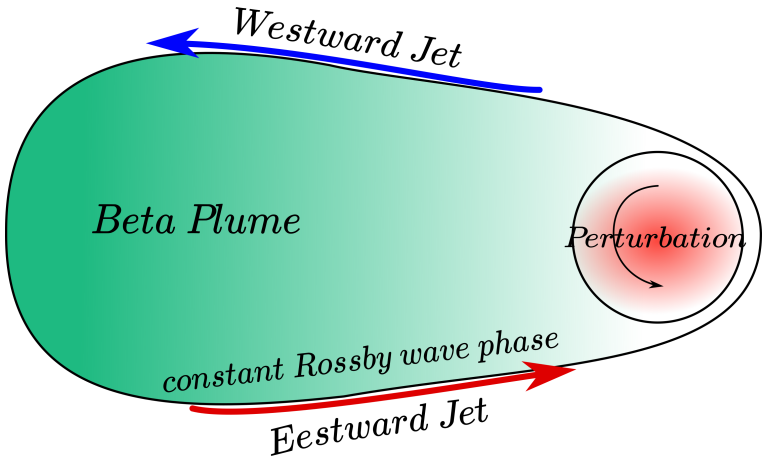


Figure 1.1: A sketch of the $\beta$-plume dynamics.

a synchronization condition of frequencies of different classes of dynamics. By equating the turbulence frequency to that of linear Rossby waves [122], one is able to solve for the solution in the $k_x - k_y$ wavenumber space as shown in Figure 1.2. The solution is of a lazy-8/dumbbell structure where the Rossby wave dynamics dominate at large scales inside the dumbbell; meanwhile, the nonlinearity due to eddy interactions dominates the dynamics at small scales outside. In spectral space the anisotropic energy distribution of $\beta$-plane turbulence is well known. In a forced-dissipative equilibrium, the dumbbell become visible as the energy clusters around it[60, 122, 121].

When zonal jets emerge the spectrum can be even more anisotropic, and more energy cascades to the zonal modes $k_x = 0$ with a spectrum predicted as $E_Z(k_y, k_x = 0) = C_Z \beta^2 k_y^{-5}$. In the literature $E_Z(k_y)$ is denominated as "zonal spectrum" even though it represents the meridional variation of zonal modes. The $-5$ spectrum is first suggested in [98] using a dimensional analysis. Although its universality is invalidated [36], the $-5$ slope is commonly

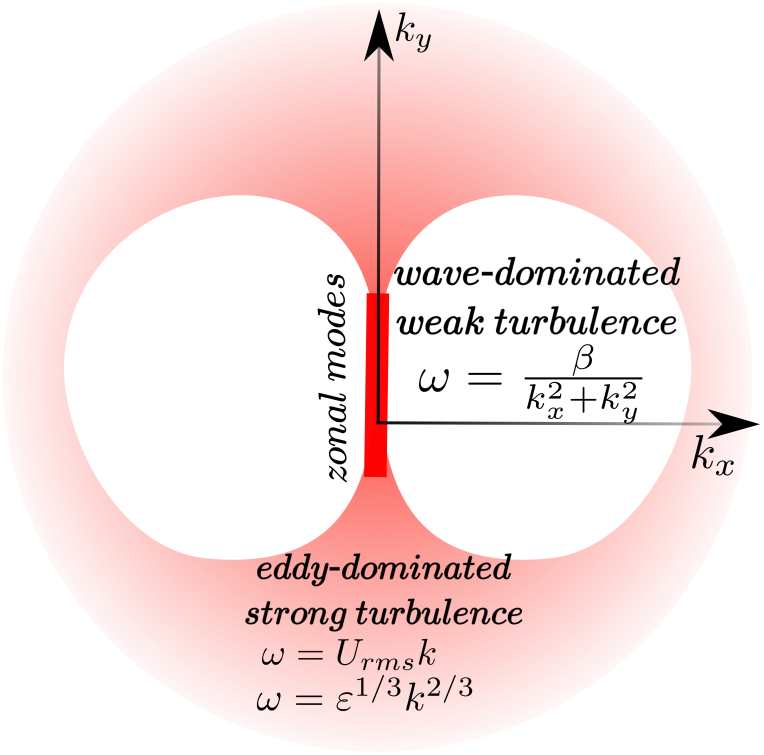


Figure 1.2: A sketch of the Rhine theory in the $k_x - k_y$ wavenumber space, where $k_x$ and $k_y$ denote the wavenumber in zonal and meridional directions respectively. Pink color denotes areas of high energy outside the solution where the presumed dispersion relation of turbulence controls the dynamics; meanwhile, the white color denotes the low-energy areas at large scales where Rossby waves dominate. $\epsilon$ is the energy injection/dissipating rate in a equilibrium state. The red rod along $k_y$ axis represents the zonal modes where the inversely cascaded energy accumulates.

observed at large scales [29, 52, 119, 53].

According to the PV conservation, zonal jets formation could be a consequence of horizontal potential vorticity mixing by wave breaking or eddy penetration. Zonal jets tend to mix PV in their flanks, which facilitates further mixing, thus leaving a strong PV gradient in the eastward jets. This positive feedback mechanism accounts for the strongly inhomo-

geneous regime, namely PV staircase observed in giant gas planets and in high-resolution simulations [93, 75, 106]. A fully-developed PV staircase shows an asymmetry between the eastward jets and westward ones, where eastward jets are more stable and narrower in width compared to the westward jets. The meridional PV profile is piecewise constant separated by step functions, whose locations indicate the cores of self-sharpening eastward jets. In contrast, westward jets are more turbulent, and PV near the axis tends to be homogeneous. This asymmetry is observed in early lab experiments [112]. In a PV staircase the original $k_R$ might be irrelevant since the wave dynamics are significantly modified by the zonal jets.

Another approach is offered by the statistical structure stability theory (3ST) [21] which excludes eddy-eddy interaction. The general idea is maximizing entropy while keeping energy and enstrophy invariant. A recent numerical study [33] validated the 3ST theory, showing that zonal jets emerge without the eddy-eddy interaction, or equivalently the local nonlinear cascade in spectral space, hence suggesting that non-local cascade dominates the process leading to the jet [13, 63, 128]. The famous "negative viscosity" phenomenon in physical space exemplifies the non-local cascade, where infinitesimal perturbation in the mean flow can arrange eddies to absorb eddy flux into zonal jets without wave breaking [11]. The non-local interaction might take the forms of non-zonal structures [73, 18]. Numerical studies [18] have shown that meridional jets of alternating direction emerge as "noodles" during the early spin-up stage, and these meridional jets undergo secondary transverse instability into zonal jets. The Rhines scale is skipped over in this process, and energy is tunneled directly to zonal modes through the express of the non-zonal structures. A similar mechanism is also

observed in the ocean [91].

In many circumstances the Rhines scale is often interpreted as the jet scale [86], though the scale-dependent $V_{rms}$ is hard to determine sometimes, thus making the direct interpretation controversial. In Ref. [16] the Rhines scale is found to be valid only in a limited parameter range, which implies that more factors need to be considered. The primary candidate is the deformation radius $R_d$ [41, 83, 127, 79], while other factors such as the bottom friction have also been suggested [73].

In the forced-dissipative equilibrium, $k_R$ alone might be insufficient in describing the $\beta$-plane turbulence, and the energy injection/dissipating rate $\epsilon$ must be included. Therefore, a ratio $R_\beta = k_\epsilon/k_R$ is employed to characterize different equilibrium states, and it includes another characteristic friction wavenumber $k_\epsilon = (\beta^3/\epsilon)^{1/5}$ [122]. $R_\beta > 2$ represents a regime where jets dominate [51]; an extreme case is the PV-staircase with $R_\beta \approx 10$ [106]. $R_\beta < 1.5$ corresponds to a viscous regime with latent jets. A similar result is obtained in [37] but while using a different $k_\epsilon$ that permits unsteady flows. Besides its capability of phenomenological description, $R_\beta$ is also found to be important to the jet scale [106].

In the first part of the dissertation, turbulence over a topographic $\beta$-plane was investigated using laboratory experiments with a focus on its spectral characteristics. Although $\beta$-plane turbulence has been a subject of study in laboratory experiments by different authors [126, 39, 111, 112, 110, 42], its spectral evolution has not been well understood, partly due to the deficiency of commonly-used PIV (Particle Image Velocimetry) techniques in visualizing the entire flow field with enough resolution. The optical system Altimetric Image

Velocimetry (AIV) employed in this study provides 4 million pixels in each image. Energy distributions in the $k_x$-$k_y$ space as well as in the frequency-wavenumber space were described in detail. One-dimensional spectra showing classic dual cascade ranges were presented. It is interesting to see if the Rhines wavenumber $k_R$ as well as its two-dimensional analogues work in both physical and spectral space in lab experiments. For this purpose, one needs a wide inverse cascade range. The AIV technique can provide a span of scales of 3 decades and the forcing was placed at a small scale. Electromagnetic forcing as well as convective thermal forcing were used in the experiments. Although the thermal forcing in the second experiment was baroclinic, the flows stayed barotropic to a great extent. The second motivation is to validate the importance of linear dynamics as inspired by the $\beta$-plume theory [70]. Results showed that energy transfer to the zonal modes through only linear dynamics is possible. The linear spectrum evolution is qualitatively similar to those observed in the lab experiments.

The second part of the dissertation focused on the spectral characteristics of baroclinic turbulence in a two-layer system. In a series of experiments, freshwater injected from the wall of the tank formed an eastward jet flowing on top of a saline layer. Baroclinic instability due to the shear between two layers created meanders and waves of large scales, as well as vortices and filaments of small scales. The spectral analyses reported in this part included both Fourier transform and Fourier-Bessel transform. It is interesting to find and validate the analogues of Rhines arguments in the Fourier-Bessel spectrum. The second question here is the significance of linear dynamics, especially if the dispersion relations of Rossby waves

and baroclinic instability waves could be validated in the observed frequency wavenumber spectra.

## Wave radiation by a traveling vortex

Mesoscale oceanic eddies are found virtually everywhere in the oceans [31]. They are subject to the $\beta$-effect during their long-term evolution. This effect is known as the $\beta$-drift. A cyclone drifts to the Northwest while an anticyclone travels to the Southwest on a $\beta$-plane. The self-induced advection of vortices over a large distance is important to mass [135], heat and PV transport in the ocean.

The general dynamics governing eddy evolution are the interplay between the Rossby waves radiated away by the traveling vortex and nonlinearity localized around the vortex. The northwestward/southwestward drift of the cyclone/anticyclone is analytically studied in Ref [1] using Taylor expansion in time. The dynamics could be easily understood conceptually. The northward Coriolis acceleration acting on the northern half of a cyclone is greater than its counterpart on the southern half due to the $\beta$-effect; therefore, integrating the Coriolis force over the cyclone/anticyclone gives a northward/southward Rossby force [102]. Modelling the vortex as a rigid body [47], one can show that the northward/southward propagating cyclone/anticyclone is pushed to the west by a lift force. This simple mechanical model works better for an isolated vortex with a sharp radial profile (as supported by the theory [68]), formed by stirring the fluid inside a cylinder in the experiment of [47]. Because the strong nonlinearity prevents wave radiation to some extent[84, 95], an isolated vortex of

strong nonlinearity seems to be more rigid.

An alternative explanation is that the drifting vortex is driven by the $\beta$-gyres [94], which is a secondary circulation of a dipole structure triggered by an initial symmetric vortex. In a cyclone, for example, fluid on the east side of the cyclone is advected northward and thus loses relative vorticity in order to satisfy PV conservation. Similarly, the west side of the cyclone gains relative vorticity. As a result, a dipole of relative vorticity anomaly emerges with cyclonic gyre west to an anticyclonic gyre, superposed upon the initial cyclone. The orientation of the dipole axis dominates the direction of the $\beta$-drift. Initially, the dipole is directed to the North but later it is rotated anticlockwise by the primary monopole such that the entire vortex propagates to the Northwest.

At later stages theoretical studies showed a different scenario of evolution between an isolated vortex (strongly nonlinear such as a stirred vortex) and a non-isolated vortex (weakly nonlinear such as a siphoned vortex). The isolated cyclone usually settles down by traveling along a rest latitude at a constant speed, out of the range of linear Rossby waves (since wave radiation and vortex decaying are assured if propagating at any linear Rossby wave speed according to studies on Rossby solitons [94]). The rest latitude could be qualitatively predicted by a balance between the planetary vorticity gain during vortex translation and its initial relative vorticity. For a vortex of weak nonlinearity, Rossby wave radiation is commonly observed. Wave radiation mechanism is immediately clear when one applies repeatedly the gyre generation mechanism on each of the secondary $\beta$-gyres. It shows that a series of gyres of alternating sign in vorticity are formed to the east of the initial vortex; in

contrast, on the west side all the gyres have the same sign as the initial vortex. The original signal is then propagating westward, leaving a vorticity tail of alternating sign, which is the quasi-geostrophic scenario of the beta-drift described in early analytic studies[46, 45]. In a steady state, the energy lost from a vortex by wave radiation can be analytically calculated [82], and as a response the vortex shrinks in size.

Rather than focusing on the details of the evolution of the vortex itself, which has been covered in many theoretical studies, the dynamics of the radiated wave were investigated in Chapter 4 in the dissertation. This study is motivated by the success of the $\beta$-plume theory in describing the spectrum evolution of the $\beta$-plane turbulence (as shown in Chapter 2), and also by the recent studies supporting the significant control of nonlinear oceanic vortices by linear wave dynamics [129, 14, 15]. Now the question is to what extent are the linear dynamics important, not to the nonlinear vortex, but to the far field where Rossby waves prevail. As mentioned previously, perturbation on a $\beta$-plane gives rise to a $\beta$-plume. Compared to the baroclinic buoyancy forcing, which was commonly used to generate the $\beta$-plume[117], wave radiation by a traveling vortex in a barotropic case is easy to realize in the lab. It is interesting to see how the $\beta$-plume dynamics work in such an idealized situation.

The main difficulty in the previous laboratory experiments on this subject was capturing the vortex and the far field simultaneously with the same resolution; however, the AIV technique employed here allows one to do so. Results from laboratory experiments were used as the benchmark to compare with numerical simulation. Moreover, a linear theory similar to that in Chapter 2 was derived, which shows a wave pattern closely resembling

those observed in the lab experiments and the numerical simulation.

## 1.4 Overview of the thesis structure

Chapter 2 presents the results from the laboratory experiments on barotropic $\beta$-plane turbulence. Spectral analyses for the baroclinic turbulence in a two-layer system is presented in Chapter 3. Then in Chapter 4, an idealized problem, i.e. wave radiation by a cyclonic vortex traveling on a $\beta$-plane, is investigated using laboratory experiments along with numerical simulations. Chapters 2 and 4 are two published papers in *Physics of Fluids*, while the results in Chapter 3 were submitted to *Ocean Modelling*. Final conclusions are contained in Chapter 5.

# Chapter 2

# $\beta$-plane Turbulence

This chapter is an adapted version of a journal article published in Physics of Fluids (Zhang and Afanasyev 2014).

## 2.1 Introduction

Two-dimensional $\beta$-plane turbulence is an important conceptual model of turbulent flows on rotating planets where the variation of the Coriolis parameter with latitude is of importance for motions of large scale. Before we consider the $\beta$-plane flows, we shall review briefly an even more basic concept of two-dimensional turbulence without the $\beta$-effect (see review papers [37, 20]). A Kolmogorov-type theory [69] predicts that a forced-dissipative two-dimensional turbulence develops a dual cascade, where energy is transferred from the scale where the forcing is applied to larger scales while enstrophy is transferred to smaller scales. The slopes of energy spectrum predicted by the theory are $-5/3$ in the energy range and $-3$

in the enstrophy range. Note that numerical simulations [48] performed at high Reynolds number showed that the theoretical $-5/3$ scaling law can be steepened to $-2$ when long-lived vortex cores develop in the flow. An extension beyond two-dimensionality is provided by rotating shallow water (RSW) theory [133] which takes into account vortex stretching, the effect of the finite radius of deformation, and inertia-gravity waves. Recent laboratory experiments with RSW turbulence on the $f$-plane [2] showed similarity to two-dimensional turbulence with the spectral slopes of approximately $-5/3$ and (somewhat steeper than) $-3$. These experimental results are in agreement with results of numerical simulations [132]. An effect of asymmetry between anticyclonic and cyclonic vortices with the anticyclonic vortices prevailing was observed in the experiments [2]; this is one of the effects that make RSW turbulence different from its two-dimensional counterpart. In order to eliminate the $\beta$-effect, a cylindrical tank with a paraboloidal bottom of the same shape as that of the rotating water surface was employed in [2]. Note that in the present work we use a similar apparatus but with an inverted paraboloidal bottom to increase $\beta$-effect rather than to eliminate it.

While two-dimensional and RSW turbulence are isotropic in the horizontal plane, the turbulence with the $\beta$-effect is not. Even when the forcing is isotropic, an anisotropy develops in the form of zonal jets. This phenomenon is of great interest for applications to atmospheric circulations on gas giants [40] as well as to recently discovered jets in the Earths oceans [80, 81, 109]. Note that while on Jupiter and Saturn jets are prominent features of the circulation, the oceanic jets are often lost in a much stronger eddy field and can be revealed only as a result of time averaging of the observed fields. In the spectral representation, the

anisotropy of the flows manifests itself in the concentration of energy at the $k_x = 0$ axis in the wavenumber plane. Theory [98, 118] predicts that the zonal spectrum of the flow defined as $E_Z = E(k_x = 0, k_y)$ has a slope of $-5$. Here $E(k_x, k_y)$ is a two-dimensional energy spectrum which will be properly defined later in this article. Baroclinic instability is a major underlying process which generates eddies in atmospheric and oceanic large-scale turbulent flows. At a mature stage of its development baroclinic instability becomes equilibrated such that the flow becomes barotropic to a significant degree. The barotropic component of the flow is coupled to the baroclinic one [34]. The barotropization process allows one to use barotropic models for the investigation of turbulent flows. Observations of $\beta$-plane turbulence in numerical simulations of different authors suggested that barotropic flows tend to generate somewhat weaker jets than those in baroclinic flows. It seems that an energy source capable of sustaining persistently high energy level in the flow is an important factor of strong jet formation [99, 86]. In baroclinic flows (even when the dynamics is mainly barotropic) the energy source is provided by eddies slowly releasing their available potential energy.

Turbulent flows on the $\beta$-plane have been a subject of study in laboratory experiments by different authors. Zonal jets were observed in the experiment [126] where the flows were induced locally by a vertically oscillating disk. A formation of a zonal flow was also observed in [39] who generated the flow by a periodic excitation of sources and sinks. In a series of experiments, Sommeria forced eastward and westward jets by pumping fluid radially from a ring of sources to a ring of sinks at the bottom of the tank [111, 112, 110]. This forcing

created prominent jets with multiple eddies in the background. Marcus [76] used numerical simulations in a setup similar to Sommeria's experiments to further investigate the properties of the jets, in particular, an asymmetry between the eastward and westward jets. Recent experiments [4, 108] showed that a pattern of zonal jets can be formed westward of the area where perturbations are located. The perturbations were created by buoyancy sources. It was shown that the jets formed via a $\beta$-plume mechanism. A $\beta$-plume is an almost zonal circulation consisting of two zonal jets flowing in opposite directions. The circulation is formed via radiation of Rossby waves by a localized perturbation [4, 116, 38]. In the experiments by [4] eddies eventually filled a significant area of the domain. However, the jets were still prominent in this turbulent flow. While it is clear how a single localized perturbation can create jets to the west of its location, it is much less clear how eddies in a turbulent flow cooperate to sustain jets. Rather than using a forcing applied in a limited area of the domain, one can use a uniformly distributed forcing to create an eddy field in the entire domain. Ref. [5] used an electromagnetic (EM) forcing to generate a turbulent flow on the polar $\beta$-plane. In EM experiments the Lorentz force is created by using a combination of permanent magnets located at the bottom of the tank and the horizontal electric current flowing through the layer of conducting fluid. It showed the formation of zonal flows in the forced-dissipative $\beta$-plane turbulence, but they were somewhat limited by the size of the apparatus. Further EM experiments in a setup similar to that used in [5] were performed recently [42]. A different kind of distributed forcing was used in experiments on the Coriolis platform [92]. The authors used convective forcing where the surface of the water in the

tank was sprayed with saline water. More dense saline water formed small-scale convective plumes descending to the bottom thus creating small-scale turbulence. A system of zonal jets was observed. The slope of the turbulent energy spectrum was measured to be close to $-5/3$ in the energy range as predicted by theory. Since the forcing was at very small scale, the enstrophy range was not resolved in those experiments.

In what follows, we describe laboratory experiments on a rotating table with the (topographic) $\beta$-effect. Two experiments were performed; in the first experiment the forcing was barotropic and generated by the EM method while in the second experiment the forcing was baroclinic and generated by heating the fluid at the bottom of the tank. The purpose of these experiments was to investigate the properties of the flows including their spectral characteristics both in wavenumber space and in frequency-wavenumber space. We used a relatively large tank of 110 cm diameter and an intermediate/small-scale forcing (approximately 1 cm) in order to observe the dual cascade including the energy and enstrophy intervals. Our optical altimetry system allowed us to measure fields with high spatial and temporal resolution which was necessary for spectral analyses. The dynamics of Rossby waves in the forced-dissipative $\beta$-plane turbulence is elucidated. Our experimental results show how idealized theory or numerical simulations hold in application to real flows. In Section 2.2 we describe the setup of our apparatus as well as the optical altimetry technique used to measure the gradient of the surface elevation field, from which we obtain the velocity and vorticity fields. In Section 2.3 the results of the experiments and their analyses are reported. Concluding remarks are given in Section 2.4.

## 2.2 Laboratory apparatus and techniques

The experiments were performed in a cylindrical tank of radius $R_t = 55$ cm installed on a rotating table (Figure 2.1). The tank was filled with water and rotated in an anticlockwise direction at a rate of $\Omega = 2.32$ rad $\cdot$ s$^{-1}$. In the first experiment with an EM forcing an inner container in the form of a cylinder with a paraboloidal bottom was inserted into the tank and was concentric with the tank. The radius of the inner cylinder was $R_i = 45$ cm. The bottom was an inverted paraboloid such that the bottom topography was $h_b = H_b + c_b r^2$, where $H_b = 8$ cm, $c_b = 4 \times 10^{-3}$ cm$^{-1}$, and $r$ is the radial distance. The flow was generated by an electromagnetic method. For this purpose the bottom of the inner container was fitted uniformly at $l_f = 4.6$ cm intervals with about 300 neodymium magnets. The magnets were in a form of square tiles $l_m = 2.5$ cm wide. The vertical component of the magnetic field of each magnet was of the order of 1 Tesla. The poles of the magnets were oriented such that their polarity alternated between neighbouring magnets. Two electrodes made from chemically neutral material (graphite) were placed on the outside of the wall of the inner container to prevent bubbles forming on the electrodes to enter the area of interest. Small holes were drilled in the wall to allow an electric current to flow through the fluid inside. A voltage of approximately 117 V DC was applied to the electrodes. The electrical conductivity of water was increased by adding NaCl in the amount of approximately 35 parts per thousand. The resulting electric current between the electrodes was about 15 Amp. A combination of the horizontal electric current with the vertical magnetic field results in the Lorentz force acting in the horizontal direction perpendicular to that of the electric current. The Lorentz force

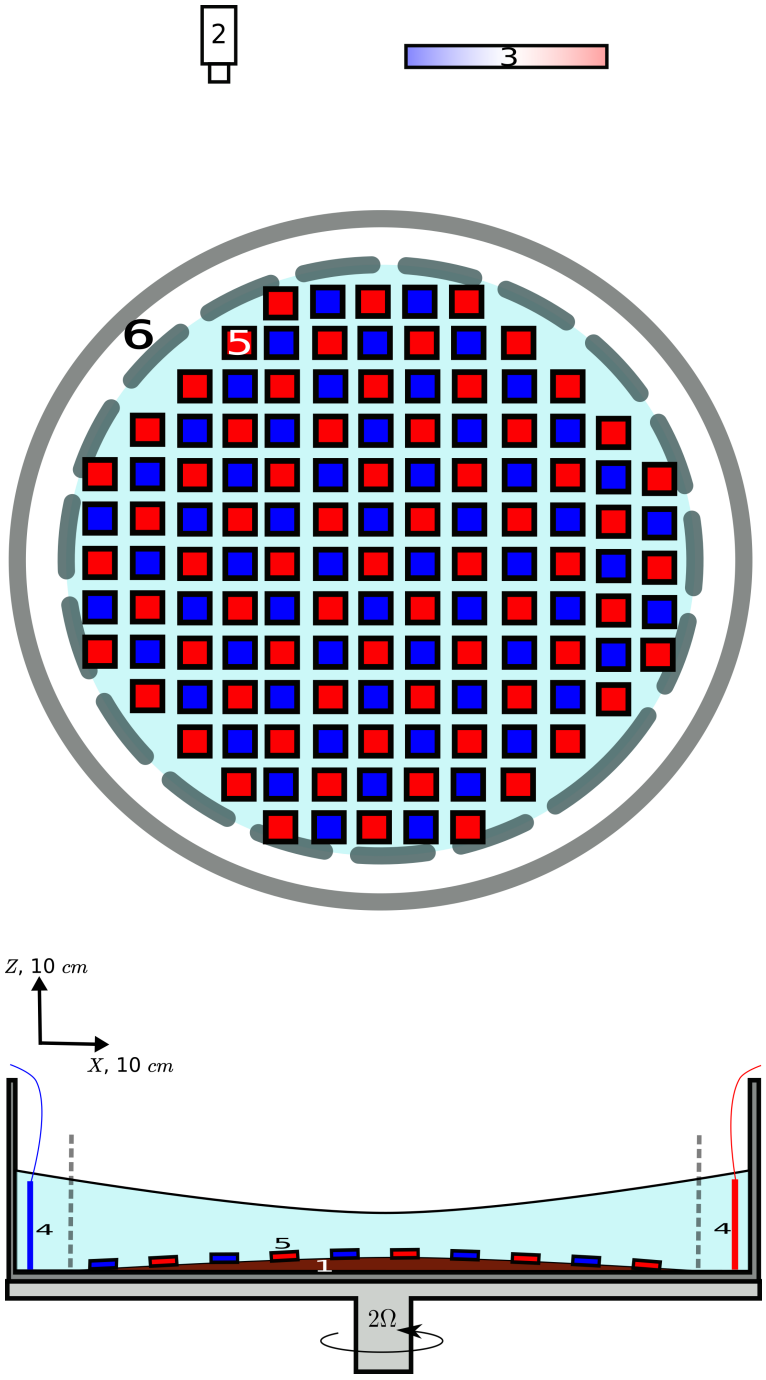


Figure 2.1: Sketch of the experimental setup: rotating tank and the inner container (gray dashed lines) with the paraboloid false bottom (1) filled with water, video camera (2), high brightness TFT panel displaying the color mask (3), electrodes (4), and permanent magnets (5). A bird's view of the paraboloid false bottom where an array of magnets was placed is shown as the insert (6) between the camera and the tank.

is a body force which acts on the fluid above each magnet. The effective vertical extent of the volume where the force is applied is approximately equal to the width of a magnet. The electromagnetic method provides an effective means of forcing the fluid in a controlled manner. For more details see [77, 3].

The second experiment was performed in the tank without the cylindrical insert or the paraboloidal bottom. The flow was forced thermally using a heating wire at the bottom of the tank. The wire was fitted in an approximately uniform pattern such that the distance between the neighbouring segments of the wire was about 4.5 cm. The power provided by the heater was 2300 W. The height $h$ of the water surface under a solid-body rotation varies quadratically with the distance $r$ from the axis of rotation

$$h(r) = H_0 + \frac{\Omega^2}{2g}(r^2 - \frac{R_t^2}{2}), \tag{2.1}$$

where $H_0$ is the depth of the layer in the absence of rotation and $g$ is the gravitational acceleration. The depth of the water in the tank is given by the difference between the height of the surface and bottom topography, $H = h - h_b$ . In the EM experiment the water was quite shallow ($H = 2.5$ cm) at the center of the tank and deep ($H = 14$ cm) near the wall at radius $R_i$. In the heating wire experiment the bottom of the tank was flat ($h_b = 0$) and the water depth varied between 4 cm at the center and 12 cm near the wall ($r = R_t$) with the average depth $H_0 = 8$ cm. The dynamical equivalence of the varying depth of the layer to the varying Coriolis parameter, results from the conservation of the potential vorticity (PV) defined as $q = (\zeta + f_0)/H$. Here $f_0 = 2\Omega$ is the Coriolis parameter and $\zeta$ is the vertical component of the relative vorticity. A local Cartesian coordinate system can be introduced

at some reference radius $r_0$ such that a positive x-direction is to the East and a positive y-direction is to the North. Note that the North Pole is at the center of the tank rotating anticlockwise. The $\beta$-plane with the linearly varying Coriolis parameter, $f = f_0 + \beta y$, can then be introduced by defining the $\beta$-parameter as

$$\beta = \frac{4(\Omega^2/2g + c_b)\Omega r_0}{H(r_0)}. \tag{2.2}$$

The Altimetric Imaging Velocimetry (AIV) system was used to observe perturbations of the surface and to measure two components of the gradient $\nabla\eta = \left(\frac{\partial\eta}{\partial x} + \frac{\partial\eta}{\partial y}\right)$ of the surface elevation $\eta$ in the horizontal plane $(x,\ y)$. The AIV technique was described in detail in [8]. The $\nabla\eta$ field was measured with a spatial resolution of approximately 2 vectors per millimeter such that the total size of the array was $1900 \times 1900$, with a temporal resolution of 5 fields per second. The surface velocity of the flow can be determined from the measured gradient of surface elevation using shallow water and quasi-geostrophic approximations which yields

$$\mathbf{V} = \frac{g}{f_0}\mathbf{n} \times \nabla\eta - \frac{g}{f_0^2}\frac{\partial}{\partial t}\nabla\eta - \frac{g^2}{f_0^3}J(\eta, \nabla\eta), \tag{2.3}$$

where $\mathbf{V}$ is the horizontal velocity vector, $\mathbf{n}$ is the vertical unit vector, and $J(A, B) = A_x B_y - A_y B_x$ is the Jacobian operator. The first term on the RHS of Equation (2.3) is the geostrophic velocity. The second and third terms are due to transient and nonlinear effects and their relative importance is determined by the temporal Rossby number $Ro_T = 1/(f_0 T)$ and the Rossby number $Ro = V/(f_0 L)$, respectively. Here $T$ is the time scale of the flow evolution, while $V$ and $L$ are velocity and length scales of the flow.

## 2.3 Experimental results and analyses

We performed two experiments with different forcing which will be referred to as the barotropic (Bt) experiment with the EM forcing and the baroclinic (Bc) experiment with the thermal forcing. Note that in fact an ensemble of EM experiments with similar values of the dimensional control parameters was performed. The mean water depth and the forcing strength varied within approximately 15% between the experiments. Here we give the results which are typical for the ensemble. In what follows we discuss the Bt and Bc experiments in parallel emphasizing the similarities and differences between them.

### Observation of the flow evolution

Figure 2.2 (multimedia view) shows a typical evolution of the flow in the forced regime and after the forcing stops in the Bt experiment. The initial period, shortly after (3 s) the forcing was switched on, is shown in top row of Figure 2.2. A regular array of vortices of alternating sign is formed such that there are approximately 10 vortices of the same sign across the tank. Note that initially the vortices between the adjacent magnets have double cores (Figure 2.2(c)) because the magnets generate vortex dipoles directed along parallel lines in the directions opposite to each other. However, these cores rapidly coalesce into a single vortex. The flow is much stronger in the center of the tank where the water is shallow. The second row of Figure 2.2 shows the flow at the end of the relatively long forcing period when the flow is at approximately steady state, the turbulence is fully developed; strong vortices are abundant. They are no longer attached to specific locations although some indications

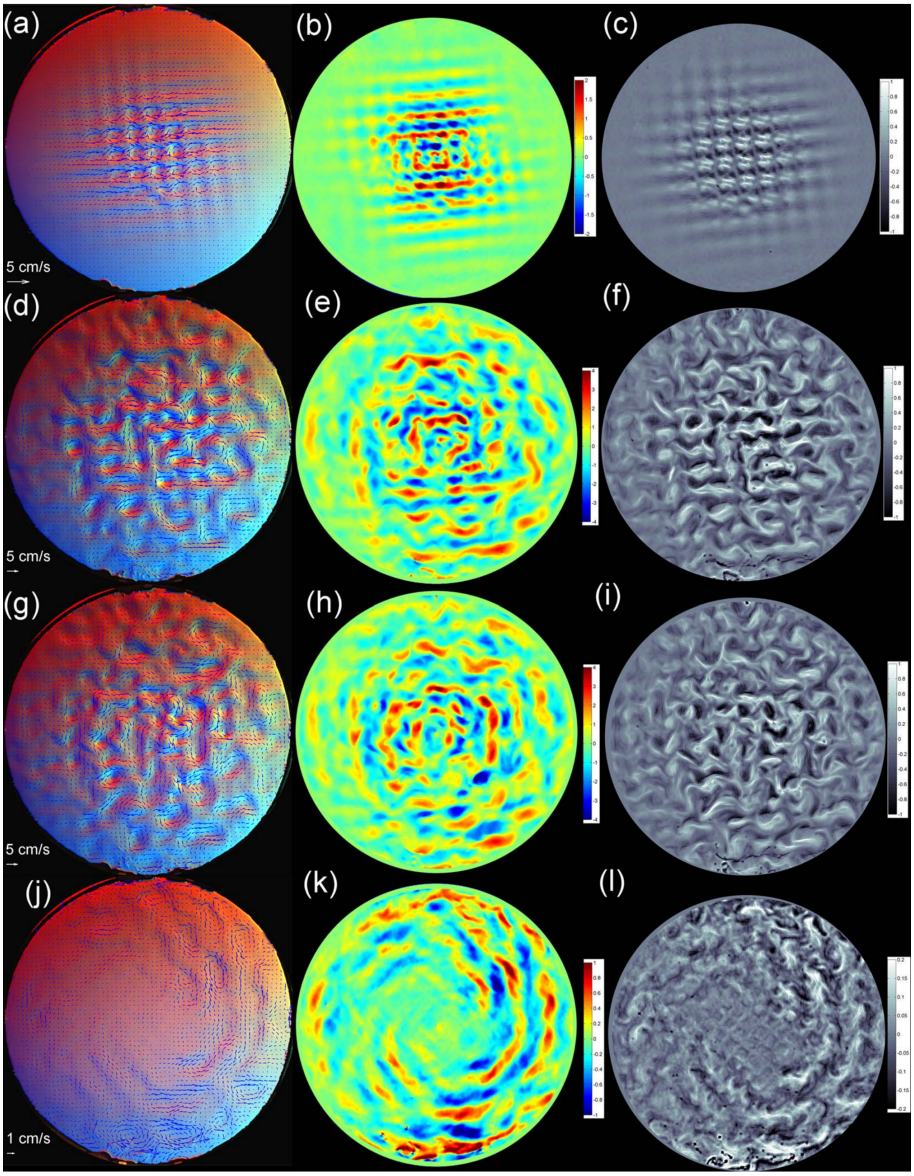


Figure 2.2: Evolution of the barotropic turbulent flow with the $\beta$-effect visualized by AIV in the Bt experiment (Multimedia view): initial period shortly after the forcing starts, $t = 2\ s$ (a-c), stationary forced turbulence, $t = 380\ s$ (d-f) and decaying turbulence, $t = 2\ s$ (g-i) and $t = 30\ s$ after the forcing was stopped (j-l). The first column of panels shows velocity vectors superposed on color altimetry images. The velocity scale is given in the lower left corner of each panel. The second column shows the x-component of velocity, $v_\theta$, while the third column shows the dimensionless vorticity $\zeta/f_0$ varying from negative values (black, anticyclonic) to positive values (white, cyclonic).

of the regular forcing array can be seen in the azimuthal velocity map (Figure 2.2(e)). The typical size of the vortices corresponds well to the forcing scale. The third row of Figure 2.2 shows the flow shortly after the forcing was switched off. The vortices are still prominent, yet a certain alignment of vortices in the zonal direction is also evident. The map of the x-component of velocity, u, shown in Figure 2.2(h) indicates the emergence of zonal jets in the flow. Finally, the bottom row of Figure 2.2 shows the decaying flow at the very end of the experiment when vortices no longer dominate but zonal currents are still present. Note an interesting spiral pattern of jets in this flow. Most likely, the spiral manifests the Rossby waves with spiral crests which occur above the isolated underwater mountains [96, 97]. In our case, the entire water layer with shallow water in the center and deep water at the wall of the tank, can be considered as that above a mountain. We will illustrate this effect using linear Rossby wave theory in section Section 2.3.

Figure 2.3 shows the azimuthal velocity $v_\theta$ and relative vorticity $\zeta/f_0$ in the Bc experiment. The warm water rises from the wire at the bottom to the surface forming a narrow upper layer initially aligned along the wire. This layer is lens-like in cross section and is unstable with respect to baroclinic/frontal instability. It rapidly breaks into small eddies of typical radius of approximately 1 cm. The size of the eddies is most likely determined by baroclinic radius of deformation. These eddies possess available potential energy which then is slowly released into the system. During the forcing period strong vertical convective motions induced by hot wires is the main source of energy. The effect of this forcing can be described by the $\beta$-plume theory which was developed in application to hydrothermal vents

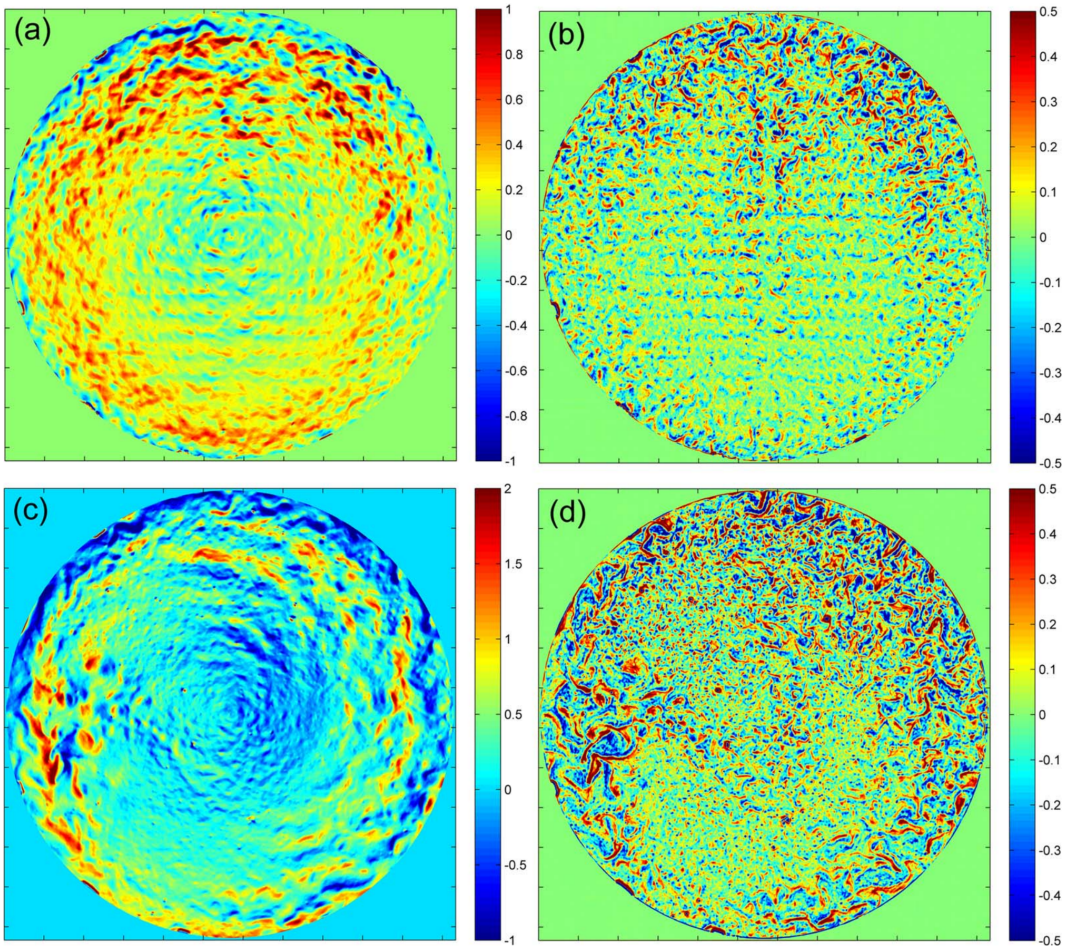


Figure 2.3: Baroclinic flow generated by thermal forcing in the Bc: forced turbulence, $t = 360$ s (a, b) and decaying turbulence, $t = 40$ s after the forcing was stopped (c, d). Panels (a) and (c) show the x-component of velocity, $v_\theta$; panels (b) and (d) show the dimensionless vorticity $\zeta/f_0$.

in the ocean [116]. When the forcing was switched off, the eddies available potential energy becomes the main source which can sustain the flow for a very long time. Panels (a) and (b) of Figure 2.3 show the flow during the forcing period. Comparison with the Bt experiment reveals that jets are more prominent in this case most likely because the eddies are much smaller and weaker than those induced by magnets. It is interesting to note that this observation agrees with the results of high-resolution numerical simulations [106]. These authors reported that the onset of strong jets in the forced-dissipative barotropic $\beta$-plane turbulence occurs when the jet and eddy vorticity maxima are comparable, but jets weaken when the eddies are too strong. During the decay period the azimuthal velocity map (Figure 2.3(c)) shows a spiral pattern similar to that in Bt experiment. However, the relative vorticity map (Figure 2.3(d)) reveals that the eddies are much more alive in this experiment compared to the barotropic one. Note also that a cyclonic circulation develops in the tank which causes the asymmetry between the strength of the eastward and westward jets. This circulation is due to a gradual accumulation of warm water at the periphery of the tank. The circulation then occurs as suggested by the thermal wind balance with a radial gradient of density.

In order to investigate whether the flow becomes stationary during the forcing period, we measured kinetic energy $\bar{E} = \mathbf{V}^2/2$ and enstrophy $\bar{\zeta^2}$ in both experiments. Time series of mean values of both quantities are shown in Figure 2.4. In the Bt experiment both energy and enstrophy fluctuate around some stationary levels during the forcing period. In the Bc experiment both quantities continue to rise slowly over a long period of time until they reach approximately steady levels at $t = 2500$ s. After the forcing stops both energy

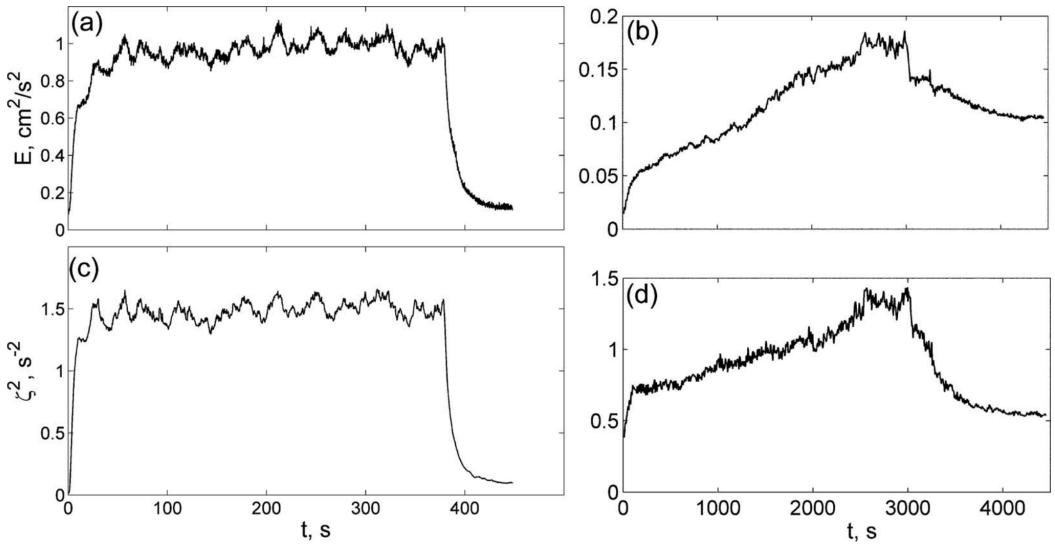


Figure 2.4: Kinetic energy $\bar{E}$ and enstrophy $\bar{\zeta^2}$ averaged over the tank versus time in the Bt (a, c) and Bc (b, d) experiments.

and enstrophy decay rapidly in the Bt experiment while in the Bc experiment the decay is much slower. The measurements of energy decay allow us to quantify dissipation in the experiments. Dissipation in the rotating fluid can be interpreted in terms of friction in the bottom Ekman layer and viscosity in the bulk of the layer. The rate of change of the mean energy in the system is given by

$$\frac{d\bar{E}}{dt} = -2\alpha\bar{E} - \nu\bar{\zeta^2}, \tag{2.4}$$

where bottom friction is parameterized by a linear term with linear drag coefficient $\alpha$ and $\nu$ is the kinematic viscosity of fluid. The coefficient $\alpha$ can then be determined as $\alpha = -[d(ln\bar{E})/dt + \nu\bar{\zeta^2}/\bar{E}]/2$. The coefficient $\alpha$ is approximately equal to 0.05 s$^{-1}$ in the Bt experiment. The coefficient was measured immediately after the forcing stops using the spatial-averaged energy and enstrophy data shown in Figure 2.4(a) and (c). Note that the

contribution of bulk viscosity constitutes only 11% of the total rate of change of energy such that most of the energy is dissipated at the bottom. Ekman dissipation is not uniform across the domain; the system loses energy faster in the shallow area in the center than in the deeper layer at the periphery. Alternatively, a theoretical estimate $\alpha = \sqrt{\Omega\nu}/H$ can be obtained from the bottom Ekman layer theory. Theory gives $\alpha = 0.06$ s$^{-1}$ in the center and $\alpha = 0.01$ s$^{-1}$ at the wall of the tank in the Bt experiment.

The presence of an energy source (baroclinic eddies) in the flow during the decay period in the Bc experiment makes it impossible to measure $\alpha$ using mean energy and enstrophy data. In this experiment we have to rely on the theoretical estimate only. It gives more uniform distribution with radius than that in the Bt experiment with $\alpha$ varying between 0.03 s$^{-1}$ in the center and 0.01 s$^{-1}$ at the wall. A bulk value (averaged over the area) is $\alpha = 0.02$ s$^{-1}$.

An important control parameter in a forced-dissipative turbulence is the rate, $\epsilon$, at which the forcing supplies energy to the system. In a stationary flow this energy is subsequently removed from the system by dissipation at the same rate. Assuming that, immediately after the forcing stops, the energy dissipation rate remains the same as it was during the forcing, $\epsilon$, can be estimated as

$$\epsilon = -\frac{d\bar{E}}{dt} \approx 2\alpha\bar{E}. \tag{2.5}$$

using Equation (2.5) but neglecting the dissipation due to bulk viscosity. The value of $\epsilon$ in the Bt experiment is 0.1 cm$^2$/s$^3$ while in the Bc experiment $\epsilon = 0.006$ cm$^2$/s$^3$, these values are calculated by differentiating spatial-averaged energy with respect to time during

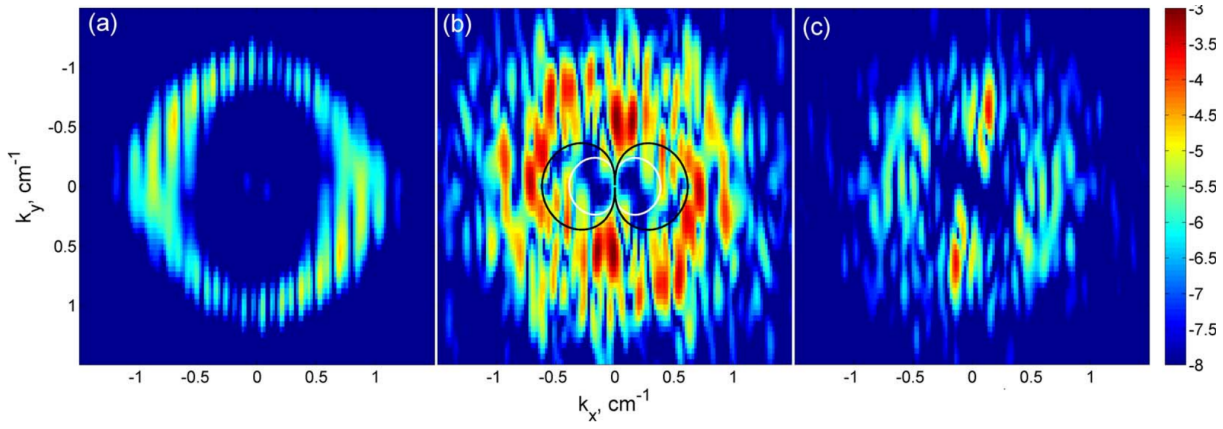


Figure 2.5: Evolution of the two-dimensional energy spectrum in the Bt experiment. The scale on the right shows the logarithm of relative energy (normalized by spatial averaged energy in the tank), in $k_x - k_y$ wavenumber space at (a) $t = 4$ s, (b) $t = 382$ s from the start of the experiment and at (c) $t = 12$ s after the forcing was switched off. The white line in panel (b) shows $k_R$ given by Equation (2.10) while the black line shows $k_\beta$ given by Equation (2.11).

the decaying regimes in the experiments.

## Energy spectra in wavenumber space

Further insight into the dynamics of the turbulent flow can be provided by an analysis of its spectral characteristics. For a Fourier decomposition it is convenient to use the Cartesian coordinates. We chose the local coordinate system which corresponds to the $\beta$-plane centered at the reference radius $r_0 = 2R_i/3$. The domain is of halfwidth $R_i/3$ such that we cut off the central part of the tank. The velocity vectors obtained by altimetry (in the global Cartesian coordinates) are mapped into the local coordinate system to obtain the velocity $\mathbf{u} = (v_\theta, v_r)$ where $v_\theta$ is the West-East and $-v_r$ is the South-North component of the velocity vector.

Two-dimensional energy spectrum is given by

$$E(k_x, k_y) = \frac{1}{2}|\mathbf{u}(k_x, k_y)|^2, \tag{2.6}$$

where $\mathbf{k} = (k_x, k_y)$ is the wavenumber vector and $\mathbf{u}(k_x, k_y)$ represents the discrete Fourier transform of the velocity vector. Figure 2.5 shows the evolution of the two-dimensional spectrum in the Bt experiment. The spectrum shortly after the forcing starts (Figure 2.5(a)) is in the form of a ring and is approximately isotropic. Note that since there are initially approximately 10 vortices of the same sign across the tank, the forcing wavelength is $\lambda_f = 2R_i/10 = 9$ cm (equal to twice the distance between the magnets). The forcing wavenumber is then $k_{xf} = k_{yf} = 2\pi/\lambda_f \approx 0.7$ cm$^{-1}$ which corresponds well to the size of the ring in Figure 2.5(a). Figure 2.5(b) shows the spectrum of a stationary forced flow. An important feature of the spectrum is the concentration of energy at the line $k_x = 0$ which, in physical space, is an indication of zonal jets. Finally, panel (c) in Figure 2.5 shows the spectra of the decaying flow when the system is no longer driven to isotropy by forcing. Strong anisotropy develops with most of the energy concentrated in zonal motions at $k_x = 0$ and $k_y \approx 0.7$ cm$^{-1}$. In physical space, vortices decay while zonal jets become more prominent.

Figure 2.6 shows the two-dimensional spectrum in the Bc experiment. Initially (Figure 2.6(a)) the strongest signal is at approximately $k \approx 1$ cm$^{-1}$ which corresponds to the spacing between the segments of the wire. The second, albeit weaker ring is visible at $k \approx 2.2$ cm$^{-1}$. This wavenumber corresponds to the small scales of baroclinic eddies formed as a result of baroclinic instability. Eventually, energy cascades towards smaller wavenumbers, and concentrates as well near the line $k_x = 0$. Figure 2.6(b) shows the spectrum after

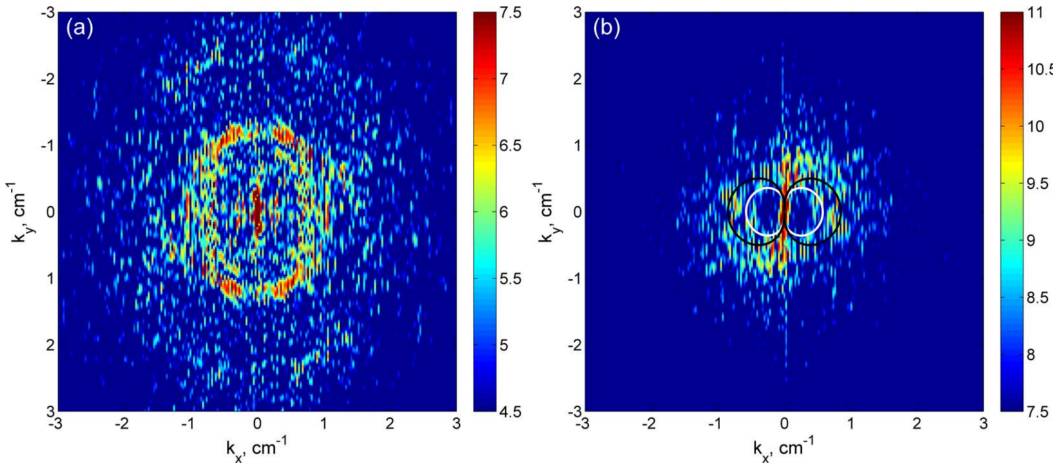


Figure 2.6: Two-dimensional energy spectrum in the Bc experiment in the beginning of the experiment at (a) $t = 35$ s and at (b) $t = 37$ s after the forcing was switched off. The white and black lines show $k_R$ and $k_\beta$, respectively.

the forcing was switched off. The spectrum is qualitatively similar to that in the Bt experiment (Figure 2.5(c)). Solid white and black lines in Figure 2.5(b) and Figure 2.6(b) show the anisotropic Rhines wavenumber, $k_R$ and a wavenumber $k_\beta$ respectively. These wavenumbers are determined using a synchronization condition for turbulence and Rossby waves which requires the frequency of the turbulent motions to be equal to the frequency of the waves. The frequency of the Rossby waves is determined by their dispersion relation

$$\omega(k_x, k_y) = \frac{-\beta k_x}{k^2 + R_d^{-2}}, \tag{2.7}$$

where $k^2 = k_x^2 + k_y^2$ and $R_d = \sqrt{gH}/f_0$ is the radius of deformation. Turbulence, on the other hand, does not have a dispersion relation; the frequency of turbulent motions can be determined using different considerations. [98] used the root-mean-square (rms) velocity of

vortices to obtain

$$\omega = V_{rms}k. \tag{2.8}$$

Turbulence is assumed to be isotropic with wavenumber $k$ characterizing a vortex arrangement in the turbulent flow. Alternatively, the characteristic frequency of forced turbulence can be obtained using the energy injection rate $\epsilon$ as a main control parameter. In the upscale energy cascade with spectral slope $-5/3$, the time required for a fluid parcel to move a distance $1/k$ is $\epsilon^{-1/3}k^{-2/3}$ ([122]) which gives

$$\omega = \epsilon^{1/3}k^{2/3}. \tag{2.9}$$

Equating turbulent frequencies Equation (2.8) or Equation (2.9) to the Rossby wave frequency Equation (2.7) and solving for the wavenumber, we obtain the Rhines wavenumber

$$k_R = (\frac{\beta}{V_{rms}})^{1/2}\cos^2\theta, \tag{2.10}$$

and the $k_\beta$ wavenumber

$$k_\beta = \frac{\beta^3}{\epsilon}^{1/5}\cos^{3/5}\theta. \tag{2.11}$$

Here $\theta$ is the angle in the wavenumber plane such that $\cos\theta = k_x/k$. In the derivations of the wavenumbers we assumed $R_d$ to be large and ignored it in the dispersion relation. Physically, $k_\beta$ can be interpreted as a wavenumber where turbulence starts feeling the $\beta$ effect. A match between the eddy frequency and the Rossby wave frequency allows the turbulence to emit Rossby waves. The energy cascade, however, does not stop there and continues towards smaller wavenumbers, especially towards $k_x = 0$ [121]. The Rhines wavenumber determines

where the Rossby waves are emitted most effectively by turbulent motions of characteristic velocity $V_{rms}$. Note that this velocity is determined by the balance of the energy supply by the forcing and its withdrawal by dissipation. The Rhines wavenumber represents a boundary which divides small-scale turbulence and large-scale wave dominated motions. The lines in Figure 2.5(b) and Figure 2.6(b) are calculated using parameters measured in the experiments: $V_{rms} = \sqrt{\bar{E}}$ and $\epsilon = 2\alpha\bar{E}$. It is clear that the space inside the dumbbells, where the Rossby waves dominate, contains reduced energy. The lines showing anisotropic wavenumbers $k_R$ and $k_\beta$ in Figure 2.5(b) and Figure 2.6(b) represent certain frequencies selected using the criteria specified by Equation (2.8) and Equation (2.9). However, turbulent motions emit waves with the entire spectrum of frequencies. Rossby wave emission by a localized perturbation is described by the $\beta$-plume theory [116, 38]. The $\beta$-plume approach can be used to show that a two-dimensional spectrum of turbulence evolves towards an anisotropic state similar to that observed in Figure 2.5(b) and Figure 2.6(b). The emission of Rossby waves occurs due to a forcing in the RHS of a linearized quasi-geostrophic equation

$$\frac{\partial}{\partial t}(\nabla^2 - R_d^2)\eta + \beta\frac{\partial \eta}{\partial x} = F, \tag{2.12}$$

where $\eta$ is the surface elevation. The forcing is isotropic with a known spectrum. In particular, an isotropic small-scale turbulence with the developed (due to nonlinear triad interactions) $-5/3$ type energy cascade can be considered as forcing for this purpose. Note that [76] used a forcing which modeled small-scale convective plumes in an atmosphere in their numerical simulations of the quasi-geostrophic equation. They showed that the cascade of energy from small to larger scales occurred and a system of zonal jets was produced. Here

we skip the nonlinear cascade and consider only the Rossby waves generated by the vortices produced by the cascade. A solution for the Fourier transform of the surface elevation $\eta$ can be obtained as

$$\eta(k_x, k_y) = \frac{iF(k_x, k_y)}{k_x \beta}[\exp(-i\omega t) - 1], \tag{2.13}$$

where $F(k_x, k_y)$ is the forcing and $\omega$ is the frequency of the Rossby waves given by the dispersion relation Equation (2.7). Geostrophic velocity is obtained from the surface elevation as

$$\mathbf{u}_g(k_x, k_y) = \frac{g}{f_0}(ik_y, -ik_x)\eta(k_x, k_y), \tag{2.14}$$

and the two-dimensional energy spectrum is then calculated using Equation (2.6). Figure 2.7 shows the evolution of the spectra generated by an isotropic Gaussian forcing

$$F(k_x, k_y) = \exp(-\frac{(k - k_f)^2}{0.04}), \tag{2.15}$$

where $k_f = 1$ cm$^{-1}$ is the forcing wavenumber. The ring-like Gaussian forcing approximately models the forcing applied by the magnets in our experiment. The dimensional control parameters used to calculate the spectrum shown in Figure 2.7 are chosen to have the same values as in the Bt experiment. Figure 2.7 shows that the energy spectrum develops from the initially isotropic spectrum towards a strongly anisotropic one where the energy is concentrated at the $k_x = 0$ line similar to that in the experiment (in Figure 2.5 and Figure 2.6(b)).

One-dimensional energy spectrum is an important characteristic of a turbulent flow which can be easily obtained from the two-dimensional spectrum such as that shown in Figure 2.5

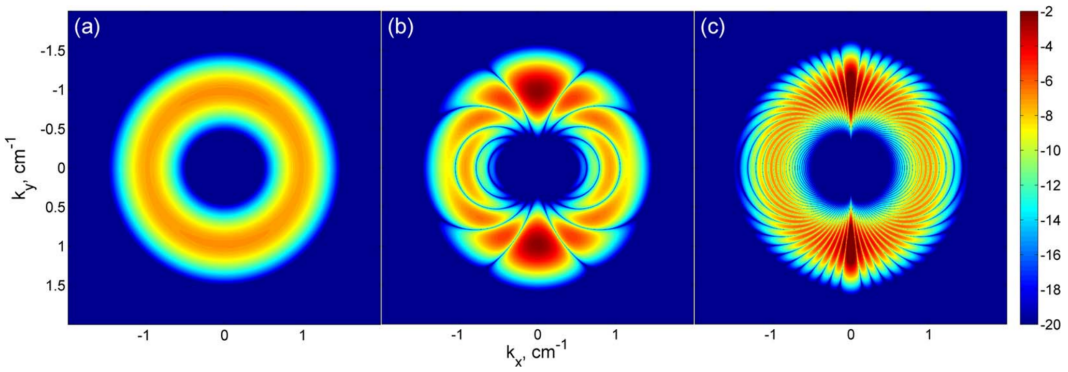


Figure 2.7: The evolution of the energy spectrum given by the theoretical solution Equation (2.14). The scale on the right shows the logarithm of energy in $k_x - k_y$ wavenumber space at (a) $t = 10$ s, (b) $t = 100$ s, and at (c) $t = 500$ s. The dimensional parameters are $k_f = 1$ cm$^{-1}$ , $f_0 = 4.64$ s$^{-1}$, $\beta = 0.2$ cm$^{-1}$s$^{-1}$ , and $R_d = 18$ cm.

and Figure 2.6. The one-dimensional (isotropic) spectrum is defined as

$$E(k) = 2\pi k \bar{E}(k_x, k_y). \tag{2.16}$$

where the two-dimensional spectrum $\bar{E}(k_x, k_y)$ is averaged over angle $\theta$ in wavenumber domain. In anisotropic $\beta$-plane turbulence, a zonal spectrum can be defined as

$$E_z = \bar{E}(k_x = 0, k_y). \tag{2.17}$$

Theory predicts a steep zonal spectrum [98, 119]:

$$E_z(k_y) \sim \beta^2 k_y^{-5}, \tag{2.18}$$

while the non-zonal spectrum is expected to have a slope of $-5/3$ as predicted by Kolmogorov theory for two-dimensional turbulence. Figure 2.8 shows both the isotropic spectrum $\bar{E}(k)$ and zonal spectrum $E_Z(k_y)$ in the Bt experiment while Figure 2.9 shows the spectra in the

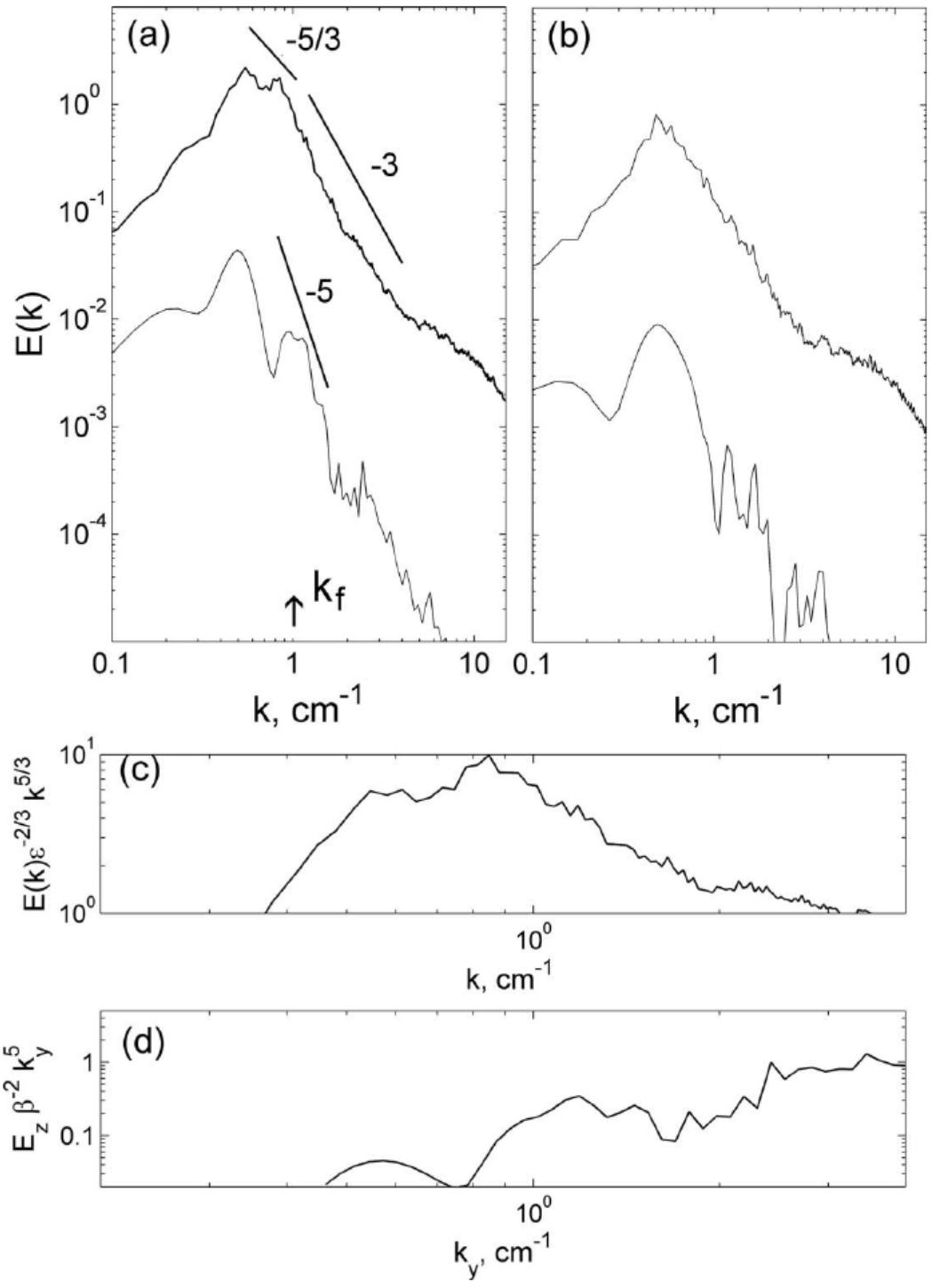


Figure 2.8: The one-dimensional spectra of relative energy (normalized by spatial average energy in the tank) in forced (a) and in decaying turbulence (b) with the barotropic electromagnetic forcing: energy $E(k)$ (upper curve) and zonal energy $E_Z(k_y)$ (lower curve). Arrows indicate the forcing wavenumber $k_f$. Panel (c) and (d) shows the Kolmogrov constants of $E(k)$ and $E_Z(k_y)$ in (a).

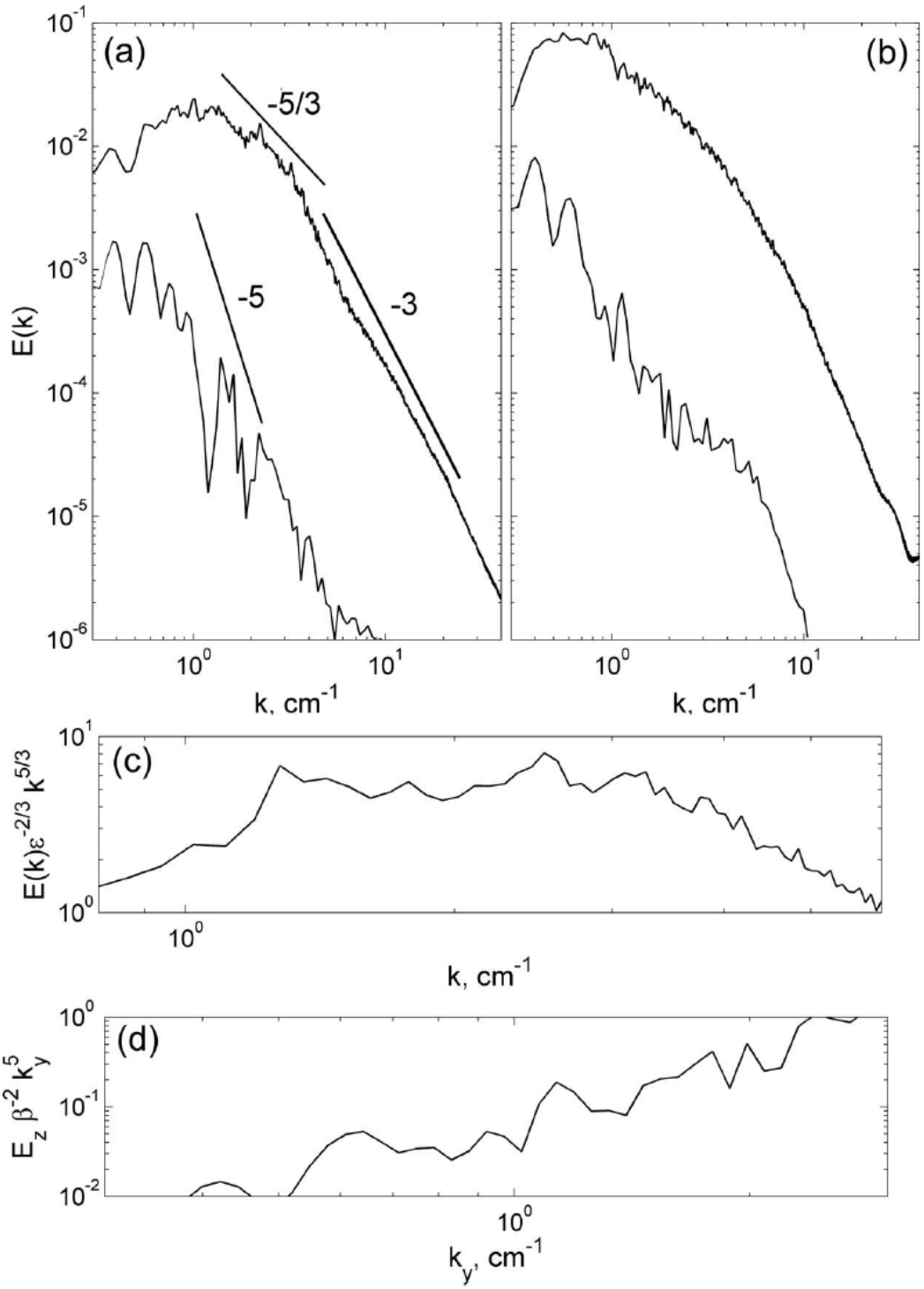


Figure 2.9: The same as before but for the flows with the baroclinic thermal forcing.

Bc experiment. In both experiments, in the forced-dissipative regime the isotropic spectrum shows a good agreement with the predictions of the two-dimensional turbulence theory. The enstrophy and energy ranges are separated by a forcing wavenumber. In the Bt experiment the isotropic forcing wavenumber is $k_f = \sqrt{2}k_{xf} \approx 1$ cm$^{-1}$ (arrow in Figure 2.8). In the Bc experiment the forcing wavenumber corresponds to the size of the baroclinic eddies and is more difficult to pinpoint precisely but it is clearly smaller than the forcing wavenumber in the Bt experiment. In the enstrophy range ($k > k_f$) the slope of the energy spectra is close to $-3$ in both experiments. The slope in the energy range ($k < k_f$) is close to $-5/3$ in both experiments. Note, however, that the energy range in the Bt experiment is quite limited. The RSW experiments by [2] showed that the finite radius of deformation can be a limiting factor for the cascade (see also [37]). In the ring-shaped domain we use for measuring spectra the values of $R_d$ vary between 13 cm and 26 cm (bulk value 20 cm) and between 15 cm and 23.5 cm (bulk value 21 cm) in the Bt and Bc experiments, respectively. These values are similar to those in [2] and so are the lowest limits of the energy range.

The zonal spectra $E_Z(k_y)$ show peak at low wavenumbers and decline, albeit somewhat flatter than $-5$, at larger wavenumbers. Compensated energy spectra in the form $E(k)\epsilon^{-2/3}k^{5/3}$ are shown in panel (c) of Figures 2.8 and 2.9. The compensated spectra in both experiments exhibit plateaus at the energy range that allows us to determine the value of the Kolmogorov constant, $C \approx 6$ and 5 in the Bt and Bc experiments, respectively. Compensated zonal spectra, $E_Z(k_y)\beta^{-2}k_y^5$ (Figure 2.8(d) and Figure 2.9(d)), however, vary with $k_y$ and do not allow an accurate measurement of a constant in the theoretically predicted

$-5$ law. The spectra in Figure 2.8 and Figure 2.9(b) were measured after the forcing was switched off and the flows were decaying. In the Bt experiment the levels of energy decrease; the shape of the zonal spectrum remains almost the same while the isotropic total energy spectrum loses its $-5/3$ range and exhibits a uniform slope of approximately $-3$ from the low wavenumber cut-off at $k \approx 0.5$ cm$^{-1}$ towards larger wavenumbers. In contrast, in the Bc experiment the flow is still driven by the baroclinic energy source at relatively large wavenumbers even when the direct forcing was switched off. The $-5/3$ range remains and is even wider than that in Figure 2.9(a).

Figure 2.10 shows the evolution of the energy spectra $E(k)$ after the forcing was switched off in each experiment. The levels of energy drop and the peaks of spectra shift to lower wavenumbers. To characterize the shift of the spectral peak it is useful to consider the energy-weighted mean wavenumber $k_E$ defined as

$$k_E = \int_0^\infty kE(k)dk / \int_0^\infty E(k)dk$$

Wavenumber $k_E$ provides a measure of the energy containing scale. Evolution of $k_E$ just before and after the forcing was stopped is shown in Figure 2.10(c, d). In both Bt and Bc experiments the energy-weighted mean wavenumbers stay at some constant level during the forcing and then drop to a lower level when the forcing was stopped. Similar behaviour was also observed in previous EM experiments[5].

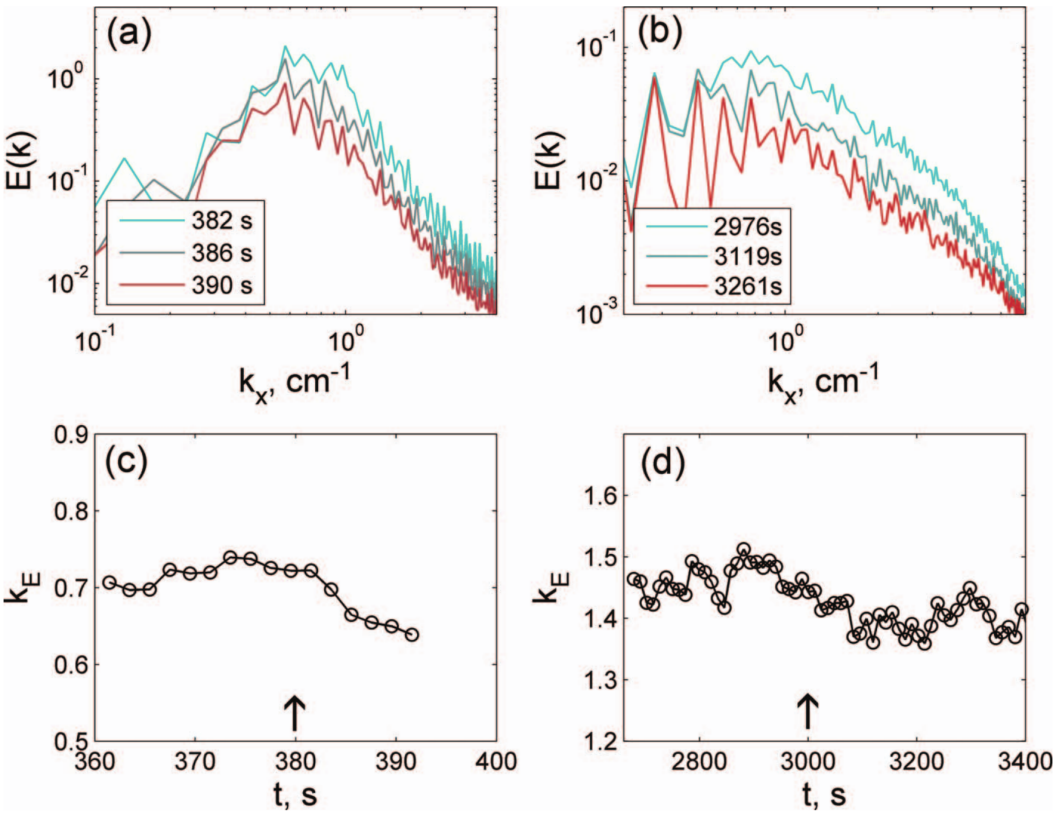


Figure 2.10: Evolution of the one-dimensional energy spectra (a, b) and the energy-weighted mean wavenumber $k_E$ (c, d) in decaying turbulence in the Bt (left column) and Bc (right column) experiments. Arrows indicate time when the forcing was switched off in each experiment.

## Frequency-wavenumber space and Rossby waves

In his pioneering paper on $\beta$-plane turbulence Rhines [98] predicted that Rossby waves should dominate at low wavenumbers below the wavenumber $k_R$. In what follows we shall provide experimental evidence of the Rossby waves in our experiments. It is not easy to identify waves in a turbulent flow. One way to do that is to use the fact that Rossby waves have a distinct dispersion relation Equation (2.7). The dispersion relation shows in particular a well-known

property, namely the westward phase propagation of the Rossby waves. Figure 2.11(a, b) shows the x-component of velocity, $v_\theta$, measured along a circle of radius $r_0 = 2R_i/3$ and $r_0 = 2R_t/3$ at different times during the Bt and Bc experiments respectively. The Hovmoller plot in Figure 2.11 shows $v_\theta$ in gray scale with distance along the circle in the horizontal and time in the vertical axes. The human eye is good at identifying patterns and it is easy to see a pattern of features aligned in oblique straight lines in these plots. These features are perturbations of the velocity u and they propagate in the negative x-direction, to the west. The slope of the lines then gives the phase velocity of the waves. Similar measurements performed at different radii $r_0$ show that the Rossby waves present almost everywhere in the tank except for the center.

The dispersion relation Equation (2.7) can be used in a more direct way to identify the spectral signature of the Rossby waves. Figure 2.12 shows the energy spectra in a frequency-wavenumber domain in both Bt and Bc experiments. To calculate the spectra we measured the velocity $(u, v)$ along the circle $r_0$ during a long time period (100 lab days and 3 lab years in the Bt and Bc experiment, respectively.) when the flow is forced and then performed the Fourier transform in time and in distance, $x$, along the circle. The resultant spectra show some interesting features of the flow. In the Bt experiment where the forcing was relatively strong and fixed in space, high energy motions are mostly concentrated at almost zero frequencies with hot spots at $k_x \approx \pm 0.8$ cm$^{-1}$, close to forcing wavenumber, and at $k_x = 0$. These high-energy, almost stationary motions radiate towards higher frequencies. In contrast, zero-frequency motions are not so obvious in the Bc experiment and main energy

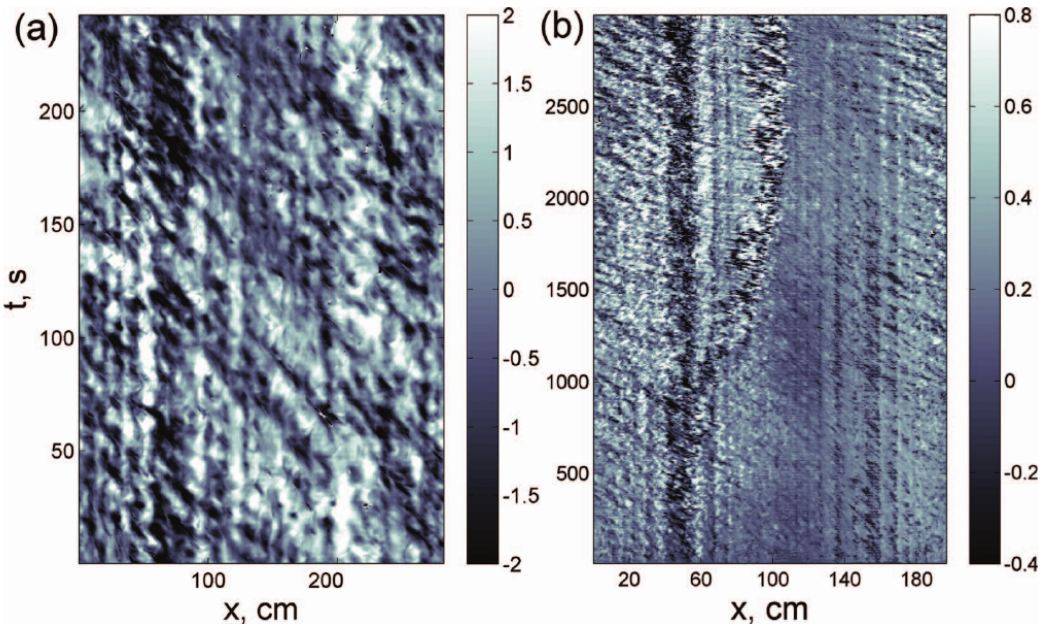


Figure 2.11: Velocity $v_\theta$ measured along a circle of radius $r_0$ equal to two thirds of the radius of the domain at different times in the Bt (a) and Bc (b) experiments. The gray scale shows $v_\theta$ in cm/s.

is concentrated in a plume extending to higher frequencies. The distribution of spectral energy at higher frequencies is clearly asymmetric with respect to the wavenumber $k_x$ in both experiments. Most of the energy is at negative $k_x$ which indicates that westward propagating waves dominate in the flow. The white lines in both panels in Figure 2.12 show the Rossby waves dispersion relation Equation (2.7) calculated with different values of $k_y$. The upper curves are calculated with $k_y = \pi/R_i = 0.07$ cm$^{-1}$ (Bt experiment) and $k_y = 0.06$ cm$^{-1}$ (Bc experiment) which correspond to largest possible wavelengths that fit across the tank. These curves provide an upper limit for the frequencies of the Rossby waves. The lower curves are calculated with the wavenumber $k_y = 0.7$ cm$^{-1}$ equal to the forcing wavenumber. Thus,

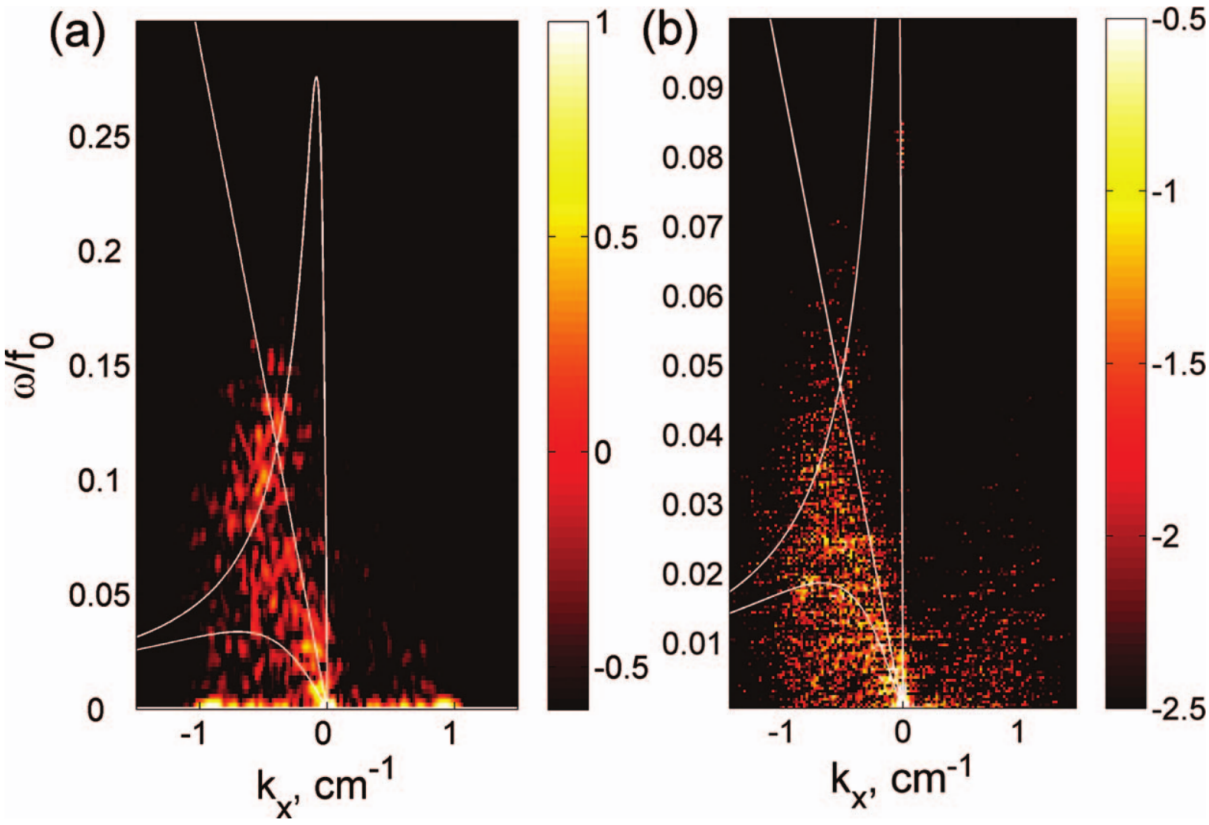


Figure 2.12: The relative energy (normalized by the spatial-averaged energy) spectrum in the frequency-wavenumber space. The scale shows the logarithm of energy. The frequency is normalized by the Coriolis parameter $f_0$ . White curves show the Rossby wave dispersion relation Equation (2.7) with $k_y = 0.07$ cm$^{-1}$ and $R_d = 20$ cm (a), and $k_y = 0.06$ cm$^{-1}$ and $R_d = 19$ cm (b) (upper curves); and with $k_y = 0.7$ cm$^{-1}$ and $R_d = 20$ cm (a), $k_y = 0.7$ cm$^{-1}$ and $R_d = 19$ cm (b) (lower curves). The solid straight lines shows turbulent frequency given by Equation (2.8) with $V_{rms} = 1.34$ cm/s (a) and $V_{rms} = 0.4$ cm/s (b).

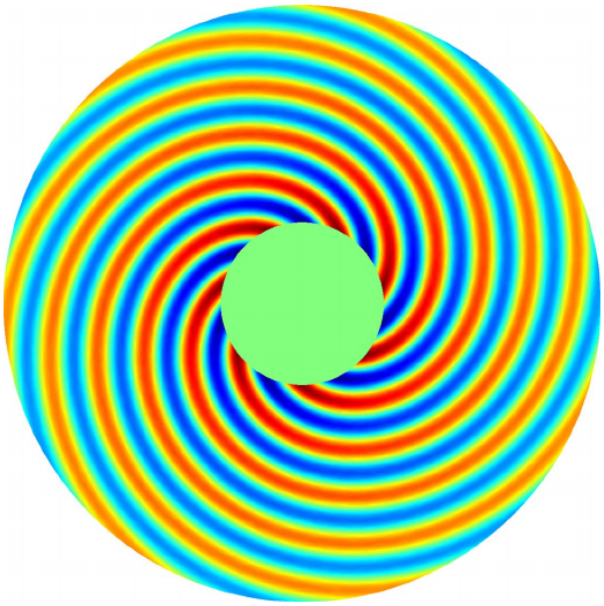

Figure 2.13: Rossby wave with spiral wavecrests propagating towards the center of the domain and represented by a solution in the form of the Hankel function.

most of the Rossby waves that can be excited in this system should be in between these two lines. According to [98] waves are excited most effectively at frequencies given by the turbulence dispersion relation Equation (2.8). The straight white lines in Figure 2.12 show Equation (2.8); there is indeed some concentration of energy along these lines.

Let us return now to the spiral pattern of jets that we pointed out earlier in Figure 2.2(k) and Figure 2.3(c). The spiral patterns were observed in the decaying flows. The energy is dissipated faster in the center of the domain where water is shallow. Therefore, we can expect propagation of energy from the periphery where the turbulence is still active towards the center. Turbulent eddies excite Rossby waves which can be described by linear theory. Here, however, we need to use a polar domain rather than a regular $\beta$-plane. Linearised

quasi-geostrophic equation similar to Equation (2.12) but in polar coordinates $(r, \theta)$ can be written as

$$\frac{\partial}{\partial t}(\nabla^2 - R_d^{-2})\eta + 2\gamma\frac{\partial \eta}{\partial \theta} = 0. \tag{2.19}$$

Here we use a so-called polar $\beta$-plane such that either the Coriolis parameter varies quadratically with distance from the pole on a rotating planet, $f = f_0 - \gamma r^2$ , or water depth varies quadratically with radius in the laboratory setting. In the latter case the coefficient $\gamma$ is defined as

$$\gamma = \frac{2\Omega(\Omega^2/2g + c_b)}{H_0 - H_b}. \tag{2.20}$$

Looking for the solution of Equation (2.19) in the form $\eta = \Psi(\kappa r)\exp(im\theta - i\omega t)$ one obtains a dispersion relation for the Rossby wave on a polar $\beta$-plane [99]:

$$\omega = \frac{2\gamma m}{\kappa^2 - R_d^{-2}}. \tag{2.21}$$

Radial dependence is given by either the Bessel function $\Psi(\kappa r) = J_m(\kappa r)$ or the Hankel functions $H_m^{(1)}(\kappa r)$ and $H_m^{(2)}(\kappa r)$. The former case corresponds to standing waves while the latter case describes waves propagating either inwards or outwards. Figure 2.13 shows the Hankel wave with spiral wavecrests which corresponds to wavemode $m = 8$, $\kappa = 0.73$ cm$^{-1}$. The particular values of the wavenumbers were chosen to match the pattern with that observed in the Bc experiment (Figure 2.3(c)). Thus, this simple linear analysis allows one to see where the experiments are in the relevant wavenumber space.

## 2.4 Discussions and conclusions

In this work, we have shown experimental evidence that zonal jets occur both in forced-dissipative and in decaying turbulent flows on the topographic $\beta$-plane. The jets are latent in the forced-dissipative case if the forcing is strong and eddies dominate; the jets in our Bt experiment are similar in this respect to oceanic jets which can only be revealed by filtering and time-averaging of the velocity fields [80, 81]. The jets are stronger, relative to the eddies, in the Bc experiment where the forcing was weaker. The jets become prominent in the decaying regime in both experiments, when the flow is no longer driven to isotropy by strong forcing.

Numerical simulations of $\beta$-plane turbulence by [52, 51, 118, 106] showed that the ratio $R_\beta = k_\beta/k_R$ controls the regime of the flow. When $R_\beta$ is large enough ($R_\beta > 2$), the flow is in a so-called zonostrophic regime when the jets are a dominant feature of the flow. The jets on gas giants satisfy the criterion of zonostrophy. When $R_\beta$ is less than approximately 1.5, the flow is in a viscous regime. A regime between the viscous and zonostrophic regimes ($1.5 < R_\beta < 2$) is transitional. The jets in the Earths oceans seem to be in the transitional regime and so are the jets in our Bt experiments where $R_\beta \approx 1.7$.

The measurements of the energy spectrum in the wavenumber space demonstrated that the spectrum evolves from initially almost isotropic one to an anisotropic spectrum of a typical dumbbell form which was previously observed in numerical simulations [122]. The evolution of the experimental spectrum is in a qualitative agreement with that predicted by a $\beta$-plume theory. The energy cascades towards $k_x = 0$ and nonzero $k_y$ close to the forcing

wavenumber.

Investigations of the energy spectra in the frequency-wavenumber domain revealed an asymmetry of the spectra with respect to the sign of the zonal wavenumber $k_x$. This asymmetry can be explained by the westward propagation of the Rossby waves. Some concentration of wave-energy was observed along the line $\omega = V_{rms}k$ as predicted by [98]. The asymmetric frequency-wavenumber energy spectra, which are qualitatively similar to those observed in our experiments, were also observed in the middle latitude ocean [129]. In the ocean,the spectra also indicated a predominantly westward propagation of perturbations. Significant energy was distributed along the so-called non-dispersive line given by $\omega = \beta R_d^2 k$. This line was tangent to the first-mode baroclinic Rossby wave dispersion curve. Note that in our experiments the Rossby waves were barotropic, so the non-dispersion line represented a barotropic Rossby wave speed for the longest spatial scale (the maximum wave speed allowed by local water depth). However, in our case, shorter waves with wavenumbers close to the forcing wavenumber were more prominent than long non-dispersive waves.

In this work we do not distinguish between jets and almost zero-frequency Rossby waves with nearly zonal wavecrests. In Figure 2.2(j-l) and Figure 2.3(c) the (slightly spiralling) jets can be directly associated with Rossby waves emitted by eddies in the decaying flows. Moreover, we suggest that $\beta$-plume mechanism or emission of low-frequency waves by perturbations is the underlying mechanism in jets formation by $\beta$-plane turbulence. This notion is illustrated in Figure 2.7 showing the evolution of the two-dimensional spectrum towards zonal motions solely by linear wave emission. Further sustaining the jets by turbulence will

perhaps involve nonlinear mechanisms where a self-organization of the jet-eddy system is important and results in fluxes of momentum from eddies to jets.

# Chapter 3

# Baroclinic Turbulence on the Polar $\beta$-plane in the Rotating tank: Down to Submesoscale

This chapter is an article submitted to Ocean Modelling (Zhang and Afanasyev 2016).

## 3.1 Introduction

General ocean circulation contains motions of different scales; the energy source for the most energetic motions is often at mesoscale and is due to the baroclinic instability. It is well-known that energy is transferred from the source scale to larger scale via the inverse cascade mechanism predicted by the dual-cascade theory [69]. However, the energy must also

be transferred to small scales where it is ultimately dissipated by viscosity. Submesoscale motions are believed to be important in providing the direct energy cascade via specific instabilities such as inertial, shear, frontal or baroclinic instabilities. Submesoscale motions are typically narrow currents or small eddies characterised by the relatively high values of strain and relative vorticity (Rossby numbers $\mathcal{O}(1)$). These currents are often frontal and have strong horizontal gradients of buoyancy and are surface-intensified. Technical progress in the recent years allowed researchers to make detailed measurements of flows at submesoscale in the ocean (e.g. [107, 25]) as well as to perform high-resolution numerical simulations (e.g. [26, 27, 25, 32, 55]).

Here we employ a complementary tool, the laboratory experiment, to study turbulent baroclinic flows with the $\beta$-effect. The experiments study the dynamics of the real fluid as opposed to "digital" fluid in numerical simulations where there might always be some degree of approximation due to unavoidable subgrid parametirizations. The challenge of field studies is to make comprehensive measurements on sufficiently large scale; the same challenge exists in the laboratory experiment. We use optical altimetry which not unlike the satellite altimetry, provides a global coverage and yet is able to resolve the motions of smallest scale present in the flow. The obvious disadvantage of the laboratory experiments remain, of course, a relatively large dissipation.

In what follows we use the data obtained in the previous experiments [78] where a two-layer baroclinic flows on the topographic $\beta$-plane were studied. The shear between the layers supported baroclinic instability; the eddies and filaments created by the instability

were affected by the $\beta$-effect and, in turn, generated Rossby waves and alternating zonal jets. These flows can be considered as a laboratory model of the Antarctic Circumpolar current or the Gulf Stream or Kuroshio extentions. A comprehensive analyses of the general dynamics of the flows was given in [78]; here we investigate spectral characteristics of the flows from the large and meso-scales down to smaller scales which can be related to the oceanic submesoscale. The purpose is to clarify the dynamical processes which create spectral features over the entire range of wavenumbers and frequences. The distinct features of our flows include large scale zonal circulation, mesoscale meanders/eddies, Rossby waves and submesoscale filaments and eddies.

In Section 3.2 of this paper, we very briefly describe the setup of the laboratory apparatus as well as the altimetry technique since both were described in detail in previous publications. In Section 3.3 the methods used to calculate energy spectra both in the Cartesian and polar coordinates are described. The results of the spectral analyses are reported in Section 3.4 and concluding remarks are given in Section 3.5.

## 3.2 Laboratory techniques

Experiments were performed in a cylindrical tank installed on the rotating table. The tank of radius $R = 55$ cm was filled with water of depth $H = 10 \sim 12$ cm and was rotated aniclockwise with angular rate $\Omega = 2.3$ rad/s. The water in the tank was of salinity varying between $S = 10$ ppt and 45 ppt in different experiments. The flow was forced by injecting a

volume of 20 liters of fresh water along the wall of the tank. The injected water then formed a fresh layer on top of the saline layer [78].

Altimetric measurements were performed to obtain the horizontal gradient of the surface elevation, $\eta$ over the entire tank [8]. The data was measured on a regular grid in the global Cartesian coordinates $(X,\ Y)$ with the origin in the center of the tank. The smallest spatial scale resolved by the altimetry was approximately 0.2 cm after filtering the original data with the window of 5 by 5 pixels to reduce noise from the camera sensor. The fields of the surface elevation gradient, $\nabla\eta$, were recorded with frequency of 7 frames per second. Thus, the measured data had sufficient spatial and temporal resolution for the purpose of the spectral analyses reported in this paper.

The measured gradient allowed us to estimate the surface velocity, $\mathbf{V}$ in the quasi-geostrophic approximation using the following expression

$$\mathbf{V} = \frac{g}{f_0}\left(\mathbf{n}\times\nabla\eta\right) - \frac{g}{f_0^2}\frac{\partial}{\partial t}\nabla\eta - \frac{g}{f_0^3}J\left(\eta,\nabla\eta\right), \tag{3.1}$$

where $f_0 = 2\Omega$ is the Coriolis parameter, $\mathbf{n}$ is the vertical unit vector and $J\left(A,B\right)$ is the Jacobian operator. Note, that the first term in the RHS of Equation (3.1) is the geostrophic velocity. Thus, in the experiments $\nabla\eta$ or, alternatively, the pressure gradient, $\nabla p = \rho g\nabla\eta$ where $\rho$ is density of water and $g$ is the gravitational acceleration, is measured "exactly" while $\mathbf{V}$ is determined approximately and is more accurate when the flow is closer to being quasi-geostrophic. Typical values of the Rossby number, $Ro = |\zeta|/f_0$, were 0.2 or less in the experiments such that the condition of quasi-geostrophy was reasonably satisfied. Here $\zeta$ is the relative vorticity of the flow, $\zeta = curl\mathbf{V}\cdot\mathbf{z}$.

The free surface of the rotating fluid is a paraboloid such that in the tank with flat bottom the depth, $h$, of the fluid varies quadratically with the distance $r$ from the axis of rotation (the center of the tank). According to the conservation of potential vorticity, flows in the layer of depth varying with $r$ are dynamically equivalent to flows in a layer of uniform depth but with the Coriolis parameter varying with $r$. In the first-order approximation this dynamical equivalence can be represented by the so-called polar $\beta$-plane (or $\gamma$-plane) where the Coriolis parameter varies quadratically:

$$f = f_0 - \gamma r^2, \tag{3.2}$$

here $\gamma = \Omega^3/(gH)$. The center of the tank is the North pole of the polar $\beta$-plane. A traditional $\beta$-plane can also be introduced in "midlatitudes" where the Coriolis parameter varies linearly, such that $\beta$-parameter can be defined as [6]

$$\beta = \left(\frac{f_0}{h}\frac{dh}{dr}\right)_{r=r_0} = \frac{8\Omega r_0}{4R_d^2 + 2r_0^2 - R^2}, \tag{3.3}$$

where $r_0$ is the reference distance from the pole and $R_d = (gH)^{1/2}/f_0$ is the barotropic radius of deformation.

## 3.3 Methods of spectral analyses

The techniques of calculating two-dimensional (2D) and one-dimensional (1D) energy spectra using discrete Fourier transform in Cartesian coordinates are well known. The Fourier-Bessel transform in cylindrical polar coordinates, however, is used less often although it is a natural

choice for a circular polar domain such as our tank (e.g. [5]) or, perhaps, for a polar-to-midlatitudes domain of an ocean or the atmosphere. In what follows, we briefly describe the methods we used to obtain spectra in the wavenumber or in frequency domain using both of the transforms.

2D energy spectrum is defined as

$$E(k_x, k_y) = \frac{1}{2}|\mathbf{V}(k_x, k_y)|^2, \tag{3.4}$$

where $\mathbf{V}(k_x, k_y)$ represents the 2D discrete Fourier transform of the velocity vector field. In order to perform the Fourier transform we introduce a local Cartesian coordinate system with the origin at a reference radius $r_0 = 25$ cm such that the $x$ and $y$ axes are directed to the East and the North, respectively. We limit the meridional extent of our domain to be 34 cm. Thus, the polar area of the tank, where the $\beta$-plane approximation is invalid, as well as the wall area are excluded. The velocity field calculated from the altimetry measurements is interpolated into this coordinate system to obtain the zonal (x-) and meridional (y-) components of the the velocity vector.

1D energy spectrum is defined as

$$E(k) = 2\pi k \langle E(k_x, k_y) \rangle, \tag{3.5}$$

where

$$\langle E(k_x, k_y) \rangle = \frac{1}{\pi(\delta k^2 + 2k\delta k)} \int_0^{2\pi} \int_k^{k+\delta k} E(k_x, k_y) k dk d\phi \tag{3.6}$$

is the spectral energy averaged over a thin ring of width $\delta k$ and of inner radius $k = \sqrt{k_x^2 + k_y^2}$ in $k_x - k_y$ wavenumber space, and $\phi$ is the polar angle in this wavenumber space.

As an alternative to the local Cartesian coordinate system, a global (applicable to the entire tank) polar coordinate system $(r,\ \theta)$ can be introduced. The velocity field given by the altimetric measurements is interpolated into this coordinate system; the velocity vector is given by its azimuthal and radial components. Fourier-Bessel series is then a natural choice for spectral decomposition. The velocity is given by

$$\mathbf{V}(r,\theta) = \sum_{m=0}^{\infty}\sum_{n=0}^{\infty} \mathbf{B}_{mn} J_m(\frac{r}{R}\alpha_{mn}) \exp(im\theta), \tag{3.7}$$

where $J_m(r)$ is the Bessel function of order $m$, $R$ is the radius of the tank, and $\alpha_{mn}$ is the $n^{th}$ root of the Bessel function. The amplitude, $\mathbf{B}_{mn}$, of each mode $(m,\ n)$ is given by

$$\mathbf{B}_{mn} = \frac{2}{[RJ_{m+1}(\alpha_{mn})]^2} \int_0^R r\mathbf{V}(m,r) J_m(r\alpha_{mn}/R) dr, \tag{3.8}$$

where

$$\mathbf{V}(m,r) = \frac{1}{2\pi}\int_0^{2\pi} \mathbf{V}(\theta,r)\exp(-im\theta)d\theta$$

is the complex Fourier transform of the velocity along azimuthal direction at some radius $r$. A two-dimensional energy spectrum is then defined as

$$E(m,n) = |\mathbf{B}_{mn}|^2 J_{m+1}^2(\alpha_{mn}), \tag{3.9}$$

where $J_{m+1}^2(\alpha_{mn})$ is a weight coefficient required by the Parseval's indentity (see Appendix 3.A).

While the definition of the 2D spectrum in wavenumber space $(n,\ m)$ is straightforward, defining a 1D spectrum is more complicated. First, a 1D wavenumber analogous to the 1D (isotropic) wavenumber $k = \sqrt{k_x^2 + k_y^2}$ in the Cartesian system, must be introduced. In the

polar coordinates, it can be defined as $k_p = \alpha_{mn}/R$. Indeed, when the Laplace operator is applied on the basis function

$$F_{mn} = J_m(\frac{r}{R}\alpha_{mn}) \exp(im\theta), \tag{3.10}$$

it gives

$$\nabla^2 F_{mn} = \frac{\alpha_{mn}^2}{R^2} F_{mn}, \tag{3.11}$$

similar to that in the Cartesian system [19]. The discrete values of $k_p$ are obtained by sorting the 2D array $\alpha_{mn}$ into a linear sequence according to the values in $\alpha_{mn}$. Values of $E(m,\ n)$ corresponding to the linear sequence of $k_p$ can be used to obtain the 1D spectrum as follows:

$$E(k_p) = \frac{E(m,\ n)|_{sorted}}{\Delta k_p}, \tag{3.12}$$

where $\Delta k_p$ is the interval between two consecutive values of $k_p$ in the (irregular) sequence. Thus, the spectrum is defined as energy per unit wavenumber, as required. In practice, the 1D spectrum obtained after sorting requires some smoothing, especially at high wavenumbers. This can be done by interpolating the data into a regular sequence of $k_p$ after specifying an appropriate constant interval of the wavenumber.

Energy spectrum in the frequency-wavenumber domain, $E(\omega,\ k_x)$ can be defined as follows:

$$E(\omega,\ k_x) = \frac{1}{2}|\mathbf{V}(\omega,\ k_x)|^2, \tag{3.13}$$

where $\mathbf{V}(\omega,\ k_x)$ represents the discrete 2D Fourier transform of the velocity along the circle of some radius $r$ both in x-direction and in time. The 1D energy spectrum in the frequency domain, $E(\omega)$, can then be obtained by integrating $E(\omega,\ k_x)$ over $k_x$.

Energy spectra are sustained by transfers of energy either from smaller to larger wavenumbers (direct cascade) or in the opposite direction (inverse cascade) . The spectra themselves do not provide us with the information on the magnitude or direction of the energy cascades. This information can be provided by the investigation of the energy fluxes. We employ a modified filter-space technique (FST, [101]) in order to calculate the spatial distribution of the energy flux at different scales in physical space as well as to obtain the flux across different wavenumbers in spectral domain. The energy flux $\Pi$ is defined as

$$\Pi^l = -[(v_i v_j)^l - v_i^l v_j^l]\frac{\partial v_i^l}{\partial x_j}, \tag{3.14}$$

where the subscript $i/j$ denotes the $i^{th}/j^{th}$ component of the velocity vector $v$, summation over repeated indices is assumed, and the superscript $l$ denotes a low-pass-filtered field with scales smaller than $l$ removed. The filtering is performed by multiplying the corresponding velocity field with a Gaussian filter in wavenumber space followed by an inverse Fourier transform. The Gaussian filter in the wavenumber domain is defined as

$$G(k_x, k_y) = \begin{cases} \exp[-20(k-k_l)^4], & \text{if } k > k_l \\ 1, & \text{otherwise} \end{cases} \tag{3.15}$$

where $k = \sqrt{k_x^2 + k_y^2}$ is the isotropic wavenumber and $k_l = 2\pi/l$. Positive value of $\Pi^l$ represents downscale flux, i.e energy transfers from large scales to small scales, while negative value represents the inverse cascade. Summing the energy flux over the entire area of the flow we obtain the overall balance of the flux as a function of the cutoff wavenumber $k_l$, as shown in Figure 3.7.

## 3.4 Results

In what follows we analyse the data obtained in the set of experiments where turbulent baroclinic flows were generated on the topographic $\beta$-plane in the rotating tank. The injection of fresh water along the wall at the surface of saline layer generates a strong jet current flowing along the wall such that the wall is on its right. The fresh water layer is at this point wedge-shaped in cross section. The injection lasts for a relatively short time after which the flow is allowed to evolve freely. The wall ("coastal") current is unstable and forms large meanders and eddies which are injected into previously unstratified interior area of the tank. The upper fresh layer thus extends gradually towards the center of the tank. After the fast adjustment during the injection, the relatively slow phase of the adjustment includes slow radial flow in the upper fresh layer towards the center. The final equilibrium state with the upper layer of an uniform thickness, however, was never achieved in the experiments. The radial flow causes an azimuthal circulation as a consequence of the conservation of angular momentum. As a result, a velocity shear is sustained between the upper and lower layers. This creates conditions for the development of the baroclinic instability. The unstable flow continuously creates meanders, filaments and eddies. This is not unlike the bariclinic instability in the ocean which serves as an energy source at mesoscale. Figure 3.1 shows a typical view of the flow in one of the experiments. A strong meandering coastal current is clearly visible in the velocity field (arrows) in Figure 3.1(a). Features of smaller scale occupy the inner area of the tank. Panel b of Figure 3.1 shows a close view of the flow including a small cyclonic eddy and multiple filaments. More detailed spatial structure of the flow can

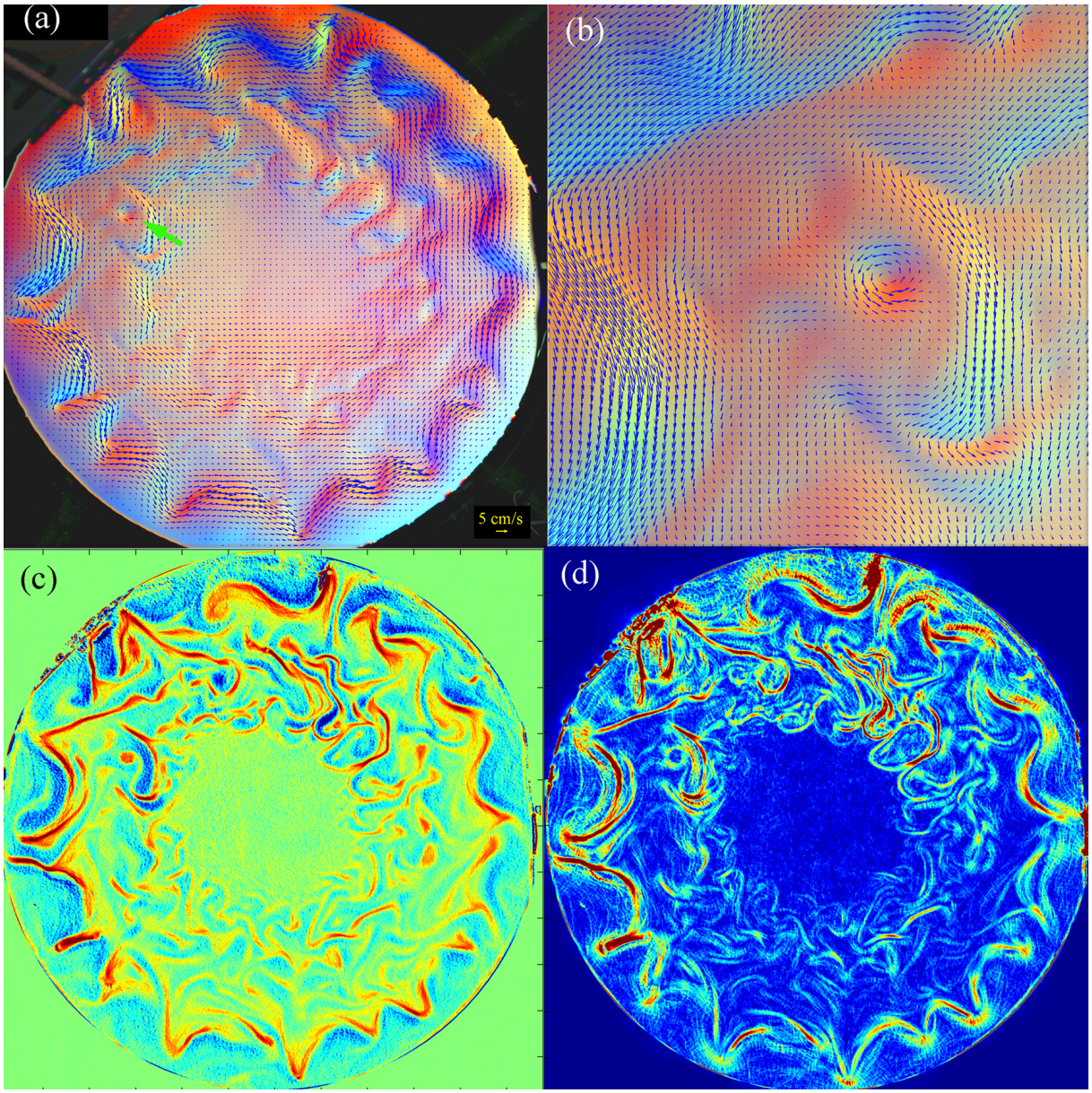


Figure 3.1: Baroclinic flow in the rotating tank at $t = 120$ s after switching off the fresh water source: (a) velocity (arrows) superposed on the altimetric color image; (b) magnified view of the vortex indicated by the green arrow; (c) dimensionless relative vorticity, $\zeta/f_0$ varying between -1 (blue) and +1 (red) and (d) dimensionless strain rate, $s/f_0$ varying between 0 (blue) and +1 (red). Lower layer salinity is $S = 20$ ppt.

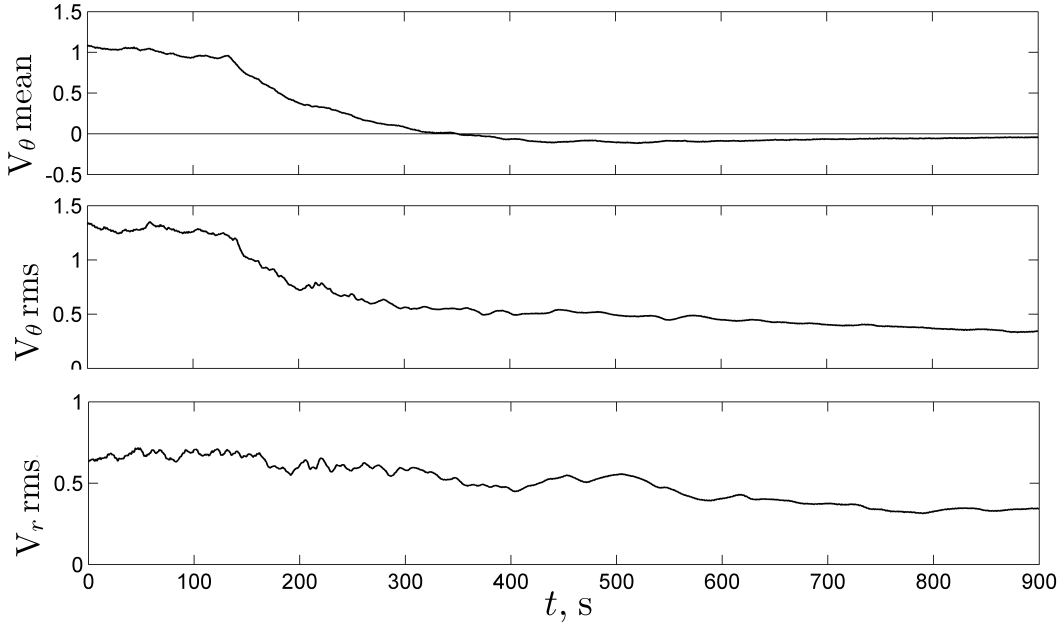


Figure 3.2: Time series of the mean azimuthal velocity, $V_{\theta,\ mean}$, rms azimuthal velocity, $V_{\theta\ rms}$, and rms radial velocity, $V_{r,\ rms}$. Time starts when the fresh water injection is stopped. Lower layer salinity is $S = 30$ ppt.

be revealed in the kinematic fields composed of the spatial derivatives of velocity. Panels c and d show the relative vorticity, $\zeta$, and the strain rate defined as

$$s = \sqrt{(\partial V_X/\partial X - \partial V_Y/\partial Y)^2 + (\partial V_X/\partial Y + \partial V_Y/\partial X)^2}, \tag{3.16}$$

where $V_X$ and $V_Y$ are the components of the velocity in the global Cartesian coordinates $(X,\ Y)$. These fields demonstrate that the flow mainly consists of multiple long and thin features with relatively high vorticity or strain rate. The values of relative vorticity normalized by the Coriolis parameter (Rossby number) are $O(1)$ which implies significant ageostrophy. The overall filament-like structure of these features and their ageostrophy allow us to relate them to submesoscale motions observed in the ocean. The energy in the laboratory flow is dissipated due to Ekman friction at the bottom as well as due to "regular" viscosity in the

bulk of the fluid. However, the continuous release of baroclinic energy partially compensates dissipation such that the dynamics of the system can be considered quasi-steady for an extended period of time [78]. Time series of the mean azimuthal velocity and the root-mean-square values of both the azimuthal and radial components of velocity in Figure 3.2 show a period of fast adjustment followed by the period of very slow evolution of the flow.

## Energy spectra in the wavenumber space

In order to investigate how anisotropy develops in the flows we consider first the 2D energy spectra in the wavenumber domain. Figure 3.3 shows a sequence of spectra measured in the experiment with salinity of the lower layer, $S = 30$ ppt. The diagrams of the spectral energy $E(k_x,\ k_y)$ obatined by the 2D Fourier transform in the Cartesian coordinates and the spectral energy $E(n, m)$ obtained by the Fourier-Bessel transform in polar coordinates are shown in parallel. Note that the major details of these spectra are qualitatively similar for all of the experiments with different $S$. The spectra in Figure 3.3 allow us to identify the main dynamical features of the flow during its evolution. The spectrum in Figure 3.3(a) is measured right after the pumping of fresh water was stopped. The flow has a significant large scale circulation component which manifests itself as a concentration of energy on $k_y$ axis. Baroclinic instability generates mesoscale motions of $k_x \approx 0.4$ rad/cm and $k_y \approx 0$. The value of $k_x$ is in agreement with the prediction of the Philips model which gives the most unstable wavenumber $k = 0.64 R_{bc}^{-1} \approx 0.5$ rad/cm [88]. Here, the baroclinic radius of deformation is defined as $R_{bc} = (g'H)^{1/2}/f_0$, where $g'$ is the reduced gravity in the two-layer system. Note

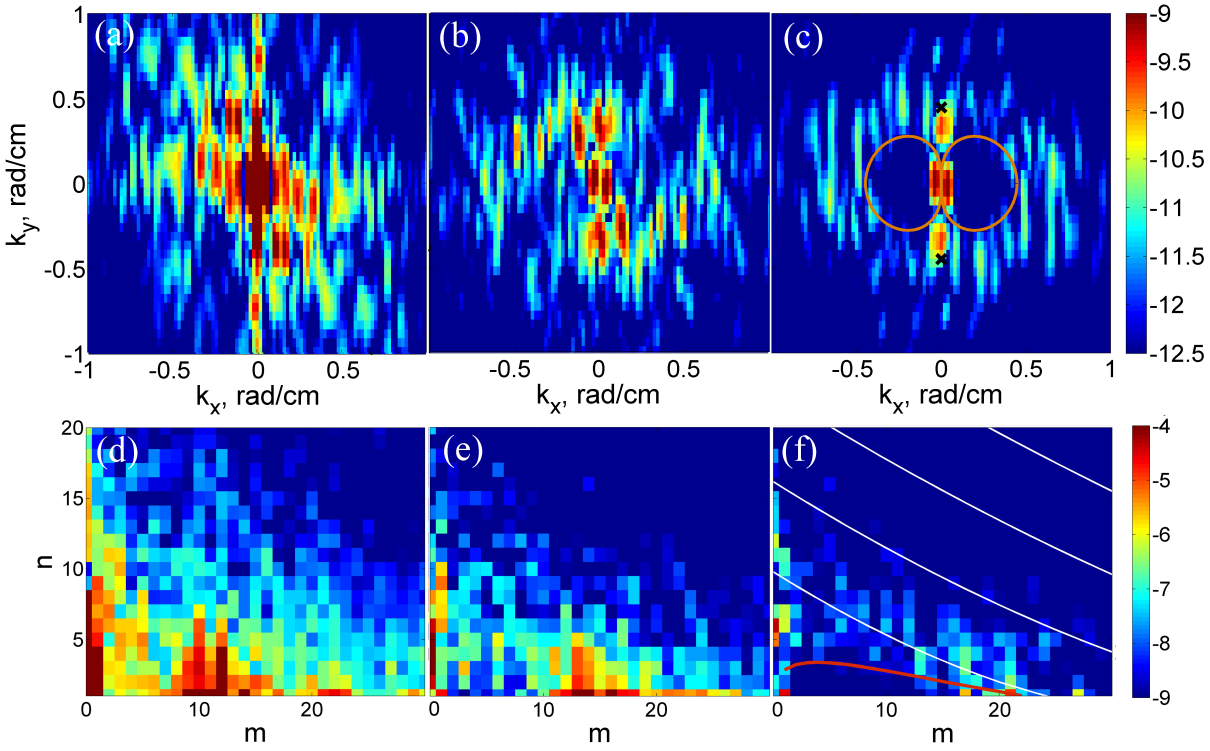


Figure 3.3: Energy spectra in the wavenumber domain: (top row) the Fourier spectra in the Cartesian coordinates and (bottom row) the Fourier-Bessel spectra in the polar coordinates at (a, d) $t = 1$ s, (b, e) $t = 300$ s, and (c, f) $t = 700$ s after switching off the fresh water source. Color scales show energy in logarithmic scale. Red lines in (c) and (f) display Equation (3.17) and Equation (3.19) respectively. Black crosses in (c) mark the Rhines wavenumber while the white lines in (f) are lines of $\alpha_{mn} = 30$, 50, 70, and 90. Lower layer salinity is $S = 30$ ppt.

that after a period of initial linear evolution, baroclinic motions become of finite-amplitude. Their wavenumber in this nonlinearly saturated state is typically smaller than that predicted by linear theory. The fact that $k_y$ is close to zero indicates a significant coherence of the baroclinic perturbations in the radial (y-) direction that was discussed previously in [78]. This can be understood within a theoretical concept of "noodles" [18].

An interesting feature of the spectra in Figure 3.3(a) and (b) is a certain asymmetry

with respect to the vertical axis. There is a somewhat larger concentration of energy in the upper left and the lower right quadrants. This implies that the phase of the periodic pattern in the flow is shifted in the positive x-direction when we move in the negative y-direction (away from the center of the tank). This is due to the larger azimuthal velocity near the wall, especially in the coastal current. The coastal current is the most energetic feature of the flow and its large meanders modulate the flow in the inner region of the tank. Although the area of interest that is used for calculating the spectra excludes the coastal current, its influence is still very significant there. In the experiment with $S = 30$ ppt the current typically had between 12 and 15 meanders. Thus, the same periodicity in the azimuthal direction can be expected in the entire flow. A strong spectral signal should then be expected at wavenumber $k_x$ between 0.25 and 0.3 rad/cm. This coherent pattern is shifted due to the radial dependence of the azimuthal velocity, hence the asymmetry.

When time progresses, the mean circulation subsides, the (finite-amplitude) baroclinic eddies and filaments lose their initial noodle-like coherence in the radial direction and become more isotropic Figure 3.3(b). On the other hand, they emit and interact with the Rossby waves. This process introduces a specific asymmetry into the spectrum. This asymmetry can be described by the so-called figure-of-eight curve [122] given by

$$k = (\beta \cos\phi / V_{rms})^{1/2}, \tag{3.17}$$

where $\phi = \arctan(k_y/k_x)$ is the polar angle in the wavenumber space. Figure 3.3(c) demonstrates a good agreement between the theoretical curve and the experimental energy distribution. Crosses on $k_y$ axis mark the Rhines wavenumber, $k_{Rh} = (\beta/V_{rms})^{1/2}$. Both in panels

(b) and (c), the spectral signiture of zonal jets at $k_y \approx 0.35$ rad/cm is distinct. This value of the wavenumber corresponds to the wavelength, $\lambda_{jet} \approx 18$ cm, such that we observe 4 counterflowing jets.

The 2D Fourier spectra, although useful and informative, have certain limitations. The ring-like area of interest cannot be wide enough to include the pole, otherwise the area distortions occur due to the fact that the scales in the x-direction are y-dependent. The effect of these distortions on the energy spectra is difficult to identify. An alternative approach which is free of these limitations and can be applied in the entire domain, including the pole, is to use the Fourier-Bessel transform. The energy spectra $E(m,\ n)$ in the wavenumber space $(m,\ n)$ are calculated using Equation (3.9) and are shown in the bottom row in Figure 3.3. Here $m$ is the wavenumber in the azimuthal direction while $n$, the number of zeroes of the Bessel function, serves as the wavenumber in the radial direction. Although the main features of the energy distribution in the Fourier-Bessel spectra are similar to those in the 2D Fourier spectra, they can be identified more clearly here. The energy concentration at $m = 12$ and 13 in Figure 3.3(d) and (e) respectively corresponds exactly to the number of meanders of the coastal current. The energy maximum at $m = 0$ and $n = 5$ in Figure 3.3(f) gives the number of alternating zonal jets. Note that the width of the jets is determined by the distance between the consecutive zeroes of the Bessel function $J_0(\alpha_{0n} r/R)$ and is not uniform. A red line in Figure 3.3(f) is a polar-domain analogue of the figure-of-eight curve. It is obtained by equating an eddy "frequency", $V_{rms} k_p = V_{rms} \alpha_{mn}/R$, to the Rossby wave

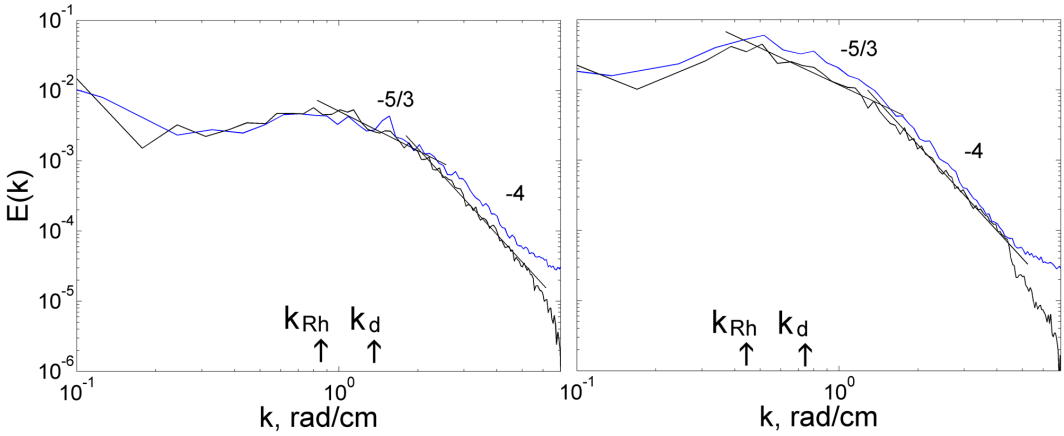


Figure 3.4: 1D energy spectra in the wavenumber domain in the experiments with salinity (left) $S = 12$ ppt and (right) $S = 30$ ppt. Blue and black lines show the Fourier and Fourier-Bessel spectra respectively.

frequency [6]:

$$V_{rms}\alpha_{mn}/R = \frac{2m\gamma}{(\alpha_{mn}/R)^2 + R_d^{-2}}. \tag{3.18}$$

Numerical solution of Equation (3.18) gives the function $n(m)$ which is shown in Figure 3.3 (f). In a similar manner the Rhines wavenumber for the polar domain can be defined:

$$k_{p\ Rh} = (\gamma R/V_{rms})^{1/2}. \tag{3.19}$$

For the flow in Figure 3.3(f), $k_{p\ ,Rh}$=0.15 cm$^{-1}$ which translates into $n$=6. Note that while at smaller $m$ and $n$ the distribution of energy is quite anisotropic, at high values of the wavenumbers, it is less so. In the Fourier-Bessel diagrams the energy is isotropic when it is distributed along the lines of constant $\alpha_{mn}$. White lines in Figure 3.3(f) display $\alpha_{mn} = 30$, 50, 70, and 90; the energy is approximately aligned with the lines for larger $m$ and $n$ just like it aligned with the circles $k$ = constant in 2D Fourier diagrams.

1D energy spectra allow us to look at the energy as a function of isotropic wavenumber $k$.

The spectra are calculated in both Cartesian and polar domains and are shown in Figure 3.4. The spectra calculated by the two different methods are quite close to each other except for very large wavenumbers where the Cartesian-domain spectrum (blue line) becomes more flat. This, however, is likely the artifact due to scale distortion and should be ignored. Figure 3.4 demonstrates spectra for two experiments with different salinity. The values of the baroclinic radius of deformation are different in these experiments and, hence, the values of the corresponding wavenumber, $k_d = R_{bc}^{-1}$ which are indicated by arrows. The values of the Rhines wavenumber are also shown in Figure 3.4. Other than the values of these control parameters, the spectra in these two experiments are quite similar. The source of energy must be close to $k_d$ from where energy propagates to lower wavenumbers where the peak corresponds approximately to $k_{Rh}$. The range of the inverse energy cascade is not very large but the spectral slope of -5/3 can still be identified. At larger wavenumber the energy drops very steeply with a slope of -4.

In order to investigate the periodicity of the flow both in time and space we calculated yet another form of the spectrum, namely the energy spectrum in the frequency-wavenumber domain. The velocity was measured along a circle in the midlatitudes of the tank during a relatively long period of quasi-stationary evolution of the flow. The Fourier transform of the velocity in time and in distance, $x$, along the circle then gives the energy spectrum (Equation (3.13)). The $k-\omega$ spectra allow us to identify Rossby waves in the turbulent flows since the waves obey the dispersion relations while the turbulent motions do not. Rossby waves form the basis of the linear dynamics of the flow, thus, we can see to what extent the

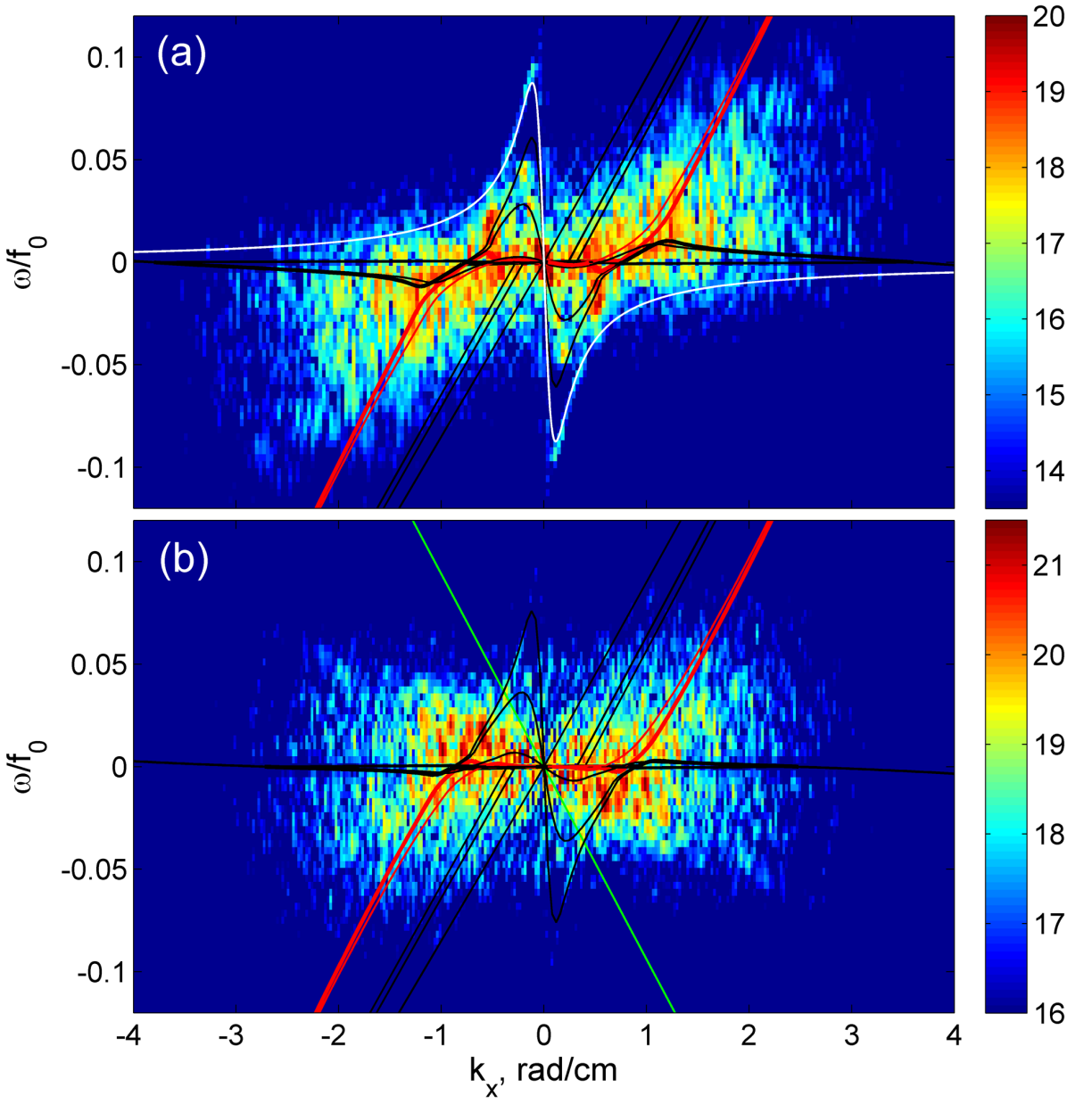


Figure 3.5: Energy spectra in the frequency-wavenumber space measured along the circles of radii (a) $r = 0.5R$ and (b) $r = 0.7R$. White line shows the Rossby wave dispersion relation Equation (3.20) with $k_y = 2\pi/R$ while black and red lines show the damped and growing waves obtained by solving Equation (3.29) with $k_y = (1,\ 2,\ 5) \times 2\pi/R$. Color scales show relative energy (normalized by its spatial average) in logarithmic scale. Lower layer salinity is $S = 10$ ppt.

linear dynamics are significant in the particular flows. Figure 3.5 shows the $k-\omega$ spectra in the experiment with salinity $S = 10$ ppt. Although the main features of spectra in all other experiments were similar, this particular experiment allowed us to observe the waves most clearly. The reason was that at this lowest salinity value, the total energy of the flow was relatively low, hence, the flow was more linear. In addition, the baroclinic radius of deformation was small, $R_{bc} = 0.7$ cm, such that the motions of very small scale were present in the flow.

Figure 3.5(a) and (b) show two spectra measured along the circles of radii $r = 0.5R$ and $0.7R$ respectively. The flow at the inner circle was close to the front of the upper layer which did not extend all the way to the pole in this experiment; the inner flow was relatively weak. The outer circle was, on the other hand closer to a strong coastal current; the flow there was stronger and more nonlinear. The comparison of the two diagrams reveals that waves are more distinct in the inner area of the flow. The waves can be distinguished from eddies using the dispersion relations. The dispersion relation of the Rossby waves in a mean flow can be written in the form:

$$\omega = \mathbf{k} \cdot \mathbf{V}_{mean} - \frac{\beta k_x + R_d^{-2} \mathbf{k} \cdot \mathbf{V}_{mean}}{k^2 + R_d^{-2}}, \tag{3.20}$$

where $\mathbf{V}_{mean}$ is the velocity of the mean flow. In order to identify the Rossby waves in the diagram, we must specify the y-component of the wavenumber. The largest wave in our tank is of one wavelength across the radius of the tank, which corresponds to $k_y = 2\pi/R = 0.11$ rad/cm. White curve in Figure 3.5(a) shows the function $\omega(k_x)$ for this wave without any Doppler shift ($\mathbf{V}_{mean} = 0$). Surprisingly, this curve agrees very well with a

particular pattern in the diagram which demonstrates that this mode is indeed excited in the flow at a range of different frequences. A somewhat more sophisticated analysis can allow us to obtain the dispersion relations not only for the Rossby waves but also for the (growing or damped) baroclinic instability waves in a two-layer flow. Following [14] we can write linearized quasi-geostrophic equations on the $\beta$-plane and, after applying the Fourier transform, obtain the characteristic equation (see Appendix 3.B). Black and red lines in Figure 3.5 display different solutions of the characteristic equation. The black lines show damped Rossby waves (with peaks at $k_x < 0$) and baroclinic instability (almost straight lines at $k_x > 0$) waves. Damping is due to the bottom Ekman friction; the time constant, which gives the rate of the exponential decay of energy, was measured to be $\lambda = 0.002$ s$^{-1}$ in the experiment. In the equations, the mean flow, $V_{x,\ mean} = 0.41$ cm/s, was present in the upper layer only, while the lower layer remained at rest. As a result, the baroclinic instability waves propagate in the positive x-direction. The $\beta$-effect was applied only in the lower layer in order to simulate the topographic $\beta$-effect in the experiments. Thus the Rossby waves, are not Doppler shifted in this theoretical analysis. The red lines in Figure 3.5 display growing modes of the baroclinic instability. It seems that they are in good agreement with the energy plume at $k_x > 0$.

Thus, a good agreement between the theoretical curves showing the linear dispersion relations of the Rossby and baroclinic instability waves, and the measured distribution of energy in the flow indicates that the linear dynamics is a significant in the flow. A line given

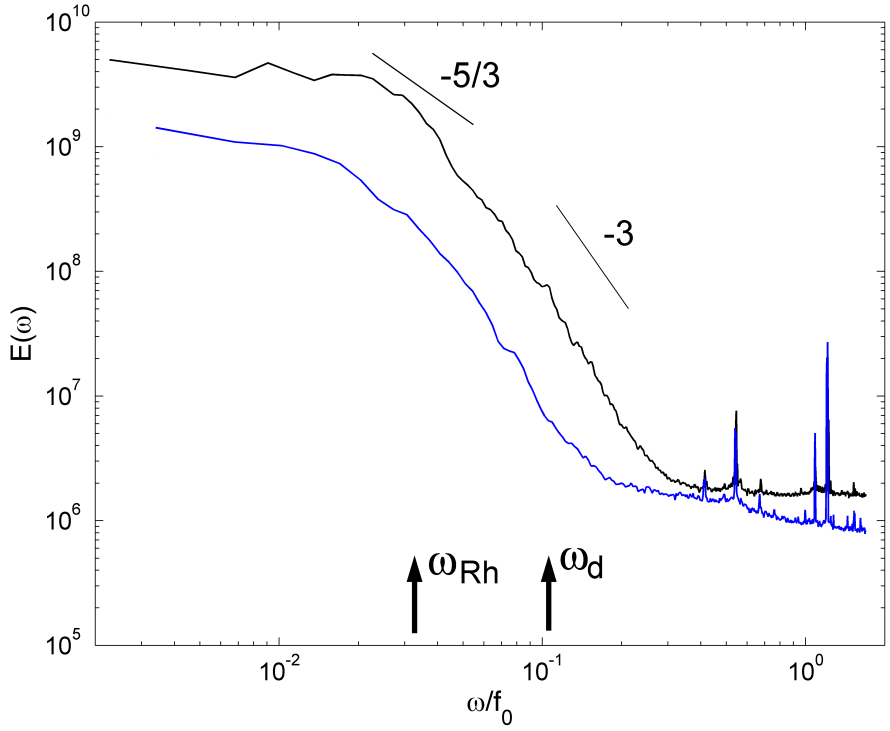


Figure 3.6: 1D spectra of relative energy, normalized by the spatial averaged energy, in the frequency domain in the experiments with salinity (black line) $S = 20$ ppt and (blue line) $S = 10$ ppt.

by

$$\omega = kV_{rms} \tag{3.21}$$

can serve as a simple "dispersion relation" for turbulent motions. It seems that it does indeed provide an upper limit in frequency for the most energetic motions of different wavenumber (green line in Figure 3.5(b)).

1D spectra in the frequency domain can be obtained from $E(\omega,\ k_x)$ by integration over $k_x$ (Figure 3.6). It is interesting to compare the 1D spectra in the frequency and wavenumber domains. Oceanographic measurements from instruments located at a fixed point are in the form of time series which are then interpreted in the frequency domain. However, the theory

of turbulence is mainly developed in the wavenumber domain (see discussion in [43, 10]). For this reason the frequency domain measurements are often related to the wavenumber domain. The only way to do that is to use the Taylor hypothesis. The hypothesis suggests that turbulent motions are embedded in and advected by a mean current such that $\omega = \mathbf{k} \cdot \mathbf{V}_{mean}$. In this case one can expect that the spectra in the frequency domain exhibit the same features as those in the wavenumber domain with the same spectral slopes. In our experiments, however, the Taylor hypothesis is not well justified, if at all. Typically, the rms velocity is larger than the mean current. The spectra in Figure 3.6 measured in two experiments demonstrate that there are some differences between them and the spectra in the wavenumber domain in Figure 3.4. In the frequency spectra the slope is less steep, -3.2 compared to -4 in the wavenumber spectra, and -5/3 slope is hardly present at all. However, there are similarities as well, at least qualitative. We can introduce the Rhines frequency $\omega_{Rh} = (V_{rms}\beta)^{1/2}$ and the forcing frequency $\omega_d = V_{rms}/R_{bc}$ which corresponds to the wavenumbers $k_{Rh}$ and $k_d$. The values of $\omega_{Rh}$ and $\omega_d$ were close in the two experiments and are shown by arrows in Figure 3.6. Thus, the frequency and wavenumber spectra are qualitatively of the same shape in the range between these characteristic quantities. Note that our frequency spectra are very similar to that in the ocean given in [129] with the same flat region at low frequences and relatively steep slope at higher frequences. At very high frequences, the laboratory spectra are relatively flat but have very distinct sharp peaks. One peak is at $\omega/f_0 = 0.5$ which correspond to one rotation of the tank or to one "laboratory day" and is due to some (negligible) tidal motion in the tank. The tidal motion can occur due

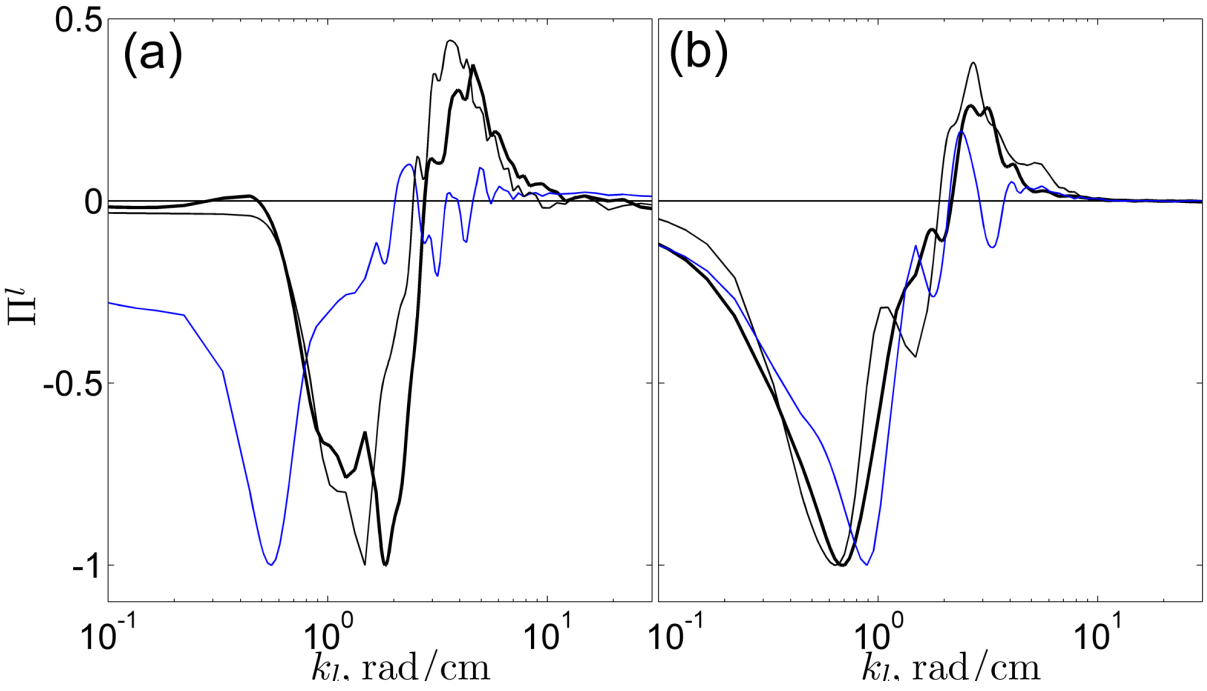


Figure 3.7: Energy flux as a function of the wavenumber in two experiments with salinity (a) $S = 15$ ppt and (b) $S = 30$ ppt. Blue line displays the flux measured in the beginning of the experiments, soon after the injection of the fresh water was stopped, at $t = 10$ s, while the thin and thick black lines show the flux during quasi-steady period of the flow at $t = 270$ s and $t = 430$ s respectively.

to some slight deflection of the rotation axis of the tank from the vertical. The second peak happens at frequencies just above the inertial frequency, $f_0$, and are likely due to (almost inertial) inertia-gravity waves. Note that the emission of the inertia-gravity waves by an almost balanced flow (in the quasi-geotrophic sense) is called spontaneous emission and is an interesting problem by itself, but we do not address it here.

## Energy flux

The form of the 1D spectra (Figure 3.4) resembles that of the spectra in 2D turbulence such that one might expect the existence of the energy cascade. Moreover, we know approximately the location of the energy source given by $k_d$. However, the only way to determine the magitude and the sign of the energy flux across the range of scales is to calculate the flux directly. Figure 3.7 shows the fluxes calculated using Equation (3.14) in two experiments with different salinity. The energy flux is negative at low wavenumbers and becomes positive at higher wavenumbers. The transition is approximately in the range between $k_{Rh}$ and $k_d$ similar to the transition between the slope -5/3 and -4 in 1D energy spectra (Figure 3.4). Thus, the existence of positive $\Pi$ provides an evidence of the direct energy cascade due to relatively high wavenumber (submesoscale) motions. Note that the derivative $\partial\Pi^l/\partial k_l$ is equal to the difference of the energy supply (energy production by the baroclinic instability) and energy disspation (energy sink due to the Ekman and "bulk" viscosity). The positive slope in the range between the negative and positive peaks confirms the presence of the energy source there. At very low or very high $k_l$ the slopes are negative and the dissipation prevails.

In order to calculate fluxes we performed filtering of velocity and its derivatives in the wavenumber domain according to Equation (3.15). The result of the filtering for relative vorticity in the physical space is shown in Figure 3.8. The filtered fields in Figure 3.8(b) and (c) correspond to $k_l$= 1.5 and 3.5 rad/cm respectively and can be compared with the original unfiltered vorticity field in panel a. These particular values of the wavenumber

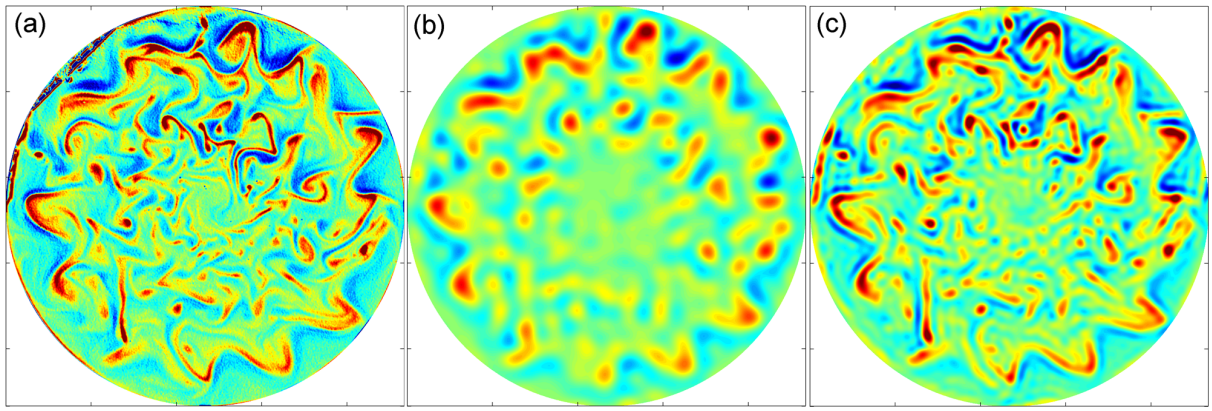


Figure 3.8: Relative vorticity in the experiment with salinity $S = 30$ ppt at $t = 270$ s: (a) original field, (b) filtered at $k_l = 1.5$ rad/cm and (c) filtered at $k_l = 3.5$ rad/cm. Vorticity is normalized by the Coriolis parameter and varies in the range between -0.5 (blue) and +0.5 (red).

$k_l$ correspond to the minimum and maximum value of the energy flux $\Pi$ in Figure 3.7(b). Thus the filtered vorticity fields show the scale of the vortex structures in the flow including eddies, meanders and filaments, at which the inverse or direct energy cascade takes place. Figure 3.9 shows the fields of the energy flux $\Pi^l$ at the same two values of the wavenumber $k_l$ as the vorticity fields. The visual inspection of Figure 3.9 together with Figure 3.8 allows one to relate the pattern of the flux to certain features in the flow. It is not, however, immediately obvious that the overall balance of $\Pi^l$ is negative in Figure 3.9(a) and positive in Figure 3.9(b) since the alternating patterns of $\Pi^l$ are present in both diagrams. For the discussion of the correspondence of the energy flux to certain patterns of vorticity dynamics in 2D turbulence we refer to [131]; some experimental results on rotating shallow-water turbulence are presented in [2].

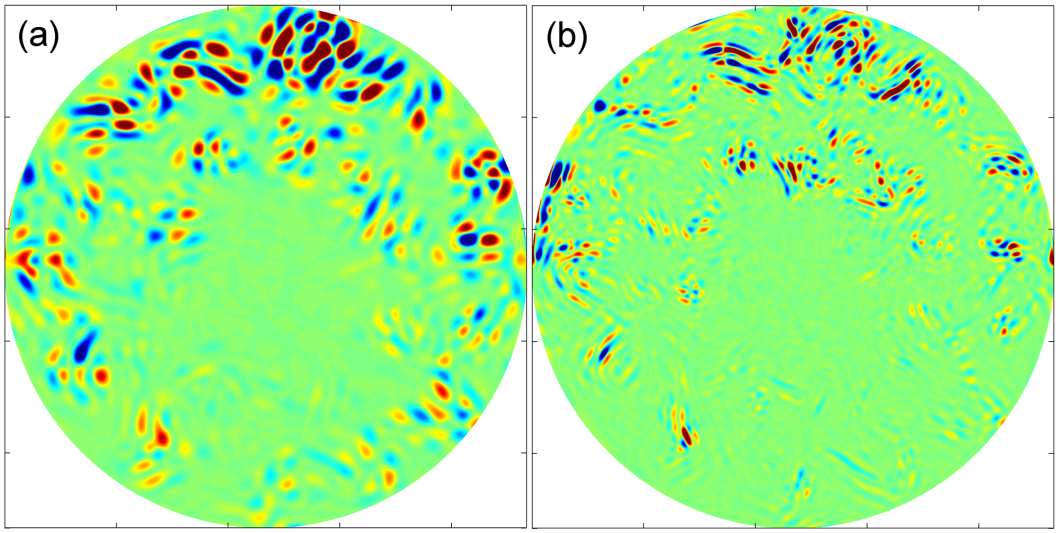


Figure 3.9: Energy flux, $\Pi^l$, in the experiment with salinity $S = 30$ ppt at $t = 270$ s: (a) $k_l = 1.5$ rad/cm and (b) $k_l = 3.5$ rad/cm. Energy flux varies in the range between -0.8 $\text{cm}^2\text{s}^{-3}$ (blue) and +0.8 $\text{cm}^2\text{s}^{-3}$ (red).

## 3.5 Conclusions

The spectral analyses reported in this article investigate the characteristics of the turbulent baroclinic flows on the polar $\beta$-plane. This study was motivated by the oceanographic applications. The laboratory flows are dynamically similar (to the degree the laboratory experiment allows) to oceanic flows where baroclinic instability is important. We investigated the entire range of scales/wavenumbers and times/frequences where the main dynamical processes take place. These include the Rossby waves, the alternating zonal jets, baroclinic instability waves which are of large scale to mesoscale, and eddies and filaments which are in the range from meso- to submesoscale.

2D energy spectra in wavenumber domain demonstrate the evolution from radial coherence and well-defined azimuthal wavenumber of the initial energy concentration due to

noodle-like baroclinic purturbations towards a different asymmetry in the energy distribution. This later state is predicted in [98] such that the energy concentrates along the figure-of-eight curves as well as in "hot spots" corresponding to alternating zonal jets. The Fourier-Bessel decomposition proved to be a useful tool in application to a circular domain such as our experimental tank. It allowed us to see somewhat "sharper" spectra than those obtained by the Fourier decomposition and to distiguish radial and azimuthal effects more clearly. We showed that all general theoretical concepts such as the figure-of-eight curves or the Rhines wavenumber can be easily transferred into the polar $\beta$-plane.

2D energy spectra in the frequency-wavenumber domain are asymmetric. At negative zonal wavenumbers, $k_x$, the motions that propagate to the east (sometimes against the mean flow) are located. The Rossby waves signature is prominent as revealed by their dispersion relation. This provides evidence that linear dynamics is significant in our flows in spite of the fact that nonlinearity is present as well (the Rossby number is $\mathcal{O}(1)$). The nonlinear motions seem to be concentrated under the dividing line $\omega = V_{rms}k$ in the spectra. At positive $k_x$, the growing (and decaying) baroclinic instability waves are present as shown by the stability analysis similar to that in [14]. It is interesting to compare the laboratory spectra to those in the midlatitude Pacific Ocean reported in [129]. There are clear similarities between the laboratory and the oceanic spectra but, perhaps, the main difference is the presence of the so-called "non-dispersive" line in the oceanic ones. The line is given by $\omega = \beta R_{bc}^2 k$, where $R_{bc}$ is the first baroclinic radius of deformation. The slope of the line corresponds to the phase velocity of long baroclinic Rossby waves. However, in the laboratory, the Rossby waves

are barotropic due to the nature of the topographic $\beta$-plane. Thus, we did not observe the concentration of energy with this slope, instead, shorter waves with wavenumbers close to that of (baroclinic) forcing were more prominent than long non-dispersive waves. A similar observation was reported in our previous study on forced barotropic turbulence [134].

Our 1D energy spectra in the frequency domain are remarkably similar to that in the ocean [129] apart from the peak at the annual cycle which we don't have in the laboratory experiments. Characteristic frequencies $\omega_{Rh}$ and $\omega_d$ can be easily estimated for the area in the Pacific ocean used by Wunsch [130] to compute the spectrum. Taking the rms velocity $V_{rms} = 10 \sim 20$ cm/s and the first baroclinic radius of deformation $R_{bc} = 40$ - 50 km, we obtain $\omega_{Rh} \approx 0.02$ cycles/day and $\omega_d \approx 0.04$ cycles/day. These values can be placed in the ocean spectrum similar to those in the laboratory spectrum.

The analysis of the spectral energy flux provided the evidence of the direct energy cascade to smaller scales by relatively small-scale motions which can be related to the oceanic submesoscale. An inverse energy cascade at larger scales was also observed as was expected according to the 2D turbulence theory and our previous study [134].

The present investigation was limited to spectral properties of the flows, however, many interesting questions related to the dynamics of the submesoscale motions remain. They include cyclone-anticyclone asymmetry, formation and sharpening of elongated filaments and buoyancy fronts. Further investigation using the laboratory data is certainly warranted.

# Appendix

## 3.A Parseval's identity

Parseval's identity shows that the total energy in physical space is equal to the total energy in the spectral domain. Here we show the Parseval's identity for the Fourier-Bessel series. In radial direction, Bessel function of the first kind is used as the basis function such that

$$\int_0^R \mathbf{u}(m,r)\mathbf{u}^*(m,r)rdr = \int_0^R \{\sum_n \mathbf{B}_{mn} J_m(\frac{r}{R}\alpha_{mn})\}\times \{\sum_n \mathbf{B}^*_{mn} J_m(\frac{r}{R}\alpha_{mn})\}\ rdr, \tag{3.22}$$

where the asterisk denotes the complex conjugate. Using the orthogonality condition

$$\int_0^R J_m(\frac{r}{R}\alpha_{mp}) J_m(\frac{r}{R}\alpha_{mq})rdr = \frac{1}{2}R^2\delta_{pq}J^2_{m+1}(\alpha_{mn}), \tag{3.23}$$

where $\delta_{pq}$ is the Kroneker delta, Equation (3.22) can be simplified as follows:

$$\int_0^R \mathbf{u}(m,r)\mathbf{u}^*(m,r)rdr = \frac{R^2}{2}\sum_n \mathbf{B}_{mn}\mathbf{B}^*_{mn}J^2_{m+1}(\alpha_{mn}). \tag{3.24}$$

In the azimuthal direction, Parseval's identity for Fourier series gives

$$\sum_m \mathbf{u}(m,r)\mathbf{u}^*(m,r) = \frac{1}{2\pi}\int_0^{2\pi} |\mathbf{u}(\theta,r)|^2 d\theta. \tag{3.25}$$

Summing Equation (3.24) over all zonal modes $m$ and using Equation (3.25), we obtain the Parseval's identity for the Fourier-Bessel series in the from:

$$\frac{1}{\pi R^2}\int_0^{2\pi}\int_0^R |\mathbf{u}(\theta,r)|^2 r dr d\theta = \sum_{m,n} \mathbf{B}_{mn}\mathbf{B}^*_{mn} J^2_{m+1}(\alpha_{mn}). \tag{3.26}$$

The LHS of Equation (3.26) represents a spatial average of kinetic energy while the RHS represents a total energy of different modes in the spectral domain.

## 3.B Dispersion relation for two-layer baroclinic flow

Following [14] we write the linearized equations of motions for the two-layer flow in the following form:

$$\begin{aligned}\frac{\partial}{\partial t}(\nabla^2\psi_1 - S_1\psi_1 + S_1\psi_2) = &- U_1\frac{\partial}{\partial x}\nabla^2\psi_1 - U_1 S_1\frac{\partial\psi_2}{\partial x} \\ &+ U_2 S_1\frac{\partial\psi_1}{\partial x} + \nu\nabla^4\psi_1,\end{aligned} \tag{3.27}$$

$$\begin{aligned}\frac{\partial}{\partial t}(\nabla^2\psi_2 + S_2\psi_1 - S_2\psi_2) = &- U_2\frac{\partial}{\partial x}\nabla^2\psi_2 - U_2 S_2\frac{\partial\psi_1}{\partial x} \\ &+ U_1 S_2\frac{\partial\psi_2}{\partial x} + \nu\nabla^4\psi_2 \\ &- \beta_T\frac{\partial\psi_2}{\partial x} - \lambda\nabla^2\psi_2,\end{aligned} \tag{3.28}$$

where index $i = 1$ or 2 refers to the upper or lower layer respectively, $\psi_i$ is the stream functions, $U_i$ is the mean flow, $H_i$ is the mean depth of each layer, $S_i = f_0^2/g'H_i$ and $g'$ is the reduced gravity. $\nu = 0.01\ cm^2/s$ is the kinematic viscosity and $\lambda = 0.002\ s^{-1}$ represents the bottom Ekman friction, estimated by approximating the time series of the kinetic energy in the experiment using exponential function $e^{-\lambda t}$. Here we take $U_2 = 0$ in the bottom layer

and the measured values of $U_1$ in the upper layer; the $\beta$-effect is present in the lower layer only. Solving the above equations in the Fourier space gives the characteristic equation

$$a\omega^2 + b\omega + c = 0, \tag{3.29}$$

where

$$a = [(\kappa + S_1)(\kappa + S_2) - S_1 S_2], \tag{3.30a}$$

$$\begin{aligned} b = {} & k_x[\beta_T(\kappa + S_1) - \kappa^2(U_1 + U_2) - 2\kappa(S_2 U_1 + S_1 U_2)] + \\ & ik_x[\nu\kappa(2\kappa + S_1 + S_2) + \lambda(\kappa + S_1)], \end{aligned} \tag{3.30b}$$

$$\begin{aligned} c = {} & [k_x(-S_1 U_2 - \kappa U_1) + i\lambda\kappa^2] \cdot [k_x(\beta_T - S_2 U_1 - \kappa U_2) + \\ & i\nu\kappa^2 + i\lambda\kappa] - k_x^2 S_1 S_2 U_1 U_2, \end{aligned} \tag{3.30c}$$

$$\kappa = k_x^2 + k_y^2. \tag{3.30d}$$

The solutions of Equation (3.29) give complex frequency $\omega(k_x, k_y) = \omega_r + i\omega_i$. Positive $\omega_i$ represents growing waves while negative $\omega_i$ means damped waves.

# Chapter 4

# Rossby Wave Radiation by an Eddy on a *beta*-plane

This chapter is an adapted version of a journal article published in Physics of Fluids (Zhang and Afanasyev 2015).

## 4.1 Introduction

Meso-scale vortices (eddies) are an essential element of the dynamics of the turbulent oceans. They provide the strongest signal in the snapshots of the circulation measured by the satellite altimetry. Eddies are intimately linked to narrow zonal flows (jets) observed in midlatitudes [80, 81]. The altimetric signal due to zonal jets is much more subtle than that of eddies. For this reason, the jets are called 'latent' in the oceans. Although it is known that the existence

of the zonal jets is due to the $\beta$-effect, the details of their generation are still a subject of ongoing discussion. One of the mechanisms discussed is related to the radiation of Rossby waves by eddies. The radiation of Rossby waves results in the creation of gyres ($\beta$-plumes) elongated in the zonal direction. Each $\beta$-plume consists of two jets flowing in the opposite directions [116, 38, 4]. $\beta$-plumes can be described within the framework of linear dynamics. This implies that linear modes can provide a significant control of the entire flow which include eddies, jets, and Rossby waves. A more general question is then to what extent the linear dynamics is important. In their recent numerical and theoretical studies, Ref. [14] analyzed linear modes in the idealized ocean circulation containing multiple jets and eddies and showed that certain properties of (generally nonlinear) eddies can be understood in terms of the linear modes. The linear modes themselves can be modified by the background flow. An analysis of an ocean gyre circulation in a spectral space performed recently [32] showed that the zonal jets (also called striations) can be interpreted either within linear dynamics context as almost zero-frequency Rossby waves or as a result of the nonlinear eddy propagation.

The present study is motivated by the oceanographic phenomena mentioned above. In what follows, we consider an idealized setup where Rossby waves are radiated by single vortex propagating on the topographic polar $\beta$-plane in the rotating tank. We focus on the far-field, away from the immediate vicinity of the vortex, where the properties of the flow were not measured in detail in previous experimental studies. In particular, we identify the horizontal wave patterns and measure the spectral characteristics of the flow. We supple-

ment our laboratory experiments with numerical simulations and theory. The results of the experiments are used as a benchmark to compare with the analytical results and the results of the simulations. The comparison between linear theory and nonlinear simulations or experiment allows us to determine to what extent the linear dynamics can predict the pattern of waves in a generally nonlinear flow.

Although a number of theoretical and numerical studies addressed the radiation of Rossby waves by vortices, laboratory investigations are relatively few. This is perhaps due to the fact that it is difficult to observe the wave field using traditional laboratory techniques. Visualization with dye allows one to record the vortex trajectory and observe its evolution but gives little information about the wave field. The Particle Image Velocimetry (PIV) technique is a well-known experimental tool and can be used to measure velocity within the vortex and in its vicinity. It is, however, more challenging to measure the far-field velocity in a large tank. Most of the laboratory studies were focused on investigating the dynamics of the vortex motion on the $\beta$-plane (e.g.,[50, 123, 115, 104, 47]). Ref. [47] used PIV to measure the velocity profiles in monopolar cyclonic vortices created by suction or stirring. They also studied the trajectories of the vortices and compared the measured trajectories with those predicted by a theoretical mechanistic model based on integral relations for the Rossby force and a lift force. In this study, we use a recently developed experimental technique, Altimetric Imaging Velocimetry (AIV) to overcome the shortcomings of the earlier techniques and to observe and measure the flow field both within the vortex and in the entire tank with the same spatial and temporal resolution. The AIV technique measures the gradient of the

surface elevation field. Integration of the gradient in the horizontal plane allows one to obtain the surface elevation field which can also be interpreted as the pressure field at the surface. The surface elevation is one of the major dynamic fields that can be used to describe the Rossby waves. The measured gradient can be further used to obtain the velocity field in the flow using quasi-geostrophic (QG) equations.

Radiation of Rossby waves by stationary perturbations was discussed in application to different oceanographic problems including the flows induced by localized buoyancy sources [116, 64, 38, 58]. A similar solution for an atmospheric tropical cyclone was given by [28]. A linear radiation process is easy to understand. When a localized perturbation is steady, i.e there is no oscillation inside the perturbation area such that the perturbation area acts as a rigid body travelling through the flow, long Rossby waves with frequency approaching zero have nearly zonal wavecrests. As a result of the radiation, the perturbation stretches to the west forming a ridge/trough. According to geostrophy, two zonal jets form along the slopes of the ridge/rough. The formation of the $\beta$-plume circulation due to the source of buoyant fluid was illustrated in the laboratory experiments on the polar (quadratic) $\beta$-plane by [4].

Vortices in a turbulent flow are not at rest; they propagate due to interaction with other vortices or with the background flow. Single vortices on the $\beta$-plane propagate due to nonlinear effect of the induced wave field on the vortex. Cyclonic vortices travel to the northwest, while anticyclonic vortices travel to southwest while radiating the Rossby waves. Thus, it is important to include the source motion into the radiation problem. Lighthill[70] gave a general solution of the linear problem for a travelling transient forcing. The external

forcing can be due to a wind-stress curl present in a finite region of space, travelling with constant velocity and varying in magnitude over some time period. A particular case is a steady forcing for which the forcing frequency is zero. Lighthill's solution gives the frequency of the Rossby waves as a function of wavenumber in $x$- and $y$- directions. In the case of the steady forcing, the solution predicts the relation between the $x$- and $y$- wavenumbers (a curve in wavenumber space) for any particular velocity of the forcing.

In Section 4.2 of this paper, we describe the setup of the laboratory apparatus as well as the altimetry technique. In Section 4.3, the setup of the shallow water numerical model is described. A theory of the Rossby wave radiation by a travelling vortex is presented in Section 4.4. In Section 4.5, the results of the laboratory experiments, numerical simulations, and theory are reported. Concluding remarks are given in Section 4.6.

## 4.2 Laboratory setup and techniques

In our laboratory experiments, a cylindrical tank of radius $R = 55$ cm was filled with water of depth $H_0 = 10$ cm (Figure 4.1). The tank was installed on a rotating table and was rotated anticlockwise at a constant angular rate $\Omega = 2.4$ rad/s. The vortices in the tank were generated by suction of fluid from below the surface. A thin tube connected to a pump was placed on the bottom of the tank such that the opening of the tube was directed upward (Figure 4.1). The suction creates a localized sink which manifests itself as a depression on the surface. Water converging to the sink creates a cyclonic vortex in the presence of the

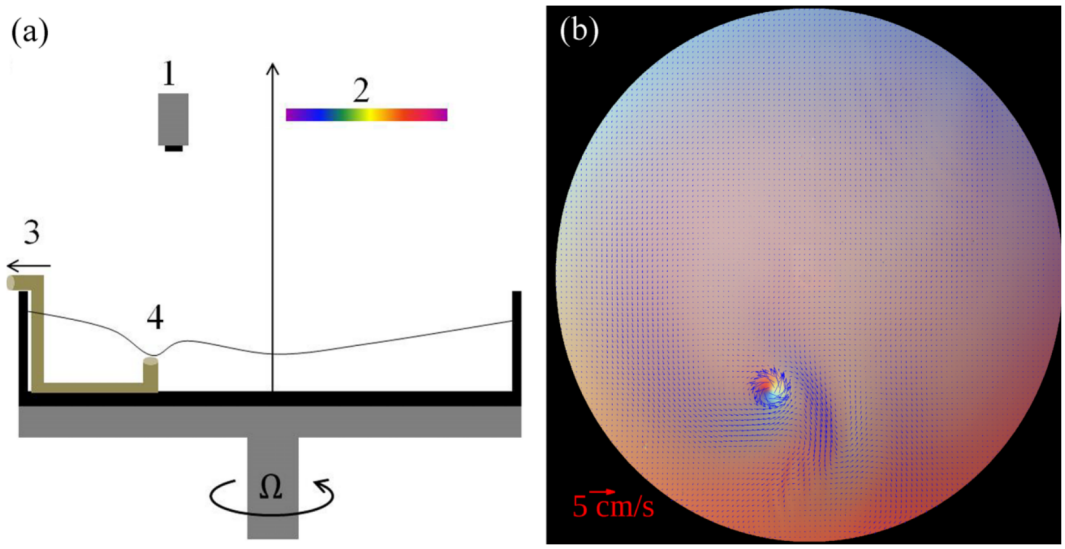


Figure 4.1: (a) Sketch of the experimental setup (left): digital camera (1), high brightness display showing the color mask (2), the fluid in the tank is pumped out through a thin tube (3) to generate a cyclonic vortex (4). (b) Top view of the flow with a superposed velocity field (vectors) measured by the AIV at 19 s in experiment 1.

background rotation. The vorticity in the core of the vortex is created by stretching the background vorticity. Both the suction rate (determined by the voltage, $V$, applied to the pump) and the duration of suction, $\Delta t$, were varied in the experiments such that vortices of different strengths and sizes were created. The control parameters for five experiments are given in Table 4.1. Table 4.1 also summarizes the main characteristics of the vortices measured right after the forcing period. The characteristics include the surface elevation, $\eta$, in the center of each vortex, the maximum azimuthal velocity averaged around the vortex, $V_{\theta v}$, the vortex radius $R_v$, which is defined as the radial location of $V_{\theta v}$, the total kinetic energy, $K$, the mean Rossby number, $Ro_v = V_{\theta v}/(f_0 R_v)$, and the ratio of the vortex azimuthal velocity to its translational velocity, $A = V_{\theta v}/U_t$. Here, $f_0 = 2\Omega$ is the Coriolis parameter.

The surface of water in the tank when in a state of a solid-body rotation is a paraboloid, such that the depth of water is given by

$$h(r) = H_0 + \frac{\Omega^2}{2g}(r^2 - \frac{R^2}{2}), \tag{4.1}$$

where $r$ is the distance to the axis of rotation (center of the tank) and g is the gravitational acceleration. A dynamical effect of the radial variation of depth is similar to that due to a variation of the Coriolis parameter on a rotating planet. The dynamical equivalence of these effects follows from the conservation of potential vorticity (PV). The center of the tank corresponds to the North pole of the planet. Due to the quadratic variation of the depth of the layer, the laboratory system corresponds to a so-called polar $\beta$-plane (or $\gamma$-plane) such that the Coriolis parameter is $f = f_0 - \gamma r^2$, where $f_0 = 2\Omega$ and $\gamma = \Omega^3/gH_0$ [5]. In this study, however, we also use a regular $\beta$-plane approximation for comparison with numerical simulations and theory. The $\beta$-plane where the Coriolis parameter varies linearly in the South-North direction can be defined with respect to a referencedistance from the North pole $r_0$. A local Cartesian coordinate is introduced at this reference latitude such that the x and y axes are directed to the east and the north, respectively. The $\beta$-parameter is then defined as

$$\beta = \frac{2r_0\Omega^3}{gh(r_0)}. \tag{4.2}$$

In the experiments, the vortices were created at $r_0 = 30\ cm$, where $\beta = 0.1\ cm^1 s^{-2}$.

Altimetry method [8] was used to measure two components of the gradient $\nabla\eta = (\eta_x, \eta_y)$ of the perturbation surface elevation $\eta$ in the horizontal plane $(x, y)$. The $\nabla\eta$ field was measured with a spatial resolution of approximately 2 vectors per millimeter which translates

into the array of size $2300 \times 2300$, with a temporal resolution of 5 fields per second. The surface velocity of the flow is then determined using quasi-geostrophic approximation

$$\mathbf{V} = \frac{g}{f_0}\mathbf{n} \times \nabla\eta - \frac{g}{f_0^2}\frac{\partial}{\partial t}\nabla\eta - \frac{g^2}{f_0^3}J(\eta, \nabla\eta), \tag{4.3}$$

where $\mathbf{V}$ is the horizontal velocity vector, $\mathbf{n}$ is the vertical unit vector. Note that while we measure an exact (within experimental accuracy) pressure gradient, $\nabla p = \rho g \nabla\eta$, at the surface, the velocity field is determined more accurately when the flow is closer to being quasigeostrophic. According to the Taylor-Proudman theorem, in a rapidly rotating flow, the surface velocity is a good approximation for the velocity in the entire column of water except the Ekman layer at the bottom. Table 4.1 shows that the Rossby number, $Ro_v = 2V_{\theta v}/(f_0 R_v)$, that characterizes the relative vorticity in the core of the vortex exceeds unity in experiments $1 \sim 4$ (immediately after the forcing stops). Here, $V_{\theta v}$ is the maximum azimuthal velocity of the vortex and $R_v$ is the radial location of $V_{\theta v}$ from the vortex center. In these experiments where $Ro_v > 1$, the validity of the quasi-geostrophic approximation was not satisfied within the vortex cores in the initial period of their evolution. As a consequence, the velocity within the cores calculated with Equation (4.3) differed from the real velocity. Later in these experiments as flow decayed, the values of the Rossby number dropped below unity. In experiment 5, the validity of the quasi-geostrophic approximation was satisfied at all times. The flow beyond the cores of the vortices (which is the primary focus of this study) was always well within the bounds of the approximation in all experiments such that the velocity given by the AIV was accurate.

| Parameters | Exp.1 | Exp.2 | Exp.3 | Exp.4 | Exp.5 |
|---|---|---|---|---|---|
| $\Delta t$ (s) | 7.7 | 2.6 | 3.2 | 8.4 | 7.1 |
| V (Volt) | 7.9 | 7.9 | 6.9 | 6.0 | 9.0 |
| $\eta_v$ (cm) | -0.19 | -0.16 | -0.14 | -0.19 | -0.2 |
| $R_v$ (cm) | 1.7 | 0.9 | 0.91 | 1.1 | 2.7 |
| $V_{\theta v}$ (cm/s) | 5.8 | 5.8 | 5.7 | 6.2 | 4.4 |
| $K$ (cm$^4$/s$^2$) | 7 | 2.7 | 2.3 | 6.0 | 8.2 |
| $Ro_v = 2V_{\theta v}/(f_0 Ro_v)$ | 1.4 | 2.6 | 2.6 | 2.3 | 0.67 |
| $A = V_{\theta v}/U_t$ | 6.1 | 9.7 | 11 | 7.8 | 3.8 |

Table 4.1: Experiment parameters.

## 4.3 The numerical model

We consider vortices on the $\beta$-plane in a shallow water model,

$$(\frac{\partial^2}{\partial t^2} - k_d^{-2})\psi = -\beta\psi_x - J(\psi, \nabla^2\psi) - \nu\nabla^6\psi - \lambda\nabla^2\psi, \tag{4.4}$$

where $\psi$ is the stream function and $k_d = f_0/\sqrt{gH_0} = 0.05\ cm^{-1}$ is the reciprocal of the deformation radius. The biharmonic diffusion term $\nu\nabla^6\psi$ is routinely used in the simulations of two-dimensional turbulence in order to effectively remove motions at the smallest scales [24, 72]. The term $\lambda\nabla^2\psi$ represents the linear Ekman bottom friction. A particular value of the friction coefficient, $\lambda = 0.03\ s^{-1}$ , was chosen to model the flow decay in our laboratory experiments. The spatial differencing was implemented using the pseudo-spectral method based on the Fourier series, implying the periodic boundary condition in both directions. For the sake of numerical efficiency and stability, we used semi-implicit scheme AB3CN from [23]. It combines third-order Adams-Bashforth scheme and the second-order Crank-Nicholson scheme to discretize linear part including the $\beta$ term and the damping terms in time. The numerical domain was set to be a square of 110 cm wide with 512 grid points

along each side. The value of the $\beta$ parameter, $\beta = 0.1$ cm$^{-1}$s$^{-1}$ , in the simulations was the same as that in the experiments. The simulations were performed in a rectangular (double periodic) domain on a regular $\beta$-plane, rather than in a circular geometry and a polar $\beta$-plane (as in our experiments) for the purpose of easier comparison and interpretation of the results since in the majority of previous theoretical or numerical studies, a regular $\beta$-plane was used.

## 4.4 Theory

Suppose we have a turbulent flow on an $f$-plane [2]. Energy distribution between motions of different spatial scales is established by nonlinear (triad) interactions. The energy spectrum is isotropic in wavenumber space. The flow on the f-plane is similar to a purely two dimensional turbulent flow in non-rotating fluid except perhaps for the presence of the Ekman layer at the bottom. Let us now suddenly switch on the $\beta$-effect. While the flow still remains balanced on small scales where nonlinear terms prevail over the $\beta$-effect, it will be unbalanced on larger scales where a QG type balance is required. In what follows, we look for an additional component of the flow that is required to balance the initially specified turbulent flow. We consider the scales starting from the scale where the turbulent flow starts to feel the $\beta$-effect (the Rhines scale) which corresponds to the scale of the largest vortices/eddies formed in the turbulent cascade, and larger zonal structures are formed in physical space to satisfy the quasi-geostrophic type balance. Meanwhile, in spectral space, the energy distribution

becomes anisotropic because energy can now cascade directly to the zonal modes such that the additional component of the flow will be in the form of Rossby waves. At large scales, it is sufficient to consider a linear dynamics at least as first approximation. The turbulent vortices (assumed known) constitute a forcing in the wave equation. In what follows, for simplicity, we consider only one vortex.

Let us follow a well-known derivation of a QG equation in order to obtain the forcing terms. Consider a flow on a $\beta$-plane $(x, y)$ where the Coriolis parameter varies linearly in y-direction as

$$f = f_0 + \beta y. \tag{4.5}$$

The flow consists of an assumed known eddy component with velocity $\mathbf{U} = (U_x, U_y)$ and the additional component due to the $\beta$-effect (the Rossby wave component) with velocity $\mathbf{u} = (u_x, u_y)$. Both components can be related to pressure fields, expressed in terms of surface elevations $\eta_0$ and $\eta$, respectively, via geostrophic relations,

$$\mathbf{U} = \frac{g}{f_0}\mathbf{n} \times \nabla\eta_0, \quad \mathbf{u} = \frac{g}{f_0}\mathbf{n} \times \nabla\eta, \tag{4.6}$$

where $\mathbf{n}$ is the vertical unit vector and $g$ is the acceleration due to gravity. Potential vorticity of the flow can be defined in a usual manner

$$q = \frac{f + \zeta_0 + \zeta}{h}, \tag{4.7}$$

where relative vorticities are $\zeta_0 = g\nabla^2\eta_0/f_0$ and $\zeta = g\nabla^2\eta/f_0$. The fluid depth is given by

$$h = H - h_b + \eta_0 + \eta, \tag{4.8}$$

where $H$ is the mean depth and $h_b$ is the bottom height. Assuming that $h_b$, $\eta_0$, and $\eta$ are small compared to $H$ and $\zeta_0$ and $\zeta$ are small compared to $f_0$ , we rewrite $q$ in the form

$$q = \zeta_0 + \zeta + \beta y - \frac{f_0}{H}(\eta + \eta_0 - h_b). \tag{4.9}$$

The dynamics of the flow is governed by the conservation equation for the potential vorticity,

$$[\frac{\partial}{\partial t} + (\mathbf{U} + \mathbf{u}) \cdot \nabla]q = 0, \tag{4.10}$$

which, after some algebra, can be rewritten in the form

$$\frac{\partial}{\partial t}(\nabla^2 - k_d^2)(\eta_0 + \eta) + (\mathbf{U} + \mathbf{u}) \cdot \nabla(\nabla^2\eta_0 + \nabla^2\eta) + k_d^2(\mathbf{U} + \mathbf{u}) \cdot \nabla h_b + \beta\frac{\partial}{\partial x}(\eta + \eta_0) = 0, \tag{4.11}$$

where $k_d$ is the reciprocal of the radius of deformation, $k_d = R_d^{-1} = f_0/\sqrt{gH}$. To derive Equation (4.11), we used the identity $(\mathbf{U} + \mathbf{u}) \cdot \nabla(\eta_0 + \eta) = 0$ which results from geostrophic relations Equation (4.6). In our further analysis, we consider a domain with a flat bottom such that the term containing $\nabla h_b$ is equal to zero. Note that this term gives a vertical velocity due to the flow over topography which can result in interesting effects in a class of problems where the bottom topography is important [113, 114]. We can neglect the quadratic term $(\mathbf{u} \cdot \nabla)\nabla^2\eta$ in Equation (4.11) assuming that the wave field is relatively weak. The term $(\mathbf{U} \cdot \nabla)\nabla^2\eta_0$ describes the advection of the relative vorticity of a vortex by its velocity field. It can be shown that this term vanishes if we assume that the vortex is axisymmetric. Indeed, in that case, the advection is just a rotation of a vorticity distribution given by $\nabla^2\eta_0$ around the center of the vortex. The translation of a vortex is determined by the wave velocity which is significant inside the vortex. Note that the vortex velocity field generates large

difference in the Coriolis force between the northern and southern parts of the eddy. The mean Coriolis force drives the (cyclonic) vortex to the North. The advection of the vortex can be approximated by a constant translation velocity $\mathbf{U_t}$ such that $(\mathbf{u}\cdot\nabla)\nabla^2\eta_0 \approx (\mathbf{U_t}\cdot\nabla)\nabla^2\eta_0$. Outside the vortex, the term $(\mathbf{u}\cdot\nabla)\nabla^2\eta_0$ is negligible since both $\mathbf{u}$ and $\eta_0$ are relatively weak. The linearized Equation (4.11) becomes

$$\frac{\partial}{\partial t}(\nabla^2 - k_d^2)\eta + \beta\frac{\partial \eta}{\partial x} = -\frac{\partial}{\partial t}(\nabla^2 - k_d^2)\eta_0 - \beta\frac{\partial \eta_0}{\partial x} - (\mathbf{U_t}\cdot\nabla)\nabla^2\eta_0. \tag{4.12}$$

In the rotating systems, Ekman dissipation can be important. This effect can be easily included in a form of the Ekman pumping. Vertical velocity at the boundary of the bottom Ekman layer is proportional to the absolute vorticity of the flow

$$w_E = \frac{\delta_E}{2}(\zeta_0 + \zeta), \tag{4.13}$$

where $\delta_E = \sqrt{2\nu/f_0}$ is the thickness of the Ekman layer and $\nu$ is the kinematic viscosity of fluid. Introducing the Ekman number, $E = 2\nu/(f_0 H^2)$, we obtain

$$w_E = \frac{1}{2}E^{1/2}k_d^{-2}f_0\nabla^2(\eta_0 + \eta). \tag{4.14}$$

The part of $w_E$ which is due to the relative vorticity of the vortex will serve as an additional forcing term in Equation (4.12), while the part due the relative vorticity of the wave will act as a damping term. With these additional Ekman terms, Equation (4.12) becomes

$$\frac{\partial}{\partial t}(\nabla^2 - k_d^2)\eta + \beta\frac{\partial \eta}{\partial x} + \lambda\nabla^2\eta = -\frac{\partial}{\partial t}(\nabla^2 - k_d^2)\eta_0 - \beta\frac{\partial \eta_0}{\partial x} - (\mathbf{U_t}\cdot\nabla)\nabla^2\eta_0 - \lambda\nabla^2\eta_0, \tag{4.15}$$

where $\lambda = E^{1/2}f_0/2$ is the Ekman coefficient.

Assuming that the RHS of Equation (4.15) is known, we transform the equation into Fourier space,

$$\frac{\partial \tilde{\eta}}{\partial t} + (i\omega + \omega_E)\tilde{\eta} = -\frac{\tilde{F}}{k^2 + k_d^2}. \tag{4.16}$$

Here,

$$\omega = \frac{-k_x \beta}{k^2 + k_d^2} \quad and \quad \omega_E = \frac{\lambda k^2}{k^2 + k_d^2} \tag{4.17}$$

are the Rossby wave frequency and the Ekman frequency, respectively, $\tilde{F}$ is the Fourier transform of the RHS of Equation (4.15), $k = (k_x, k_y)$ is the wavevector, and the tilde denotes the spatial Fourier transform. Solving the first-order differential Equation (4.16) with an initial condition $\tilde{\eta}(t = 0) = 0$, we obtain

$$\tilde{\eta} = \exp(-i\omega t - \omega_E t) \int_0^t \frac{-\tilde{F}}{k^2 + k_d^2} \exp(i\omega t + \omega_E t) dt. \tag{4.18}$$

Let us specify now a particular form of forcing in order to gain further insight into the dynamics of the flow. Consider a vortex travelling with velocity $\mathbf{U_t}$ without changing its spatial structure such that its surface elevation is $\eta_0 = \eta_0(\mathbf{r})$, where $\mathbf{r'} = \mathbf{r} - \mathbf{r_0} - \mathbf{U_t} t$ and $\mathbf{r_0}$ is the initial position of the eddy. In the Fourier space, this translates into $\exp(-i\mathbf{k} \cdot \mathbf{r_0} - i\mathbf{k} \cdot \mathbf{U_t} t)\tilde{\eta_0}$ according to the shift theorem. The forcing can then be written as

$$\tilde{F} = (-ik_d^2 \mathbf{k} \cdot \mathbf{U_t} - i\beta k_x + \lambda k^2) \exp(-i\mathbf{k} \cdot \mathbf{r_0} - i\mathbf{k} \cdot \mathbf{U_t} t)\tilde{\eta_0}. \tag{4.19}$$

Substituting Equation (4.19) into Equation (4.18), we obtain the solution in the form

$$\tilde{\eta} = \frac{i\omega_v - i\omega - \omega_E}{-i\mathbf{k} \cdot \mathbf{U_t} + i\omega + \omega_E} \exp(-i\mathbf{k} \cdot \mathbf{r_0})[\exp(-i\mathbf{k} \cdot \mathbf{U_t} t) - \exp(i\omega t - \omega_E t)]\tilde{\eta_0}, \tag{4.20}$$

where we introduced a vortex frequency

$$\omega_v = \frac{k_d^2 \mathbf{k} \cdot \mathbf{U_t}}{k^2 + k_d^2}. \tag{4.21}$$

In what follows, we use a simple expression for the vortex in the form

$$\eta_0 = \eta_v M(r)[1 + \frac{f_0}{g\eta_v}(U_{ty}x - U_{tx}y)], \tag{4.22}$$

where $M(r)$ is the monopolar component of the vortex which describes its radial structure. The second term in the brackets gives an additional dipolar component which is necessary for the translation of the vortex. The $x$- and $y$- coordinates in Equation (4.22) are defined in a coordinate system with the origin in the center of the vortex. The radial distribution $M(r)$ can be obtained from the experiments. The ratio of the magnitude of the monopolar to dipolar components is determined by the ratio of the azimuthal velocity of the vortex to its translational velocity.

$$A = \frac{V_{\theta v}}{U_t} = \frac{g\eta_v}{f_0 U_t}. \tag{4.23}$$

## 4.5 Results

We performed five experiments with different forcing (Table 4.1); in experiments 2 and 3, the forcing was applied for a relatively short time, $\Delta t = 2 \sim 3$ s, while in the rest of the experiments, the forcing time was $\Delta t = 7 \sim 8$ s. As a result, the vortices in experiments 2 and 3 are of relatively small radius, low amplitude of the surface elevation and, consequently, low energy. The maximum velocity, $V_{\theta v}$, of these low-energy vortices is still relatively high

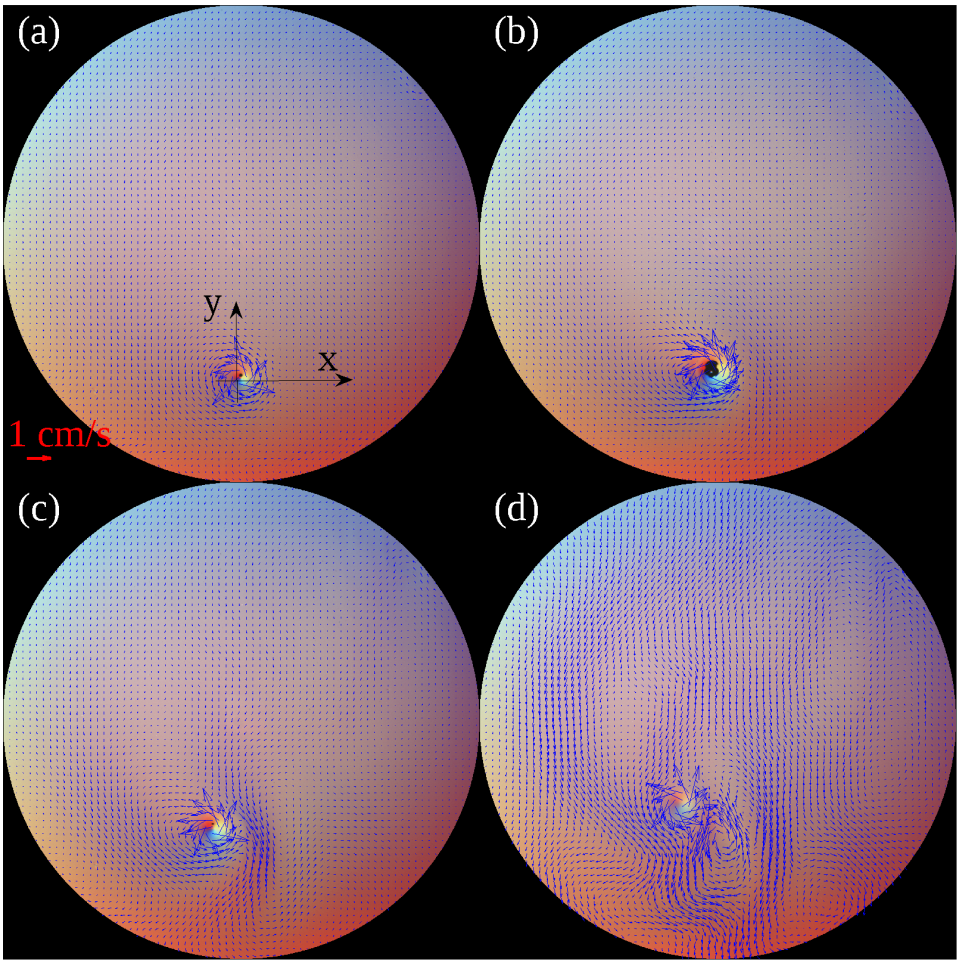


Figure 4.1: Flow evolution in experiment 1 visualized by AIV: (a) the beginning of forcing, $t = 4$ s, (b) the end of the forcing period when the vortex achieved its maximum strength, $t = 9$ s, (c) and (d) unforced vortex, $t = 16$ s and $t = 28$ s. The arrows (blue) indicate the velocity field.

as are the values of parameter $A$ which can be considered as a measure of the nonlinearity. Despite the differences between the control parameters in the experiments, the flows in all of the experiments were qualitatively similar to each other.

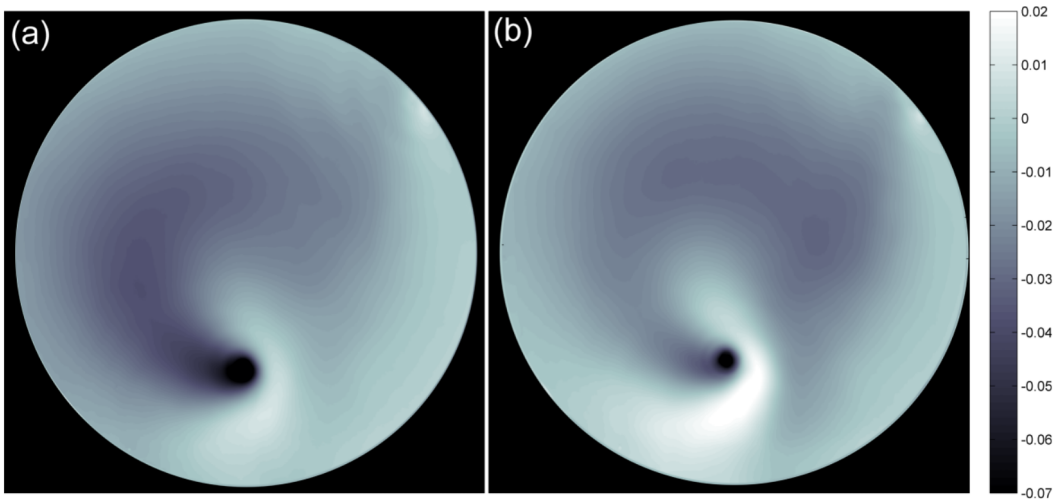


Figure 4.2: Surface elevation field in experiment 1 at $t = 10$ s (a) and $t = 12$ s (b). Gray scale shows $\eta$ in cm.

Figure 4.1 shows a typical evolution of the flow. The color shows $\nabla\eta$ field as recorded by the video camera, while the arrows show the velocity field obtained in the post-processing of the color images as described in Section 4.2. A local coordinate system with $x$-axis directed to the East and $y$-axis directed to the North (the center of the tank is the North pole) is shown in Figure 4.1(a). A cyclonic vortex indicated by a circular rainbow-like color pattern is formed by the forcing (Figure 4.1(a, b)) and then propagates to the Northwest. The vortex radiates Rossby waves; the longer and more zonal waves are to the west of the vortex, while shorter waves are trailing behind the vortex to the East. Note that the altimetric signal due to the waves are weaker than that due to the vortex. A (global) pattern of the Rossby wave in the entire tank can be easily identified in the distribution of the surface elevation (Figure 4.2). The depression of the surface (shown by darker shading) extends westward from the vortex forming a typical $\beta$-plume.

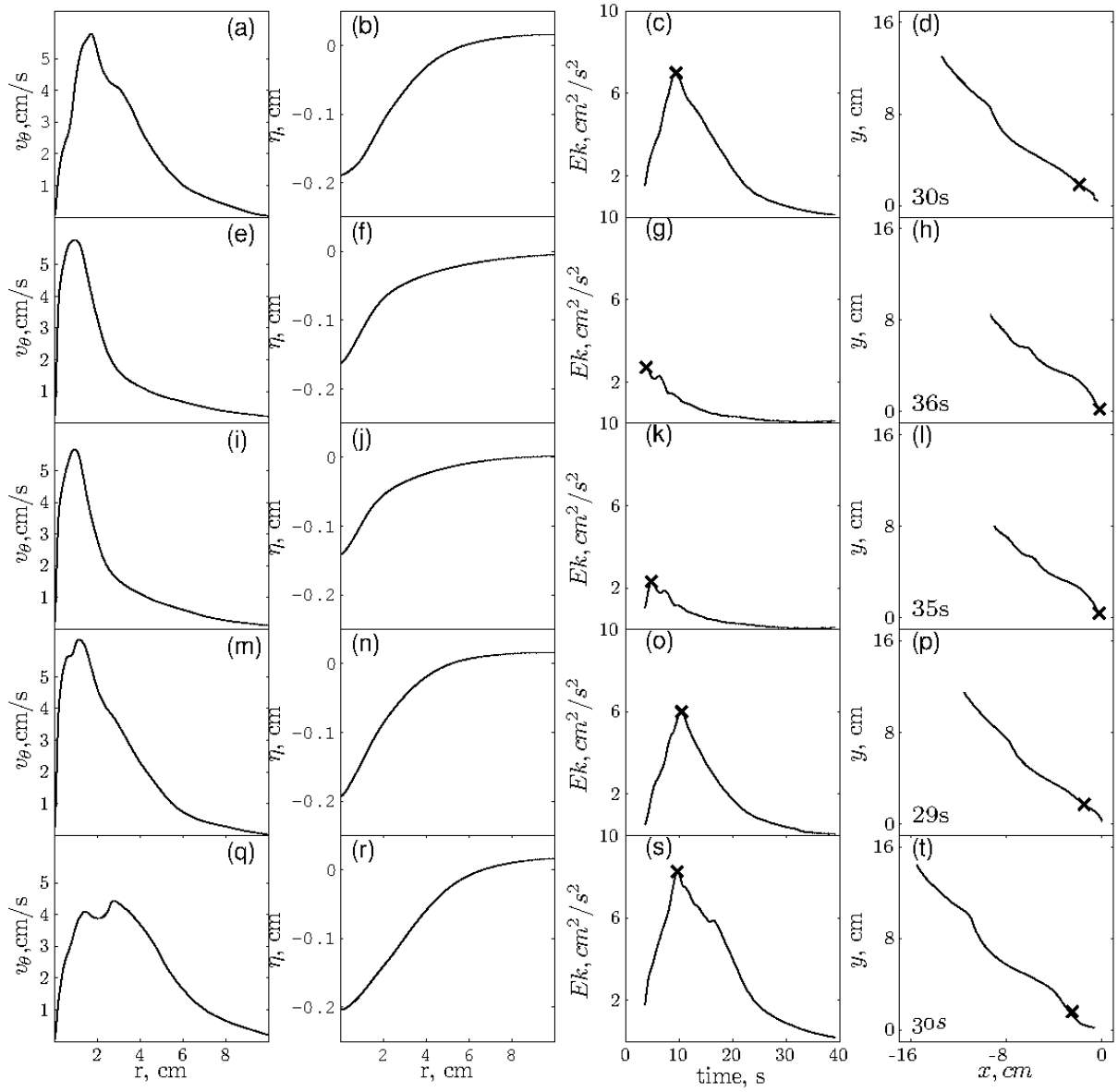


Figure 4.3: Characteristics of vortices measured in experiments 1-5: the azimuthal velocity in cm/s (the first column), the surface elevation in cm (the second column), total kinetic energy as a function of time (the third column), and the vortex trajectory (the fourth column). The total time of travel after the forcing stops is indicated in the last column.

Averaging the azimuthal velocity $v_\theta$ and the surface elevation $\eta$ in the azimuthal direction around a vortex center, we obtained the radial profiles of these two quantities. They are shown in the first and second columns, respectively, in Figure 4.3 for all five experiments. The total kinetic energy, $K$, of a vortex can be obtained by integrating $v_\theta^2/2$ over an area which surrounds the moving vortex at each time (here, we used a circular area of approximately 5 $cm$ radius). The third column in Figure 4.3 gives $K$ as a function of time. The end of the forcing period in each experiment is marked by a cross. During the forcing period, the energy grows linearly, while after the forcing, it is switched off and the energy decays approximately exponentially. By tracking the vortex center (surface elevation minimum), the trajectory of each vortex can be determined. The trajectories for all experiments are shown in the fourth column of Figure 4.3. Crosses denote the position of a vortex when the forcing is switched off. Here, the $x$-component of the vortex displacement was measured in the zonal direction, while the $y$-component was measured along the local North (radial) direction with respect to a reference distance from the pole $r_0$. The trajectories are approximately straight lines such that the direction of propagation is approximately at an angle $\alpha = 140^o$. Note that similar, almost straight trajectories were predicted theoretically in [95] (see their Figs. 1 and 2) for vortices with Gaussian or hurricanelike profiles of vorticity. An axially symmetric monopolar vortex cannot perform translational motion unless a dipolar component is added in order to match the velocity inside the vortex to that of translational motion. On the $\beta$-plane, the breaking of the axial symmetry of the flow is provided by the $\beta$-effect. The so-called $\beta$-gyres are formed within the vortex [94]. The formation of the dipolar $\beta$-gyres is

easy to understand. A cyclonic vortex advects water parcels to the North at its eastern side and to the South at its western side. According to the conservation of potential vorticity, the parcels advected to the North acquire anticyclonic relative vorticity to compensate for the increased background vorticity, while the parcels advected to the South acquire cyclonic relative vorticity. Thus, the additional vorticity forms a dipole with its axis directed to the North which indicates the primary direction of the translational motion. However, the dipole is also affected by the monopolar velocity field and its axis rotates cyclonically. As a result of this complex nonlinear interaction, the axis of the dipolar component and, hence, the direction of the translational motion of the entire vortex is to the Northwest. Similar arguments show that anticyclone propagates to the Southwest. We can use the measured fields to reveal the dipolar component of the flow using Fourier transform in the azimuthal direction.

In a local polar coordinate system attached to a vortex, the surface elevation field could be decomposed into angular modes

$$\eta(r,\theta) = M(r) + a(r)\cos\theta + b(r)\sin\theta, \tag{4.24}$$

where $M(r)$ is the monopolar component which can be calculated as the azimuthal average of $\eta$. The dipolar component is a sum of two orthogonal terms of magnitude $a(r)$ and $b(r)$, respectively. The relative strengths of the two dipolar terms determine the direction of propagation of the vortex. Figure 4.4 shows the surface elevation fields due to the monopolar and dipolar components together with the geostrophic velocity fields corresponding to these components. The fields were measured right after the forcing was stopped in each experiment.

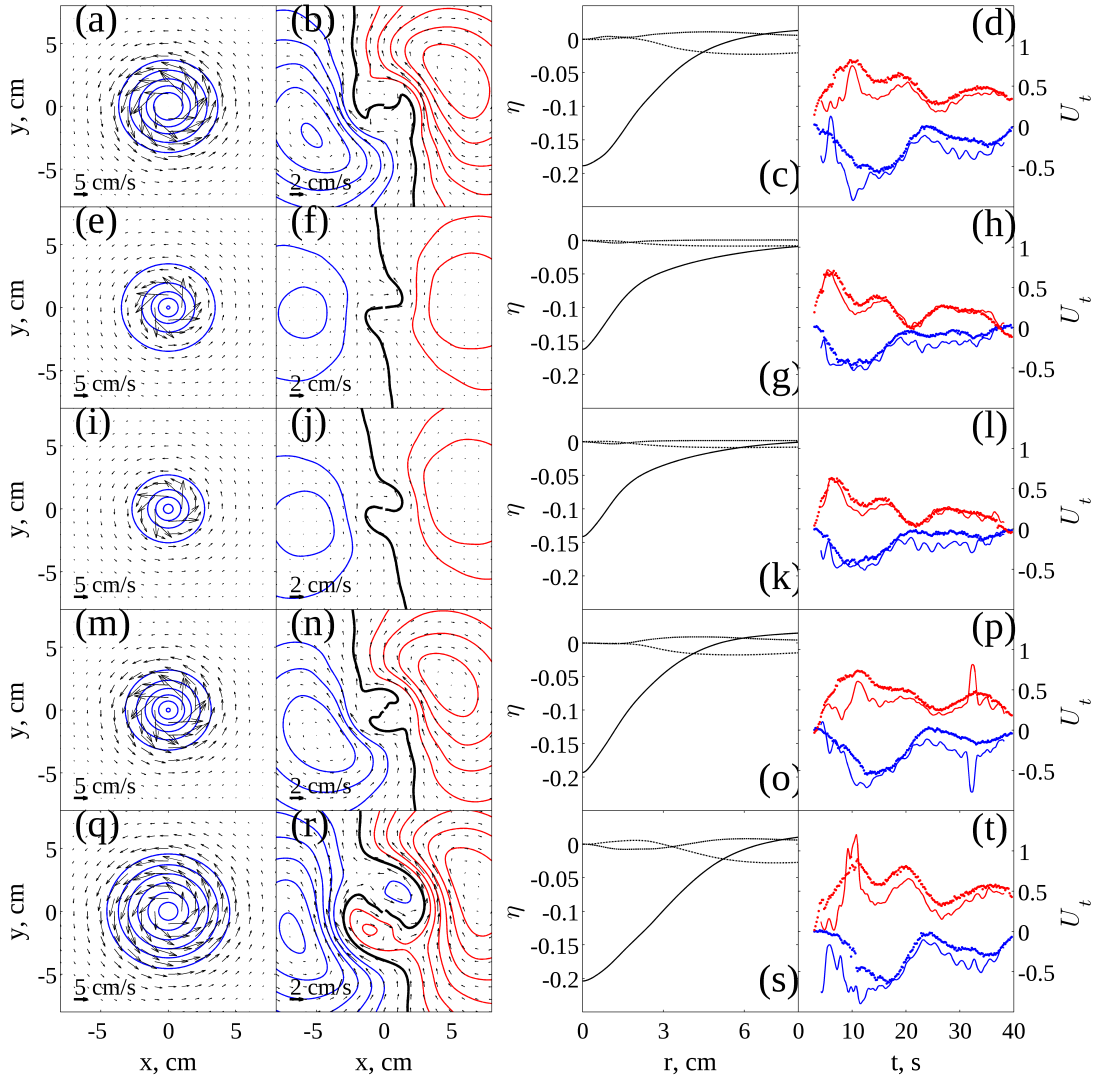


Figure 4.4: Monopolar and dipolar components of the flow in experiments 1 – 5: (the first column) the monopolar component $M$ (contours show $\eta$ in the range from $-0.25$ cm to $-0.03$ cm with 0.03 cm interval and arrows show the geostrophic velocity); (the second column) the dipolar component (contours show $\eta$ in the range from $-0.2$ cm to 0.2 cm with 0.004 cm interval, lighter gray lines (red) indicate positive values, the darker gray lines (blue) indicate negative values, the black shows zero $\eta$, and arrows show the geostrophic velocity); (the third column) radial profiles $M(r)$ (solid line), $a(r)$ (dashed line), and $b(r)$ (dashed-dotted line); and (the fourth column) zonal and meridional components of the translation velocity of the vortex measured in the experiments (solid darker gray/blue and lighter gray/red lines, respectively) and the velocity derived from the dipolar component (dotted lines).

The dipole (the second column in Figure 4.3) has a cyclonic vortex at the southwest and an anticyclone at the northeast such that the axis of the dipole and the main flow induced by the dipole are directed to the Northwest as theory predicts. The magnitudes of $a(r)$ and $b(r)$ are relatively small compared to the monopolar term $M(r)$ (the third column in Figure 4.4). To confirm that the dipole provides the translation of the entire vortex structure, we compared the velocity of the vortex measured in the experiments with that due to the dipole (the fourth column in Figure 4.4). The zonal ($x$) and meridional ($y$) components of the vortex translational velocity, $\mathbf{U_t}$, were measured by tracking the position of the center of the vortex (minimum $\eta$) and then differentiating with respect to time. The velocity due to the dipole was obtained by averaging the geostrophic velocity

$$\mathbf{u_{dipole}} = \frac{g}{f_0}\mathbf{n} \times \nabla \eta_{dipole}, \tag{4.25}$$

where $\eta_{dipole} = a(r)\cos\theta + b(r)\sin\theta$, over the area of the vortex. The comparison between the directly measured velocity $\mathbf{U_t}$ and that calculated from the dipole surface elevation field shows a close match that confirms that the vortex is indeed driven by its dipolar component.

Figure 4.5 shows the monopolar and dipolar components at different times in experiment 1. The sequence in the first column clearly shows that the monopole decays with time. The dipolar fields in the second column in Figure 4.5 exhibit an interesting periodic behavior. The dipole inside the vortex is swirled by the monopolar velocity field such that the dipole can even reverse its direction at the center of the vortex (Figure 4.5(k, n)). Note that the dipole outside of the vortex remains consistently to the Northwest. The swirling of the dipole in the center is due to a nonlinear interaction between the monopolar and dipolar components. As

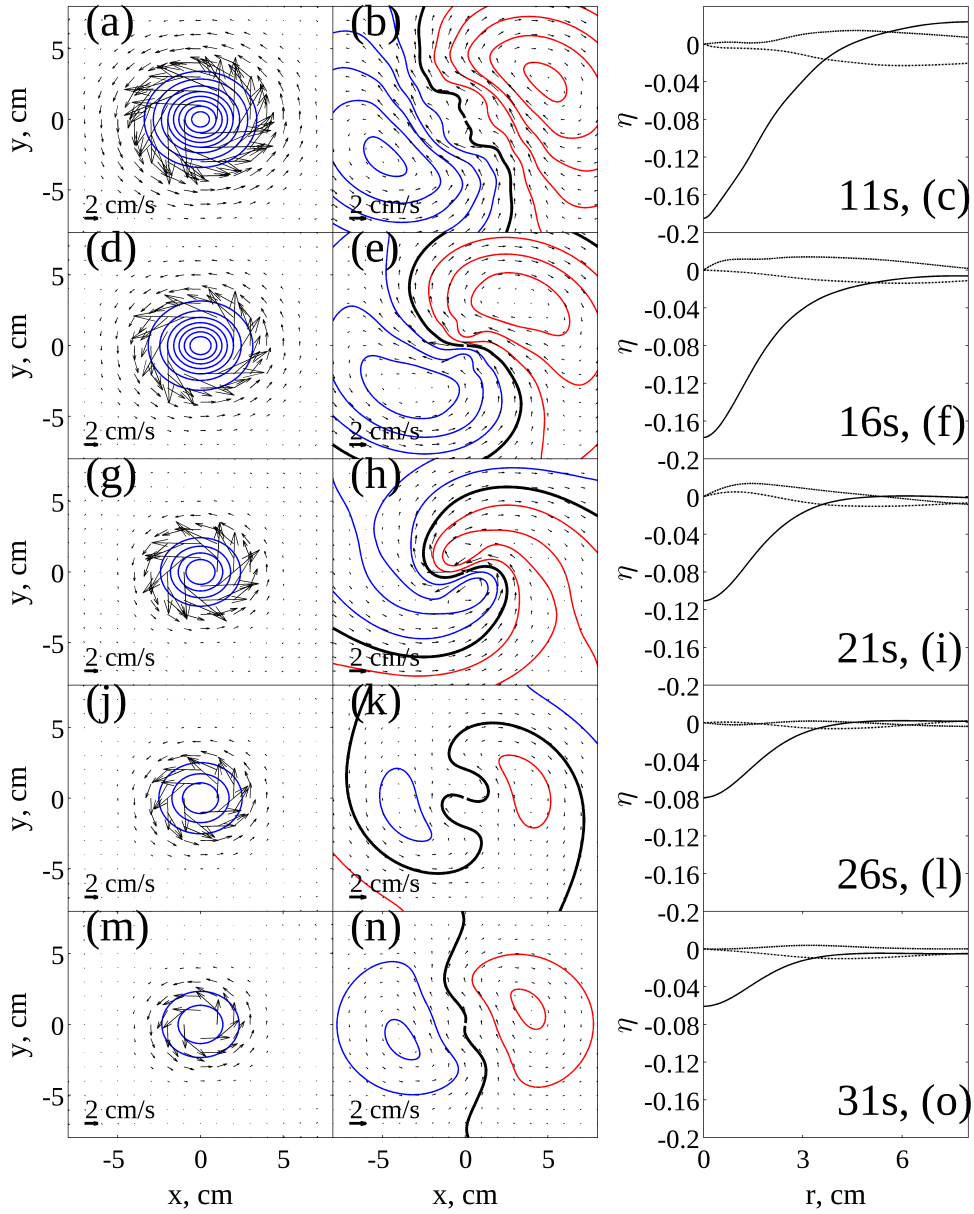


Figure 4.5: Evolution of the monopolar (the first column) and the dipolar (the second column) components of the flow in experiment 1 at $t = 11$ s, 16 s, 21 s, 26 s, and 31 s. The third column gives $M(r)$ (solid line), $a(r)$ (dashed line), and $b(r)$ (dashed-dotted line). The contour lines show $\eta$ with 0.01 cm interval for the monopole and with 0.005 cm interval for the dipole.

a result of the swirling, the translational motion of the entire vortex structure is oscillatory which can be seen clearly in the time sequences of the translational velocity (the fourth column in Figure 4.4). The time of the dipole reverses correlates well with the time when the entire vortex slows down.

We performed numerical simulations of the flow with the control parameters similar to those in the laboratory experiments (Section 4.3). The numerical simulations were initialized with an axisymmetric distribution of the surface elevation mimicking that in the experiment right after the vortex is fully formed. Since the simulations were performed in a rectangular (rather than circular) domain and on a regular (rather than polar) $\beta$-plane, certain differences between the experimental and simulated flows can be noted. These differences arise from a different geometry and the different boundary conditions (such as the presence of a wall in the tank) but they are not crucial for the physical interpretation of the flows. In order to see to what extent can the observed laboratory flows be explained by the linear theory, here we also present the theoretical solutions together with the experimental and numerically simulated flows. We used vortex profiles obtained in the experiments to specify a translating vortex in the RHS of Equation (4.15). The vortex was in a form given by Equation (4.22) where we used experimental data to specify the profile of the monopolar component, $M(r)$, and the translation velocity $\mathbf{U_t}$. The field of surface elevation is then given by the inverse Fourier transform of the solution given by Equation (4.20).

Figure 4.6 shows a comparison of the surface elevation fields between the experiment, numerical simulation, and linear theory, while Figure 4.7 compares relative vorticity fields.

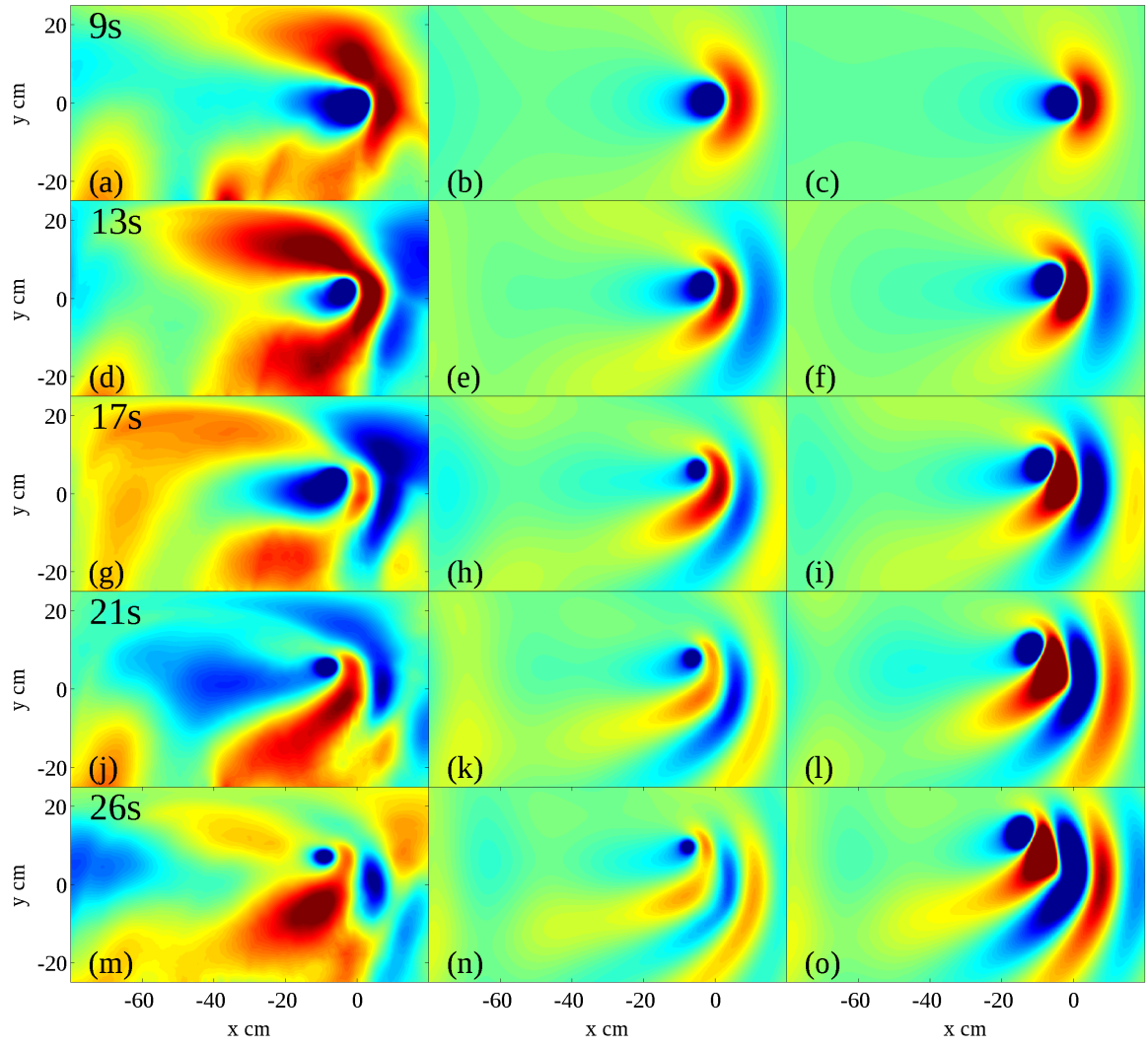


Figure 4.6: Comparison of the surface elevation fields $\eta$ in experiment 1 (the first column), numerical shallow-water simulation (the second column), and linear theory (the third column). Values of $\eta$ is in the range between $-0.03$ cm (darker gray/blue) and 0.03 cm (lighter gray/red).

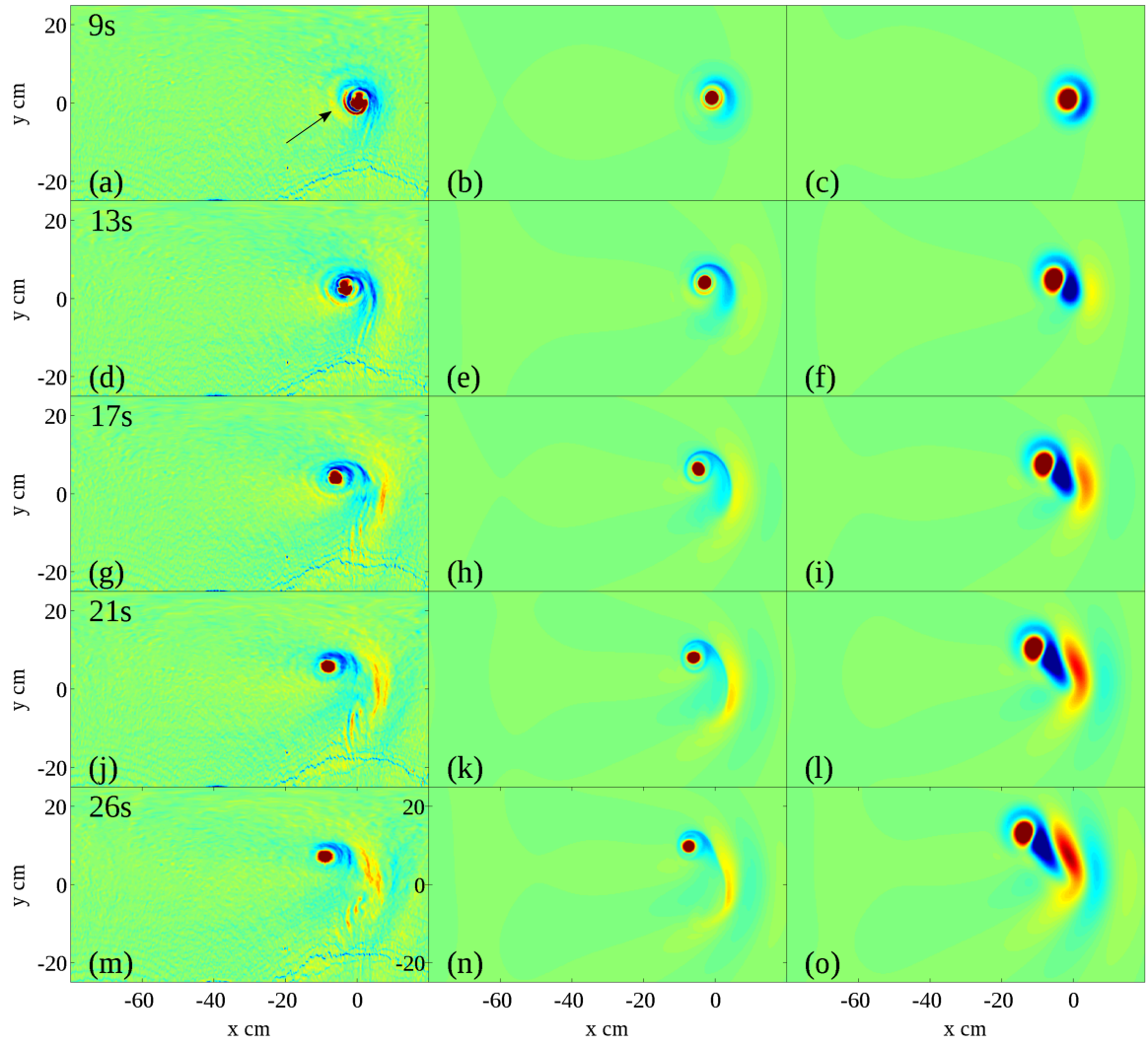


Figure 4.7: Same as in Fig. 7 but for the relative vorticity fields. Vorticity is normalized by the Coriolis parameter and varies in the range between $-0.5$ (darker gray/blue) and 0.5 (lighter gray/red). Arrows indicate the crests of inertial waves emitted by the evolving vortex.

For easier comparison, the laboratory fields were interpolated into a local Cartesian coordinate system with its origin fixed at the position of forcing and $x$- and $y$- axes directed to the East and to the North, respectively. Figures 4.6 and 4.7 show the snapshots of the flow at five different times. There are general similarities between the laboratory, numerical, and theoretical fields. The vortex travels to the northwest, leaving behind a wave trail. The wavecrests have approximately parabolic shape; the waves propagating to the East are short, while the waves propagating to the West are long and approximately zonal as one can expect. The vortex decays in magnitude due to the Ekman friction at the bottom as well as due to regular friction in the bulk of the fluid layer. The comparison between numerical simulations and linear theory shows that the theory predicts quite well the pattern of the waves in the far-field. This confirms the approximately linear character of the radiation in spite of the fact that the vortex itself is strongly nonlinear. It is not entirely surprising since we account for the nonlinearity by specifying the translational motion of the vortex.

The differences between the experimental and simulated or theoretical flows are also worth noting. In particular, the perturbations of $\eta$ at the northern part of the domain appear to be propagating much farther westward in the experiments compared to that in the numerical simulations. Most likely, the reason is geometric, due to the fact that the tank is circular such that the size of the domain in the $x$-direction becomes smaller when approaching the center of the tank. As a result, a circumpolar circulation can be easily established there. A similar effect can be important in real atmospheric flows (and, perhaps, to lesser extent in oceanic flows) and is not accounted for in the regular $\beta$-plane setup.

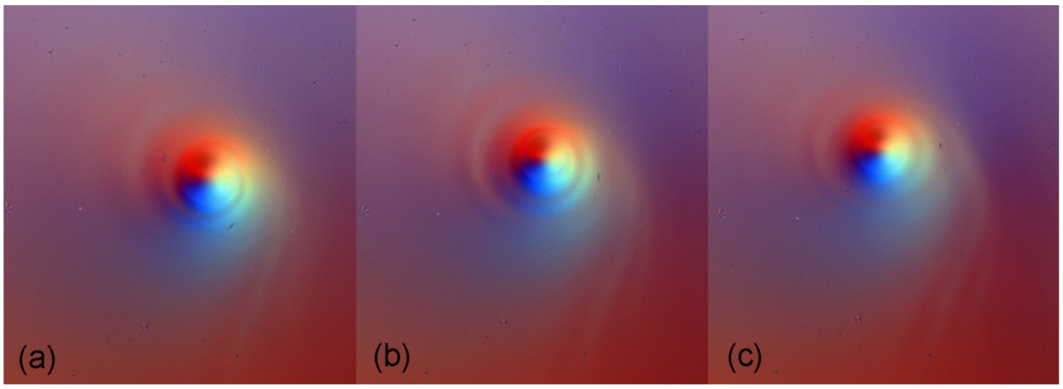


Figure 4.8: Sequence of the altimetric images of the vortex at $t = 10$ s (a), 12 s (b), and 14 s (c). Thin bands spiraling around the vortex are inertial waves.

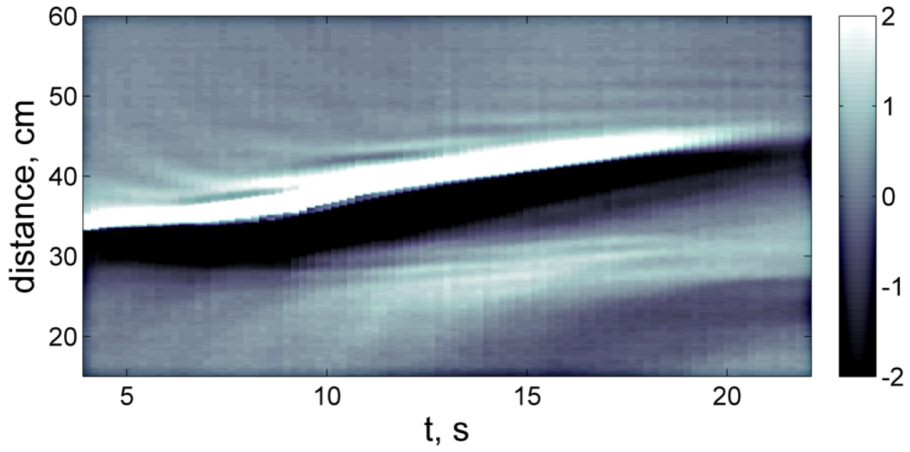


Figure 4.9: Hovmoeller (space-time) diagram of the geostrophic velocity measured along the straight line parallel to the vortex trajectory. Gray scale shows velocity in cm/s.

Relative vorticity fields in Figure 4.7 allow us to see fine features of the flow. The surface elevation (as in Figure 4.6) is obtained by integration of the measured $\nabla\eta$ and, as a result, all small-scale features are smoothened. Vorticity, on the other hand, is a result of differentiation which reveals the fine features (the downside of differentiation of experimental data is, of course, that it amplifies noise). A couple of interesting features can be observed in Figure 4.7. First, the cyclonic vortex generated by suction wraps the negative (anticyclonic) vorticity around itself and thus becomes partially isolated. There is also evidence of instability in the ring of the anticyclonic vorticity when two small satellite anticyclones form and the cyclonic core of the vortex becomes elliptic. Second, inertial waves can be observed in the flow. They are only present in the experimental flow and have an appearance of thin filaments within the patches of vorticity around the vortex (indicated by arrows in Figure 4.7). The emission of inertial waves by a travelling barotropic vortex is of interest in the oceanographic context because it provides a path for the energy transfer from mesoscale eddies to motions of smaller scales (submesoscale). Inertial waves should not be confused with inertial oscillations which are inertia-gravity waves (IGW) in the limit when their frequency approaching the Coriolis frequency $f_0$. IGW are surface waves of frequency above $f_0$. Near-inertial IGW or inertial oscillations are sometimes called in short inertial waves in the oceanographic literature. However, inertial waves have frequency below $f_0$ and are three-dimensional waves that can propagate in the bulk of the fluid. They are otherwise known as Kelvin waves [66] or gyroscopic waves. Inertial waves constitute a basis of linear dynamics of rotating fluid [54]; Rossby waves can in fact be considered as simply a special

type of inertial waves [89]. Inertial waves are important in the process of adjustment of the flow and can also be regarded as spontaneously emitted by an otherwise balanced flow. Some altimetric observations of inertial waves emitted by a meandering coastal flow in a rotating fluid were previously presented in [7].

Since this phenomenon is rarely observed in the experiments, it is worth investigating in more detail. Note that here we report on inertial waves of relatively high frequency (although still below $f_0$) compared to the frequency of Rossby waves. Inertial waves can be easily identified in a sequence of consecutive images of the flow (Figure 4.8) or in a video (not shown here) by their curious feature when the phase of the wave propagates toward the source of the wave rather than away from it (as gravity waves do when say a stone thrown in a pond disturbs the surface of water). To visualize the evolution of the waves and to measure their general characteristics, a Hovmoeller (space-time) diagram was rendered. The diagram in Figure 4.9 shows the distribution of the geostrophic velocity along a straight line at different times. The line was drawn along the vortex trajectory; the velocity component perpendicular to the line was recorded. The vortex, where the velocity changes from positive to negative and is of large magnitude, is visible as white and black bands in the middle of the diagram. The vortex detaches itself from the sink when the forcing stops at approximately 9 $s$ and then moves along the line. The slope of the bands indicates that it moves with an approximately constant velocity. Inertial waves manifest themselves as thin bands above (in front of) and below (behind) the vortex. The inertial waves are superposed on Rossby waves which are of larger scale. The slope of the bands allows us to measure the phase

speed, $c \approx 0.33$ cm/s, while the distance between the lines gives the wavelength, $\lambda \approx 2.7$ cm (which gives the horizontal wavenumber, $k \approx 2.3$ cm$^{-1}$ ). It is interesting to check the measured properties against the dispersion relation for inertial waves. Figure 8 in [7] shows dimensionless frequency, $\omega/f_0$, as a function of dimensionless wavenumber $kR_d$ for different vertical modes. Here, $R_d$ is the barotropic radius of deformation. In our case, the waves are of low frequency, $\omega/f_0 \approx 0.17$ and of high wavenumber, $kR_d \approx 50$. The dispersion relation plot in [7] then shows that these particular values of frequency and wavenumber correspond to the vertical mode of the lowest order which has a simplest vertical structure. Although it is difficult to pinpoint the exact mechanism of emission here, we can hypothesize that the emission is of the spontaneous type as that described in the theoretical study in [49]. This terminology emphasizes that this emission occurs due to the dynamics of the quasi-balanced flow rather than due to an imbalance in the initial conditions. Indeed, our vortex together with its Rossby wave field is approximately balanced within the quasi-geostrophic framework. The (relatively weak) emission of the inertial waves occurs during the entire time of the evolution of the vortex long after the forcing ended. This indicates that this emission is the result of the higher-order dynamics beyond the quasi-geostrophy.

An insight into the dynamics of the Rossby wave radiation by a travelling vortex can be gained by considering an energy spectrum of the flow in the wavenumber space. Two-dimensional energy spectrum is given by

$$E(k_x, k_y) = \frac{1}{2}|\mathbf{u}(k_x, k_y)|^2, \tag{4.26}$$

where $\mathbf{k} = (k_x, k_y)$ is the wavenumber vector and $\mathbf{u}(k_x, k_y)$ represents the discrete Fourier

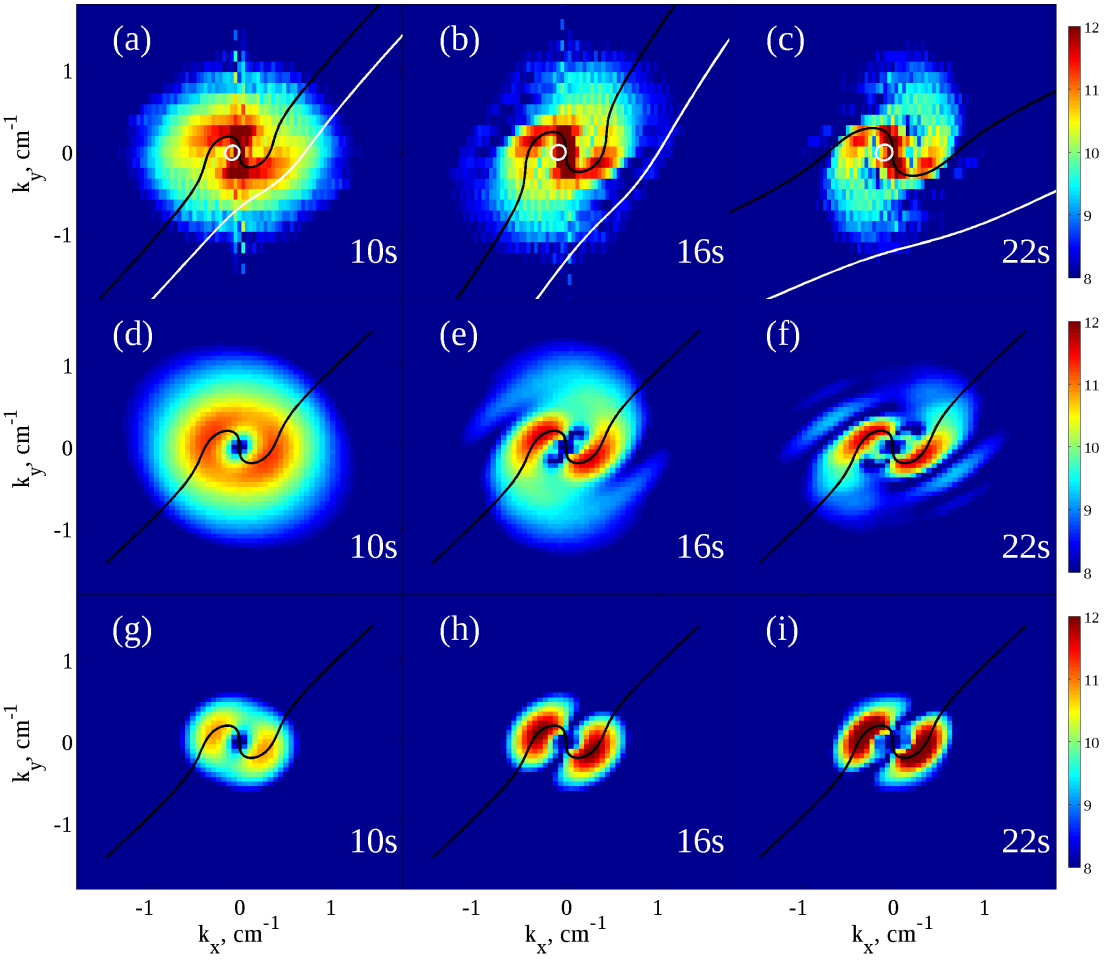


Figure 4.10: Two-dimensional energy spectra, $E(k_x, k_y)$ in experiment 1 (upper row, a-c), numerical simulations (middle row, d-f), and theory (bottom row, g-i) at $t$ = 10 s, 16 s, and 22 s, respectively. Color scale shows $ln(E)$. Solid black lines show the solution of Equation (4.27) with $\omega_0 = 0$. The white curves show the solution of Equation (4.27) with $\omega_0 = 2\pi/\Delta t$, where $\Delta t = 12$ s.

transform of the velocity vector field. Figure 4.10 shows the evolution of the two-dimensional spectrum in experiment 1 together with the spectra of the flow in our numerical simulations and in linear theory. All spectra have a typical inverted S shape. While in the simulations and theory, the energy is mainly located in the lobes at the ends of the S shape; in the experiment, the significant energy is also concentrated at low $k_x$ that indicates that zonal modes are significant. To understand the observed spectra, let us consider theoretical results by Lighthill [70] who described general properties of linear Rossby waves emitted by a moving disturbance (vortex). The disturbance moving with velocity $\mathbf{U_t}$ emits waves of frequency $\omega_0 + \mathbf{k} \cdot \mathbf{U_t}$, where $\omega_0$ is the natural frequency of the disturbance and $\mathbf{k} \cdot \mathbf{U_t}$ is the Doppler shift. For a steady disturbance, $\omega_0 = 0$ and the Doppler shift defines the wave radiation. A disturbance varying over a period of time $\Delta t$ emits transient waves with a spectrum of frequencies varying from 0 to, say, $10/\Delta t$. In our experiments, the vortices are created by forcing over the time period $\Delta t$ such that the transients can be expected in the beginning of each experiment. After the forcing stops, the vortex evolves on a longer time scale determined by dissipation and by a loss of energy due to wave radiation. The wavevector $k$ of a wave of particular frequency can then be determined from the dispersion relation

$$\omega_0 + \mathbf{k} \cdot \mathbf{U_t} = \frac{-\beta k_x}{k^2 + k_d^2}. \tag{4.27}$$

Black lines in Figure 4.10 show $k_y$ as a function of $k_x$ calculated from Equation (4.27) for a stationary disturbance, $\omega_0 = 0$ . Instantaneous values of $\mathbf{U_t}$ were used to calculate the curves for the experiment, while in the simulations and theory, $\mathbf{U_t}$ was constant, $\mathbf{U_t} = 0.7\ cm/s$. While a close fit of the zero frequency curves with the energy pattern in the theoretical

spectrum is not surprising, the fit with the fully nonlinear numerical simulations is somewhat unexpected. The spectrum evolves from an approximately isotropic (Figure 4.10(d)) when the vortex is initially approximately axisymmetric to the anisotropic spectrum (Figure 4.10(e, f)) which corresponds quite well to linear dispersion relation Equation (4.27). Transient waves with frequency corresponding to the forcing time $\Delta t$ can be expected in the experiments. In order to check where the transients are located in the wavenumber space and if their energy signature is noticeable in the experimental spectrum, we plot the curves $\omega_0 = 2\pi/\Delta t$ in Figure 4.10(a-c). At this frequency, Equation (4.27) has two solutions: one is given by an almost straight line and another is a circle near the origin. However, there is no evidence of any concentration of energy along the line since the wavenumbers are relatively large there. The waves with large wavenumbers are not effectively radiated by the relatively large vortex as in our case. The low wavenumber waves corresponding to the circle near the origin can be radiated but they can hardly be distinguished from those corresponding to the zero-frequency curve.

## 4.6 Discussion

In this work, we have shown experimental evidence on the radiation of the Rossby waves by vortices moving on the $\beta$-plane. Vortices are self-propelled due to nonlinear interaction between primary monopolar flow field and the secondary dipolar flow which occurs due to $\beta$-effect as described in [94]. The measurements of the velocity due to the dipolar component

of vortices demonstrated this effect. The cyclones generated by suction in our experiments are strongly nonlinear (similar to oceanic eddies) and propagate to the northwest. Travelling vortices radiate zero-frequency Rossby waves Doppler-shifted by $\mathbf{k} \cdot \mathbf{U_t}$ due to their motion. The pattern of waves is approximately parabolic such that the waves with relatively large wavenumber in (zonal) $x$- direction are to the East of the vortex and waves with small $k_x$ and approximately zonal crests are to the west as discussed in [100]. The radiation of the Rossby waves by vortices (eddies) can be one of the primary mechanisms of the creation of zonal jets observed in the oceans [80, 81]. In fact, this mechanism is the basis of the important theoretical work by [98] on the dynamics of turbulence on the $\beta$-plane. In his original work, Rhines considered a field of closely packed eddies with a narrow spectrum around some wavenumber $k_0$ and assumed that $\beta$-term in the equation of motion is of the same order of magnitude as the nonlinear term. As a result, he obtained a wavenumber

$$k_\beta = \sqrt{\frac{\beta}{V_{rms}}} \tag{4.28}$$

which separates the eddies (turbulence) and waves in the spectral space. Here, $V_{rms}$ is the root-mean-square fluid velocity at the energy containing wavenumber $k_0$. The Rhines scale has been widely discussed in the literature as a suitable measure of the meridional scale of the zonal jets. This work contributes to this discussion as follows. The energy spectra measured in our experiments as well as the spectra obtained in numerical simulations and theory suggest the scaling

$$k_\beta = \sqrt{\frac{\beta}{U_t}}. \tag{4.29}$$

This expression gives the characteristic wavenumber for Rossby waves emitted by a vortex travelling with a speed $U_t$. Similar arguments as those applied for the Rhines scale can be used here to justify that this is an appropriate scaling for zonal flows/jets. Note that the translational velocity $\mathbf{U_t}$ is used here. The translational velocity (at least for highly nonlinear vortices that are self-driven due to the $\beta$-effect) can be much lower than the characteristic rotational velocity in the vortex ($A >> 1$). The characteristic rotational velocity can be interpreted here as an analogue of the $V_{rms}$, the velocity at the energy containing wavenumber $k_0$. For a field of closely packed vortices, originally considered by Rhines, there is no distinction between the two velocities because vortices are driven by strong interactions with each other such that their translational velocity is determined by the flow induced by their nearest neighbors rather than by the $\beta$-effect. However, one can imagine a field of more loosely packed vortices which only occasionally interact with each other but mostly driven by the $\beta$-effect (and perhaps by the mean flow). This is, perhaps, the case in the ocean where mesoscale eddies are formed mostly at the eastern boundaries and then move westward across the oceans. In this case, the relatively subtle distinction between the velocities in Equations (4.28) and (4.29) might be important.

# Chapter 5

# Conclusions

Vortices, waves and zonal jets under the $\beta$-effect, i.e. a background gradient in potential vorticity, are conventional topics in the context of geophysical fluid dynamics. This dissertation addressed the problems firstly regarding the $\beta$-plane turbulence (Chapters 2 and 3) and secondly the wave radiation by a traveling vortex (Chapter 4), using mainly laboratory experiments, together with numerical and analytic methods. An optical system AIV (Altimetry Imaging Velocimetry) was employed in the study to observe the surface elevation gradient field and to measure the velocity in the experiments. A detailed description of the AIV method is given in [8]. High spatial resolution is the primary advantage of this method. Approximately 2000 pixels in each direction of an image resolve wavenumbers with a span of 3 decades in spectral space, which is beyond the reach of previously used laboratory observation techniques, thus making AIV a desirable method for the purpose of spectral analysis. The camera in the optical system captures 5 frames per second, such that

it generates approximately 15 snapshots per revolution ($\Omega = 2.3$ rad/s). AIV directly measures the water surface slopes, or equivalently the zero-order geostrophic currents. Under the quasi-geostrophic approximation (Equation (2.3)) the total velocity can be calculated from the geostrophic component. Consequently, the disadvantage of the AIV method lies with the assumption of the small Rossby number $Ro < 1$. In areas with strong nonlinearity such as inside an eddy the quasi-geostrophic approximation is flawed, as is the total velocity. In a circular vortex, a centripetal force needs to be added in order to account for the underestimated nonlinerity in the quasi-geostrophic approximation. In the experiments on $\beta$-plane turbulence (Chapters 2 and 3), $Ro < 1$ is satisfied almost everywhere in the tank except inside the strong eddies or filaments. In the experiments with a single cyclone (Chapter 4), the focus is the far field where $Ro < 1$ held rather than the strongly nonlinear vortex. Therefore, the observed velocity field in this study is accurate to the first order of quasi-geostrophic approximation.

A barotropic forcing with electromagnetic method (EM) and a baroclinic forcing with a heating wire (thermal) were used to generate the turbulent flows on a topographic $\beta$-plane. Although thermal forcing is baroclinic, the flow kept barotropic to a great extent. Latent jets were observed in the forced-dissipative regime in our EM-forced experiment, and can only be revealed by filtering the velocity fields, which is similar to oceanic jets [80, 81]. A non-dimensional index $R_\beta$ characterizing the forced-dissipative equilibrium of $\beta$-plane turbulence is found to be $R_\beta \approx 1.7$ in this experiment; this represents a transitional regime between a zonostrophic regime ($R_\beta > 2$) where jets dominates and a viscous regime where friction

dominates ($R_\beta < 1.5$). The jets are stronger, relative to the eddies, in the thermal-forced experiment where the forcing was weaker and of a smaller scale. The jets become prominent in the decaying regime in both experiments.

The signal of west-propagating Rossby waves is revealed in physical space, through the Hovmoller diagram, as well as in the frequency-wavenumber space. In the frequency-wavenumber domain Rossby wave propagation manifests itself as the asymmetric energy distribution with respect to $k_x$. Energy concentration along the "turbulence dispersion relation" $\omega = V_{rms}k$ [98] is observed. The asymmetric frequency-wavenumber energy spectra, which are qualitatively similar to those observed in our experiments, were also observed in the middle latitude ocean [129]. This shows a significant energy concentration along the so-called non-dispersive line given by $\omega = \beta R_d^2 k$. This line was tangent to the first-mode baroclinic Rossby wave dispersion curve. Note that flows in our experiments were almost barotropic, so the non-dispersion line represented a wave speed for the gravest mode. However, shorter waves of almost the forcing scale are more energetic than long non-dispersive waves in the experiments.

The energy spectrum in $k_x - k_y$ wavenumber space shows anisotropy where the analogue of the Rhine scale, i.e. $k_\beta$ or $k_R$ acts as a boundary of a dumbbell shape between the wave regime and the nonlinear regime. Less energy inside the dumbbell was observed; however, the dumbbell does not hinder energy cascades to the zonal modes of approximately the forcing scale. It is interesting to see that the spectrum evolution predicted by the linear dynamics of $\beta$-plume theory agrees qualitatively with the observations, where an isotropic forcing at

the initial moment evolves into anisotropy.

Baroclinic turbulence in a 2-layer system is studied with a focus on its spectral characteristics. The flow is initially triggered by a coastal current flowing on top of a saline layer. Baroclinic instability due to the shear between two layers gives rise to large-scale meanders and waves, as well as small-scale eddies and filaments. In two-dimensional wavenumber space, Rhines's theory is validated in this baroclinic case. Energy concentration on the zonal modes larger than the Rhine scale is observed, as anisotrophy manifests as less energy locating inside a dumbbell-shaped curve. In order to include all the data points and eliminate the geometric distortion due to the local $\beta$-plane, the Fourier-Bessel spectrum is employed in parallel. Analogues of Rhines's arguments work in the Fourier-Bessel spectra. The energy distribution in frequency wavenumber space shows a good correspondence to the dispersion relations of the westward-propagating Rossby waves as well as those of the eastward-propagating baroclinic instability waves. This emphasizes the significance of linear dynamics in the 2-layer case even though nonlinearity is strong. The one-dimensional spectrum in the frequency domain is similar to that found in the mid-latitude ocean [129]. Two frequencies are proposed that characterize the time scale of baroclinic instability and that of small Rossby waves, respectively.

Encouraged by the good prediction of spectrum evolution by solely the linear dynamics in Chapter 2, and also by the significance of linear control in the baroclinic flow in Chapter 3, Chapter 4 extends the $\beta$-plume theory to an idealized case: wave radiation by a traveling vortex. In a series of experiments, intense cyclonic vortices were generated by siphoning

water out of the tank. Vortex strength was varied by adjusting the forcing period and voltage applied on the pump. In all the experiments, a cyclonic vortex propagates northwestward; meanwhile, it radiates long Rossby waves with quasi-zonal wave crests aligned to the West, leaving a tail of short waves to the East. A similar scenario was observed in numerical simulation as well. Experiments showed the existence of inertial waves triggered by the cyclone, though it was not captured by the pseudo-spectral model. $\beta$-gyres theory is validated in these experiments; that is, the $\beta$-gyres/dipole component of the vortex determines the vortex translation speed and direction. The dipole component is advected by the primary monopole anti-clockwise such that the dipole axis as well as the vortex translation direct to the Northwest. Small oscillations in the Lagrangian trajectory of the $\beta$-drift are owing to the reverse events of the dipole near the vortex center.

The wave field (far field) predicted by the $\beta$-plume theory resembles those in the experiments and model simulation. In addition, energy distribution in $k_x - k_y$ wavenumber space by linear dynamics agrees qualitatively with the energy spectrum of the flows generated in the laboratory experiments and fully-nonlinear simulation. This study validates the significant control of linear dynamics in the radiated wave field triggered by a travelling vortex, which is strongly nonlinear. The connection of the present work to the celebrated Rhines scale is $\mathbf{U_t}$, the vortex translation speed. As shown in Section 4.5 vortex translation speed is determined by the dipole component, which could be considered as the local wave field in the vicinity of the vortex; therefore, $\mathbf{U_t}$ could be interpreted further as the upper limit of the characteristic velocity scale of the wave field. The Rhine scale was originally proposed

for the fully turbulent flows where eddy interaction dominates, and thus the characteristic velocity scale $V_{rms}$ is close to the swirling velocity inside the vortices. However, in a case of the $\beta$-drift, nonlinearity is greatly confined inside the vortex such that there is a distinct scale separation between the vortex-dominated flow and the wave field. $U_t$ naturally characterizes the whole field due to the widespread waves. Although $\sqrt{\frac{\beta}{U_t}}$ is not an exact analogue to the Rhines scale physically, the curves in Figure 4.10 follow correctly the energy lobes in wavenumber space. The scale-dependency of characteristic velocity requires caution when applying the Rhines scale in the ocean, where sparsely distributed vortices interact with each other through radiated waves.

# Bibliography

[1] J. Adem. A series solution for barotropic vorticity equation and its application in the study of atmospheric vortices. *Tellus*, VIII:364–372, 1956.

[2] Y. D. Afanasyev and J. D. C. Craig. Rotating shallow water turbulence: experiments with altimetry. *Phys. Fluids.*, 25:106603, 2013.

[3] Y. D. Afanasyev and V. N. Korabel. Wakes and vortex streets generated by translating force and force doublet: laboratory experiments. *J. Fluid Mech.*, 553:119–141, 2006.

[4] Y. D. Afanasyev, S. OLeary, P. B. Rhines, and E. G. Lindahl. On the origin of jets in the ocean. *Geoph. Astroph. Fluid*, 106(2):113, 2012.

[5] Y. D. Afanasyev and J. Wells. Quasi-two-dimensional turbulence on the polar beta-plane: laboratory experiments. *Geoph. Astroph. Fluid*, 99:1, 2005.

[6] Yakov D Afanasyev. Altimetry in a GFD laboratory and flows on the polar $\beta$-plane. In T. von Larcher and P. Williams, editors, *Modeling Atmospheric and Oceanic Flows: Insights from Laboratory Experiments and Numerical Simulations*, volume 205. John Wiley & Sons, 2015.

[7] YD Afanasyev, PB Rhines, and EG Lindahl. Emission of inertial waves by baroclinically unstable flows: Laboratory experiments with altimetric imaging velocimetry. *J. Atmos. Sci.*, 65(1):250–262, 2008.

[8] YD Afanasyev, PB Rhines, and EG Lindahl. Velocity and potential vorticity fields measured by altimetric imaging velocimetry in the rotating fluid. *Exp. Fluids*, 47(6):913–926, 2009.

[9] David LT Anderson and AE Gill. Spin-up of a stratified ocean, with applications to upwelling. In *Deep-Sea Res.*, volume 22, pages 583–596. Elsevier, 1975.

[10] Brian K Arbic, Robert B Scott, Glenn R Flierl, Andrew J Morten, James G Richman, and Jay F Shriver. Nonlinear cascades of surface oceanic geostrophic kinetic energy in the frequency domain. *J. Phys. Ocean.*, 42(9):1577–1600, 2012.

[11] Nikolaos A Bakas and Petros J Ioannou. On the mechanism underlying the spontaneous emergence of barotropic zonal jets. *J. Atmos. Sci.*, 70(7):2251–2271, 2013.

[12] Mark P Baldwin, PB , HP Huang, and ME McIntyre. Atmospheres: The jet-stream conundrum. *Science*, 315(5811):467, 2007.

[13] AM Balk, VE Zakharov, and SV Nazarenko. Nonlocal turbulence of drift waves. *Soviet Phys. JETP*, 71:249–260, 1990.

[14] P Berloff and I Kamenkovich. On spectral analysis of mesoscale eddies. part i: Linear analysis. *J. Phys. Ocean.*, 43(12):2505–2527, 2013.

[15] P Berloff and I Kamenkovich. On spectral analysis of mesoscale eddies. part ii: Nonlinear analysis. *J. Phys. Ocean.*, 43(12):2528–2544, 2013.

[16] P Berloff, I Kamenkovich, and Joseph Pedlosky. A model of multiple zonal jets in the oceans: Dynamical and kinematical analysis. *J. Phys. Ocean.*, 39(11):2711–2734, 2009.

[17] P Berloff, S Karabasov, J Thomas Farrar, and Igor Kamenkovich. On latency of multiple zonal jets in the oceans. *J. Fluid Mech.*, 686:534–567, 2011.

[18] Pavel Berloff, Igor Kamenkovich, and Joseph Pedlosky. A mechanism of formation of multiple zonal jets in the oceans. *J. Fluid Mech.*, 628:395–425, 2009.

[19] GJ Boer and TG Shepherd. Large-scale two-dimensional turbulence in the atmosphere. *J. Atmos. Sci.*, 40(1):164–184, 1983.

[20] G. Boffetta and R.E. Ecke. Two-dimensional turbulence. *Annu. Rev. Fluid Mech.*, 44:427, 2012.

[21] Freddy Bouchet and Antoine Venaille. Statistical mechanics of two-dimensional and geophysical flows. *Phys. Rep.*, 515(5):227–295, 2012.

[22] Jean-Philippe Boulanger and Christophe Menkes. Propagation and reflection of long equatorial waves in the pacific ocean during the 1992–1993 el nino. *J. Geophys. Res.*, 100(C12):25041–25059, 1995.

[23] John P Boyd. *Chebyshev and Fourier spectral methods*. Courier Corporation, 2001.

[24] A Bracco, JC McWilliams, G Murante, A Provenzale, and JB Weiss. Revisiting freely decaying two-dimensional turbulence at millennial resolution. *Phys. Fluids*, 12(11):2931–2941, 2000.

[25] Jörn Callies, Raffaele Ferrari, Jody M Klymak, and Jonathan Gula. Seasonality in submesoscale turbulence. *Nat. Commun.*, 6, 2015.

[26] XAVIER Capet, JAMES C McWilliams, M JEROEN Molemaker, and AF Shchepetkin. Mesoscale to submesoscale transition in the california current system. part i: Flow structure, eddy flux, and observational tests. *J. Phys. Ocean.*, 38(1):29–43, 2008.

[27] XAVIER Capet, JAMES C McWilliams, M JEROEN Molemaker, and AF Shchepetkin. Mesoscale to submesoscale transition in the california current system. part ii: Frontal processes. *J. Phys. Ocean.*, 38(1):44–64, 2008.

[28] Johnny CL Chan and RT Williams. Analytical and numerical studies of the beta-effect in tropical cyclone motion. part i: Zero mean flow. *J. Atmos. Sci.*, 44(9):1257–1265, 1987.

[29] Alexei Chekhlov, Steven A Orszag, Semion Sukoriansky, Boris Galperin, and Ilya Staroselsky. The effect of small-scale forcing on large-scale structures in two-dimensional flows. *Physica D*, 98(2):321–334, 1996.

[30] D.B. Chelton and Michael G. Schlax. Global observations of oceanic rossby waves. *Science*, 272:234, 1996.

[31] Dudley B Chelton, Michael G Schlax, and Roger M Samelson. Global observations of nonlinear mesoscale eddies. *Prog. Oceanogr.*, 91(2):167–216, 2011.

[32] Ru Chen, Glenn R Flierl, and Carl Wunsch. Quantifying and interpreting striations in a subtropical gyre: A spectral perspective. *J. Phys. Ocean.*, 45(2):387–406, 2015.

[33] Navid C Constantinou, Brian F Farrell, and Petros J Ioannou. Emergence and equilibration of jets in beta-plane turbulence: applications of stochastic structural stability theory. *J. Atmos. Sci.*, 71(5):1818–1842, 2014.

[34] Benoit Cushman-Roisin and Jean-Marie Beckers. *Introduction to geophysical fluid dynamics: physical and numerical aspects*, volume 101. Academic Press, 2011.

[35] Yves Dandonneau, Andres Vega, Hubert Loisel, Yves Du Penhoat, and Christophe Menkes. Oceanic rossby waves acting as a" hay rake" for ecosystem floating by-products. *Science*, 302(5650):1548–1551, 2003.

[36] Sergey Danilov and Vladimir M Gryanik. Barotropic beta-plane turbulence in a regime with strong zonal jets revisited. *J. Atmos. Sci.*, 61(18):2283–2295, 2004.

[37] Sergey Danilov and David Gurarie. Scaling, spectra and zonal jets in beta-plane turbulence. *Phys. Fluids*, 16(7):2592–2603, 2004.

[38] M. K. Davey and P. D. Killworth. Flows produced by discrete sources of buoyancy. *J. Phys. Ocean.*, 19:1279, 1989.

[39] A. Coline de Verdiere. Mean flow generation by topographic rossby waves. *J. Fluid Mech.*, 94:39–64, 1979.

[40] T. E. Dowling. Dynamics of jovian atmospheres. *Annu. Rev. Fluid Mech.*, 27:293, 1995.

[41] DG Dritschel and ME McIntyre. Multiple jets as pv staircases: the phillips effect and the resilience of eddy-transport barriers. *J. Atmos. Sci.*, 65(3):855–874, 2008.

[42] Stefania Espa, Isabella Bordi, Thomas Frisius, Klaus Fraedrich, Antonio Cenedese, and Alfonso Sutera. Zonal jets and cyclone–anticyclone asymmetry in decaying rotating turbulence: laboratory experiments and numerical simulations. *Geophys. Astrophys. Fluid*, 106(6):557–573, 2012.

[43] Raffaele Ferrari and Carl Wunsch. The distribution of eddy kinetic and potential energies in the global ocean. *Tellus*, 62(2):92–108, 2010.

[44] Ragnar Fjørtoft. On the changes in the spectral distribution of kinetic energy for two dimensional, nondivergent flow. *Tellus*, 5(3), 1953.

[45] G. R. Flierl. The application of linear quasi-geostrophic dynamics to gulf stream rings. *J. Phys. Ocean.*, 7:365–397, 1977.

[46] G. R. Flierl and R. C. Beardsley. The behavior of a barotropic eddy on beta plane. *J. Phys. Ocean.*, 6:57–65, 1976.

[47] J.B. Flor and I. Eames. Dynamics of the monopolar vortices on a topographic beta-plane. *J. Fluid Mech.*, 456, 2002.

[48] Jérôme Fontane, David G Dritschel, and Richard K Scott. Vortical control of forced two-dimensional turbulence. *Phys. Fluids*, 25(1):015101, 2013.

[49] Rupert Ford, Michael E McIntyre, and Warwick A Norton. Balance and the slow quasimanifold: some explicit results. *J. Atmos. Sci.*, 57(9):1236–1254, 2000.

[50] R. C. Kloosterziel G. F. Carnevale and G. J. F. van Heijst. Propagation of barotropic vortices over topography in a rotating tank. *J. Fluid Mech.*, 233:119–139, 1991.

[51] B. Galperin, S. Sukoriansky, N. Dikovskaya, P. L. Read, Y. H. Yamazaki, and R. Wordsworth. Anisotropic turbulence and zonal jets in rotating flows with a -effect. *Nonlinear Pro. Geoph.*, 13:83, 2006.

[52] B. Galperin, S. Sukoriansky, and H.-P. Huang. Universal $n^{-5}$ spectrum of zonal flows on giant planets. *Phys. Fluids*, 13:1545, 2001.

[53] Boris Galperin, Hideyuki Nakano, Huei-Ping Huang, and Semion Sukoriansky. The ubiquitous zonal jets in the atmospheres of giant planets and earth's oceans. *Geophys. Res. Lett.*, 31(13), 2004.

[54] Harvey Philip Greenspan. *The theory of rotating fluids*. CUP Archive, 1968.

[55] Jonathan Gula, M Jeroen Molemaker, and James C McWilliams. Submesoscale dynamics of a gulf stream frontal eddy in the south atlantic bight. *J. Phys. Ocean.*, pages 305–325, 2015.

[56] George R Halliwell Jr, Young Jae Ro, and Peter Cornillon. Westward-propagating sst anomalies and baroclinic eddies in the sargasso sea. *J. Phys. Ocean.*, 21(11):1664–1680, 1991.

[57] Isaac M Held. Stationary and quasi-stationary eddies in the extratropical troposphere: Theory. *Large-scale dynamical processes in the atmosphere*, pages 127–168, 1983.

[58] Karl R Helfrich and Kevin G Speer. Oceanic hydrothermal circulation: Mesoscale and basin-scale flow. In L. S. Mullineaux S. E. Humphris, R. A. Zierenberg and R. E. Thomson, editors, *Seafloor hydrothermal systems: physical, chemical, biological, and geological interactions*, pages 347–356. Wiley Online Library, 1995.

[59] Neil J Holbrook, Ian D Goodwin, Shayne McGregor, Ernesto Molina, and Scott B Power. Enso to multi-decadal time scale changes in east australian current transports and fort denison sea level: Oceanic rossby waves as the connecting mechanism. *Deep-Sea Res. Pt. II*, 58(5):547–558, 2011.

[60] Greg Holloway and Myrl C Hendershott. Stochastic closure for nonlinear rossby waves. *J. Fluid Mech.*, 82(04):747–765, 1977.

[61] Brian J Hoskins and Fei-Fei Jin. The initial value problem for tropical perturbations to a baroclinic atmosphere. *Q. J. Roy. Meteor. Soc.*, 117(498):299–317, 1991.

[62] Brian J Hoskins and David J Karoly. The steady linear response of a spherical atmosphere to thermal and orographic forcing. *J. Atmos. Sci.*, 38(6):1179–1196, 1981.

[63] Huei-Ping Huang and Walter A Robinson. Two-dimensional turbulence and persistent zonal jets in a global barotropic model. *J. Atmos. Sci.*, 55(4):611–632, 1998.

[64] Terrence M Joyce and Kevin G Speer. Modeling the large-scale influence of geothermal sources on abyssal flow. *J. Geophys. Res.*, 92(C3):2843–2850, 1987.

[65] Michio Kawamiya and Andreas Oschlies. Formation of a basin-scale surface chlorophyll pattern by rossby waves. *Geophys. Res. Lett*, 28(21):4139–4142, 2001.

[66] Lord Kelvin. Vibrations of a columnar vortex. *Phil. Mag*, 10(5):155–168, 1880.

[67] William S Kessler. Observations of long rossby waves in the northern tropical pacific. *J. Geophys. Res.*, 95(C4):5183–5217, 1990.

[68] Gennady K. Korotaev and Alexander B. Fedotov. Dynamics of an isolated barotropic eddy on a beta-plane. *J. Fluid Mech.*, 264, 1994.

[69] R. Kraichnan. Inertial ranges in two-dimensional turbulence. *Phys. Fluids.*, 10:1417, 1967.

[70] MJ Lighthill. On waves generated in dispersive systems to travelling forcing effects, with applications to the dynamics of rotating fluids. In *Hyperbolic Equations and Waves*, pages 124–152. Springer, 1970.

[71] Andrew J Majda and Joseph A Biello. The nonlinear interaction of barotropic and equatorial baroclinic rossby waves. *J. Atmos. Sci.*, 60(15):1809–1821, 2003.

[72] ME Maltrud and GK Vallis. Energy spectra and coherent structures in forced two-dimensional and beta-plane turbulence. *J. Fluid Mech.*, 228:321–342, 1991.

[73] AJ Manfroi and WR Young. Slow evolution of zonal jets on the beta plane. *J. Atmos. Sci.*, 56(5):784–800, 1999.

[74] Nathan J Mantua and David S Battisti. Evidence for the delayed oscillator mechanism for enso: The observed oceanic kelvin mode in the far western pacific. *J. Phys. Ocean.*, 24(3):691–699, 1994.

[75] Philip S Marcus and Sushil Shetty. Jupiter's zonal winds: are they bands of homogenized potential vorticity organized as a monotonic staircase? *Philosophical Transactions of the Royal Society of London A: Mathematical, Physical and Engineering Sciences*, 369(1937):771–795, 2011.

[76] PS Marcus and C Lee. A model for eastward and westward jets in laboratory experiments and planetary atmospheres. *Phys. Fluids*, 10(6):1474–1489, 1998.

[77] D. Marteau, O. Cardoso, and P. Tabeling. Equilibrium states of two-dimensional turbulence: an experimental study. *Phys. Rev. E.*, 51:5124, 1995.

[78] AM Matulka and YD Afanasyev. Zonal jets in equilibrating baroclinic instability on the polar beta-plane: Experiments with altimetry. *J. Geophys. Res.*, 120(9):6130–6144, 2015.

[79] AM Matulka, Y Zhang, and YD Afanasyev. Complex environmental [beta]-plane turbulence: laboratory experiments with altimetric imaging velocimetry. *Nonlinear Proc. Geoph.*, 23(1):21, 2016.

[80] N. A. Maximenko, B. Bang, and H. Sasaki. Observational evidence of alternating zonal jets in the world ocean. *Geoph. Res. Lett.*, 32:L12607, 2005.

[81] N. A. Maximenko, O. V. Melnichenko, P. P. Niiler, and H. Sasaki. Stationary mesoscale jet-like features in the ocean. *Geoph. Res. Lett.*, 32:L08603, 2008.

[82] N. R. McDonald. The decay of cyclonic eddies by rossby wave radiation. *J. Fluid Mech.*, 361:237–252, 1998.

[83] ME McIntyre. Potential-vorticity inversion and the wave-turbulence jigsaw: some recent clarifications. *Adv. Geosciences*, 15(15):47–56, 2008.

[84] J. C. McWilliams and G. R. Flierl. On the evolution of isolated nonlinear vortices. *J. Phys. Ocean.*, 9:1155–1182, 1979.

[85] Gary Meyers. On the annual rossby wave in the tropical north pacific ocean. *J. Phys. Ocean.*, 9(4):663–674, 1979.

[86] R Lee Panetta. Zonal jets in wide baroclinically unstable regions: Persistence and scale selection. *J. Atmos. Sci.*, 50(14):2073–2106, 1993.

[87] Joseph Pedlosky. *Geophysical fluid dynamics*. Springer Science & Business Media, 2013.

[88] Norman A Phillips. A simple three-dimensional model for the study of large-scale extratropical flow patterns. *J. Atmos. Sci.*, 8(6):381–394, 1951.

[89] Norman A Phillips. Elementary rossby waves. *Tellus*, 17(3):295–301, 1965.

[90] Paulo S Polito and Peter Cornillon. Long baroclinic rossby waves detected by topex/poseidon. *J. Geophys. Res.*, 102(C2):3215–3235, 1997.

[91] Bo Qiu, Robert B Scott, and Shuiming Chen. Length scales of eddy generation and nonlinear evolution of the seasonally modulated south pacific subtropical countercurrent. *J. Phys. Ocean.*, 38(7):1515–1528, 2008.

[92] P. L. Read, Y. H. Yamazaki, S. R. Lewis, R. Wordsworth P. D. Williams, J. Sommeria K. Miki-Yamazaki, and H. Didelle. Dynamics of convectively driven banded jets in the laboratory. *Earth Planet. Sci. Lett.*, 64:40314052, 2007.

[93] PL Read, BJ Conrath, LN Fletcher, PJ Gierasch, AA Simon-Miller, and LC Zuchowski. Mapping potential vorticity dynamics on saturn: Zonal mean circulation from cassini and voyager data. *Planet Space Sci.*, 57(14):1682–1698, 2009.

[94] G. M. Reznik. Dynamics of localized vortices on the beta plane. *Atmospheric and Oceanic Physics*, 46:784–797, 2010.

[95] G. M. Reznik and W. Dewar. An analytical theory of distributed axismmetric barotropic vortices on the beta plane. *J. Fluid Mech.*, 269:301–321, 1994.

[96] P. B. Rhines. Slow oscillations in an ocean of varying depth part 1. abrupt topography. *J. Fluid Mech.*, 37(01):161–189, 1969.

[97] P. B. Rhines. Slow oscillations in an ocean of varying depth part 2. islands and seamounts. *J. Fluid Mech.*, 37(01):191–205, 1969.

[98] P. B. Rhines. Waves and turbulence on a beta-plane. *J. Fluid Mech.*, 69:417, 1975.

[99] P. B. Rhines. Jets and orography: Idealized experiments with tip-jets and lighthill blocking. *J. Atmos. Sci.*, 64:3627, 2007.

[100] Peter B Rhines. The dynamics of unsteady currents. In *The sea*, volume 6, pages 189–318. Harvard U. Press, 1977.

[101] MK Rivera, WB Daniel, SY Chen, and RE Ecke. Energy and enstrophy transfer in decaying two-dimensional turbulence. *Phys. Rev. Lett.*, 90(10):104502, 2003.

[102] CG Rossby. On displacements and intensity changes of atmospheric vortices. *J. mar. Res*, 7(175):71, 1948.

[103] Carole M Sakamoto, David M Karl, Hans W Jannasch, Robert R Bidigare, Ricardo M Letelier, Peter M Walz, John P Ryan, Paulo S Polito, and Kenneth S Johnson. Influence of rossby waves on nutrient dynamics and the plankton community structure in the north pacific subtropical gyre. *J. Geophys. Res.*, 109(C5), 2004.

[104] L Zavala Sansón and GJF Van Heijst. Interaction of barotropic vortices with coastal topography: Laboratory experiments and numerical simulations. *J. Phys. Ocean.*, 30(9):2141–2162, 2000.

[105] Niklas Schneider and Arthur J Miller. Predicting western north pacific ocean climate. *J. Climate*, 14(20):3997–4002, 2001.

[106] Richard K Scott and David G Dritschel. The structure of zonal jets in geostrophic turbulence. *J. Fluid Mech.*, 711:576–598, 2012.

[107] Andrey Y Shcherbina, Eric A D'Asaro, Craig M Lee, Jody M Klymak, M Jeroen Molemaker, and James C McWilliams. Statistics of vertical vorticity, divergence, and strain in a developed submesoscale turbulence field. *Geophys. Res. Lett.*, 40(17):4706–4711, 2013.

[108] A. G. Slavin and Y. D. Afanasyev. Multiple zonal jets on the polar beta plane. *Phys. Fluids*, 24:016603, 2012.

[109] Serguei Sokolov and Stephen R Rintoul. Multiple jets of the antarctic circumpolar current south of australia. *J. Phys. Ocean.*, 37(5):1394–1412, 2007.

[110] J Sommeria, SD Meyers, and Harry L Swinney. *Experiments on vortices and Rossby waves in eastward and westward jets*, volume 109. North-Holland, 1991.

[111] Jöel Sommeria, Steven D Meyers, and Harry L Swinney. Laboratory simulation of jupiter's great red spot. *Nature*, 331(6158):689–693, 1988.

[112] Joël Sommeria, Steven D Meyers, and Harry L Swinney. Laboratory model of a planetary eastward jet. *Nature*, 337(6202):58–61, 1989.

[113] Michael A Spall. Large-scale circulations forced by localized mixing over a sloping bottom. *J. Phys. Ocean.*, 31(8):2369–2384, 2001.

[114] Michael A Spall and Robert S Pickart. Wind-driven recirculations and exchange in the labrador and irminger seas. *J. Phys. Ocean.*, 33(8):1829–1845, 2003.

[115] A. Stegner and V. Zeitlin. From a quasi-geostrophic to a non-linear monopolar vortices in a paraboloidal shallow-water-layer experiment. *J. Mar. Res.*, 356:1–24, 1998.

[116] H. Stommel. Is the south pacific helium-3 plume dynamically active? *Earth Planet. Sci. Lett.*, 61:63, 1982.

[117] Yi Sui and Yakov D Afanasyev. Buoyancy storms in a zonal stream on the polar beta-plane: Experiments with altimetry. *Phys. Fluids*, 25(6):066604, 2013.

[118] S. Sukoriansky, N. Dikovskaya, and B. Galperin. On the arrest of inverse energy cascade and the rhines scale. *J. Atmos. Sci.*, 64:3321, 2007.

[119] Semion Sukoriansky, Boris Galperin, and Nadejda Dikovskaya. Universal spectrum of two-dimensional turbulence on a rotating sphere and some basic features of atmospheric circulation on giant planets. *Phys. Rev. Lett.*, 89(12):124501, 2002.

[120] Andrew F Thompson. The atmospheric ocean: eddies and jets in the antarctic circumpolar current. *Philosophical Transactions of the Royal Society of London A: Mathematical, Physical and Engineering Sciences*, 366(1885):4529–4541, 2008.

[121] G. K. Vallis. *Atmospheric and Oceanic Fluid Dynamics: fundamentals and large-scale circulation*. Cambridge University Press, 2006.

[122] G. K. Vallis and M. E. Maltrud. Generation of mean flows and jets on beta plane and over topography. *J. Phys. Ocean.*, 23:1351, 1993.

[123] GJF Van Heijst. Topography effects on vortices in a rotating fluid. *Meccanica*, 29(4):431–451, 1994.

[124] John M Wallace and David S Gutzler. Teleconnections in the geopotential height field during the northern hemisphere winter. *Mon. Weather Rev.*, 109(4):784–812, 1981.

[125] Bin Wang and Xiaosu Xie. Low-frequency equatorial waves in vertically sheared zonal flow. part i: Stable waves. *J. Atmos. Sci.*, 53(3):449–467, 1996.

[126] J. A. Whitehead. Mean flow driven by circulation on a -plane. *Tellus*, 27:634, 1975.

[127] Paul D Williams and Christopher W Kelsall. The dynamics of baroclinic zonal jets. *J. Atmos. Sci.*, 72(3):1137–1151, 2015.

[128] RD Wordsworth, PL Read, and YH Yamazaki. Turbulence, waves, and jets in a differentially heated rotating annulus experiment. *Phys. Fluids*, 20(12):126602, 2008.

[129] C. Wunch. Toward a midlatitude ocean frequency-wavenumber spectral density and trend determination. *J. Phys. Ocean.*, 40:22642281, 2010.

[130] Carl Wunsch. Toward a midlatitude ocean frequency-wavenumber spectral density and trend determination. *J. Phys. Ocean.*, 40(10):2264–2281, 2010.

[131] Z Xiao, M Wan, S Chen, and GL Eyink. Physical mechanism of the inverse energy cascade of two-dimensional turbulence: a numerical investigation. *J. Fluid Mech.*, 619:1–44, 2009.

[132] Yuan and Hamilton. Equilibrium dynamics in a forced-dissipative f-plane shallow water system. *J. Fluid Mech.*, 280:369, 1994.

[133] V. Zeitlin. *Nonlinear dynamics of rotating shallow water: methods and advances*, volume 2. Elsevier, 2007.

[134] Y Zhang and YD Afanasyev. Beta-plane turbulence: Experiments with altimetry. *Phys. Fluids*, 26(2):026602, 2014.

[135] Zhengguang Zhang, Wei Wang, and Bo Qiu. Oceanic mass transport by mesoscale eddies. *Science*, 345(6194):322–324, 2014.